Plasma Modification of Polydimethylsiloxane in a hydrogen CCRF low-pressure discharge

Inauguraldissertation

zur

Erlangung des akademischen Grades eines

Doktors der Naturwissenschaften (Dr. rer. nat.)

der

Mathematisch-Naturwissenschaftlichen Fakultät

der

Ernst-Moritz-Arndt-Universität Greifswald

vorgelegt von

Vladimir Danilov

geboren am 07.10.1984

in Sankt-Petersburg, Russland

Greifswald, 17.09.2013

Dekan:	Prof. Dr. Klaus Fesser
1. Gutachter:	Prof. Dr. Jürgen Meichsner
2. Gutachter:	Prof. Dr.-Ing. Peter Awakowicz
Tag der Promotion:	January 16, 2014

To my parents, my sister and Valeria

Content

1. Introduction

Plasma is widely used for various solutions of scientific and specific industrial problems. It is generated by applying of electromagnetic field to a gas inside a vacuum chamber. This field may be constant (direct-current discharge) or alternating (radio-frequency or microwave discharge). Basically, the plasma consists of ions, free electrons, neutrals, free radicals, excited particles and photons. The interaction of these plasma components with solid or liquid material may be used to change their surface properties in a wide range and to expand the field of applications.

In comparison with wet chemical treatment the plasma processing does not require the use of any harmful substances (acids, hydroxides, etc.), in other words it is environmentally friendly. At the same time the temperature of heavy particles in the plasma is equal or differs little from the room temperature, which is required for the treatment of heat-sensitive materials, e.g. polymers. The combination of low gas temperature with high chemical activity makes the non-thermal plasma as an attractive tool for material surface processing.

1.1. Research objectives

Nanocomposites can be defined as multiphase solid materials, where at least one phase has one, two or three dimensions in the nanometer range (up to 100 nm). Often nanocomposite coating consists of a solid matrix material and nanoscale reinforcing materials, which can have various structure and chemical composition to provide different properties to nanocomposites. The area of interaction between a solid matrix and reinforcements is by orders of magnitude higher than in conventional composites. Thus, even relatively low amount of reinforcements may significantly affect on the macroscopic properties of nanocomposites such

as dielectric properties, heat resistance, or mechanical properties such as stiffness, hardness, and resistance to damage and wear.

Different techniques are available for producing such nanocomposite coatings. One is the gas flow sputtering (GFC).[1] It is based on a hollow glow discharge and an inert gas flow supported material transport to the substrate. This technique distinguishes itself by the high deposition rates in the order of $10 - 20\ \mu m/h^{-1}$, operates at a low vacuum (1 mbar range) and is applicable to a wide range of coating materials.[2,3] Among other techniques are the magnetron co-sputtering [4,5], co-evaporation [6,7], magnetron sputtering from a composite target [8] or a combination of evaporation and sputtering with plasma polymerization.[9]

The present work is arisen from the collaborative research project "Plasma hybrid coating: functional surfaces by plasma supported nanotechnology" funded by the Volkswagen Foundation. In this project the Fraunhofer Institute for Manufacturing Technology and Advanced Materials in Bremen, the University of Bremen and the University of Greifswald were involved. The goal of this project was the development of an innovative nanocomposite coating with functional properties: corrosion protection, photocatalytic activity, antibacterial protection and improved fluidic properties.

Three conceptions are outlined in Figure 1.1, involving hybrid processes to produce functional thin solid films from a liquid precursor without and with nanoparticles. In the first one the liquid polydimethylsiloxane (PDMS) film is deposited onto the surface. Afterwards the film is crosslinked by the treatment in the low-pressure capacitively coupled radio-frequency (CCRF) discharge. The resulting surface is expected to be smoother and the plasma modified layer may act as a barrier for the oxygen diffusion.

In the second one a suspension of silver nanoparticles in PDMS is deposited on the surface and crosslinked by the non-thermal plasma. Silver nanoparticles are toxic for microorganisms, and the surface becomes antibacterial properties.[10,11] The third line was realized by use of anatase TiO_2 nanoparticles dispersed in liquid PDMS. Like in the other cases, the liquid film is deposited on the surface and crosslinked by the non-thermal plasma. The TiO_2 crystalline configurations rutile and anatase show a photocatalytic activity. However, the anatase exhibits a higher activity compared to the rutile.[12] The band gap of anatase is about 3.2 eV.[13,14] It means that the UV radiation with wavelength shorter than ca. 386 nm will generate electron-hole pairs, which can

initiate chemical reactions for decomposition of organic material on the nanoparticle. To increase the photocatalytic efficiency the surface of the embedded nanoparticles should be partially free from plasma modified PDMS. This was realized by plasma etching of the covering layer in the low-pressure CCRF discharge in CF_4.[15]

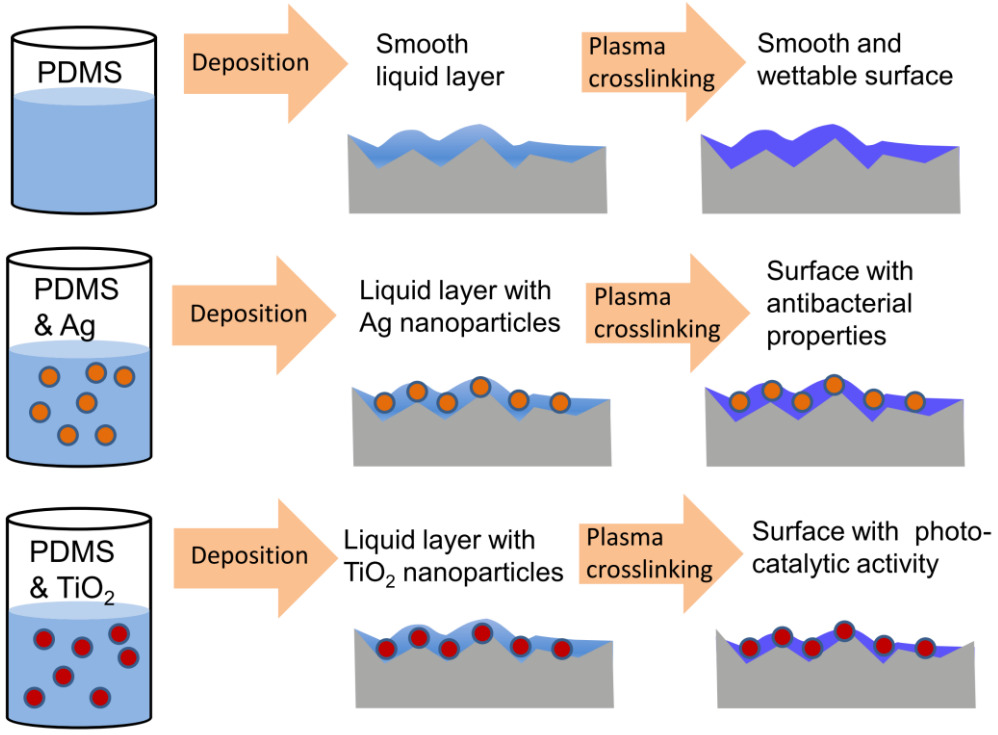

Figure 1.1. Basic conceptions of hybrid processes for the realization of multifunctional surface coatings.

For the development of this technology the presented work is focused on fundamental investigations to study the crosslinking mechanisms in dependence on the plasma and processing parameters of low-pressure CCRF plasma. In particular, the CCRF plasma was analyzed by probe measurements and optical emission spectroscopy. Obviously, the main plasma component which initiates chemical reactions in the bulk of PDMS films is the VUV radiation. The VUV spectrum of the plasma induced emission for different processing gases such as Ar, Xe, O_2, H_2O and H_2 was obtained for different pressures. It was found that the H_2 plasma is much more advantageous than others because of the strong emission from excited hydrogen molecules in the VUV range. Thus, its emission spectrum was studied the most detailed for different processing parameters: RF power and pressure. The absolute intensity of the VUV radiation was measured by the VUV power meter.

The UV-visible spectrum was monitored to control the purity of processing gas and to detect possible emission from radicals leaving the film. The idea was to find the correlation between the intensity of radical emission with the state of modification of thin film.

To transfer the plasma modification from laboratory devices to the industrial scales it is necessary to know internal plasma parameters. For this reason the electron energy distribution function (EEDF) was measured by probe diagnostics for various pressure and RF power. From EEDF the electron concentration and the effective electron temperature were calculated. To avoid the surface bombardment by energetic ions the samples were immersed in the plasma bulk at floating potential. In this case the difference between plasma and floating potential defines the maximal kinetic energy of positive hydrogen ions accelerated in the plasma sheath to the sample surface. The probe technique allowed measuring the plasma and the floating potential and provided the estimation of the ion penetration depth in the film.

The characterization of thin non-modified and modified films was performed by Fourier Transform InfraRed (FTIR) spectroscopy, in particular, by InfraRed Reflection Absorption Spectroscopy (IRRAS). This sensitive technique allows to obtain spectra of ultra thin films.[16] The film thickness and its reduction after the plasma modification was determined by the spectroscopic ellipsometry (SE). Various damages, surfaces defects and changes of film surface topology were investigated by the optical microscopy.

1.2. State of the art in plasma treatment of organosilicones

Modification of polydimethylsiloxane (PDMS) using treatment either by direct plasma or by radiation of plasma was realized in different works. One of most common cases is the modification by radio-frequency (RF), microwave (MW) or corona discharge in different gases.[17-24] Other way is to treat PDMS by VUV/UV light from mercury or Xe excimer lamp in oxygen atmosphere or in vacuum.[18,20,25-31] Polydimethylsiloxane is an excellent material for the fabrication of microfluidic devices used for biological purposes.[31-33] Hydrophilicity is needed in certain applications, e. g. to provide cell adhesion and facilitate channels to fill with aqueous solutions. However, PDMS is a hydrophobic material; its contact angle is 105 – 110 degrees.[19,23,24,30] Plasma treatment of

PDMS as reported in various works increases the wettability. The top surface transforms into a thin brittle SiO_x top layer which also contains polar OH groups. Thus, the surface becomes hydrophilic with the contact angle in the range of 0 − 30 degrees.[18,19,24] However, the effect is not permanent, the hydrophobicity restores. In Hillborg et al. [19] this process was investigated by contact angle measurements for samples treated in different plasma and, thereafter, stored in various atmospheres: dry air, argon and vacuum. The recovery kinetics and XPS results showed that it is not due to contamination trough adsorption from the atmosphere. A general agreement to this phenomenon is that the recovery appears due to diffusion of low molar weight (LMW) species to the surface.[19,34] Eddington et al. used thermal pre-treatment of PDMS samples, modified later in oxygen plasma. In this case the hydrophilicity of the surface was retained for a much longer time.[35] Vickers et al. used chemical treatment to remove LMW species from the bulk of PDMS.[36] Then PDMS was oxidized by plasma. The hydrophobic recovery was absent during at least 7 days of storage in air.

The biocompatibility of siloxane intraocular lenses can be improved by plasma surface modification.[37,38] In particular, the inflammation of eyes after the implantation of a siloxane lens appears foremost due to the diffusion of toxic monomer residues with SiH groups to the surface. The plasma treatment produces a barrier layer, which blocks monomer release to the surface and completely prevents the harmful effect. Furthermore, the influence of processing plasmas on integrated circuits (IC) during their manufacturing is important to understand. Typical materials used for the production of ultra-large scale integrated (ULSI) circuits are methylsilsesquioxane (MSQ), hydrogen silsesquioxane (HSQ) and low-k SiOCH dielectric films.[39,40] One of the steps of ULSI circuit production is the resist ashing (resist removal). Generally, it is realized by use of low-pressure capacitively coupled radio-frequency (CCRF) discharge in O_2. However, this process damages the wafer and decreases the performance of produced circuit.[40,41] Namely, this damage results in the increase of dielectric constant and higher leakage current in IC. [39,40] Alternatively, the ashing can be performed by N_2/H_2 or H_2 plasmas with reduced damage to low-k SiCOH films.[40,42,43]

2. Low pressure capacitively coupled radio frequency (CCRF) plasma

2.1. Plasma. Basics.

In the second half of the 70s of the XIX century a member of the Royal Society of London William Crookes became interested in gas discharges in vacuum. In 1879 Crookes published the paper, where he proposed that: "The phenomena in these exhausted tubes reveal to physical science a new world - a world where matter may exist in a fourth state… " [44] In the 1920s the future Nobel laureate in chemistry Irving Langmuir was investigating gas discharges. Realizing that these discharges have many special properties, Langmuir firstly introduced the term plasma for the fourth state of matter in 1928.[45]

Plasma can be defined as a partially or completely ionized gas, containing electrons, atomic and molecular ions, free radicals, neutral atoms and molecules in the ground and excited states. The negative and positive charges compensate each other so that the total charge is approximately zero and plasma is electrically neutral. This property is known as quasi-neutrality. The charges in plasma shield each other. The Debye length is the characteristic distance at which an external electrostatic field is screened by charged particles of plasma. The Debye length is equal also to the maximum distance at which the separation of charges in the plasma is possible. In other words it characterizes the scale over which quasi-neutrality of plasma can be disrupted. Since deviations from quasi-neutrality should be small, we can assume that $|e\varphi| \ll T_e, T_i$. (φ is the potential of point charge).

In this case, the Debye length can be calculated from formula:

$$\lambda_D{}^{-2} = \left[\frac{n_e e^2}{\varepsilon_0 k_B}\left(\frac{1}{T_e} + \frac{1}{T_i}\right)\right] = \lambda_{De}{}^{-2} + \lambda_{Di}{}^{-2} \qquad (2.1)$$

Where n_e is the concentration of electrons, T_e and T_i are temperatures of electrons and ions, λ_{Di} and λ_{De} – Debye lengths of electrons and ions.

For non-thermal plasma ($T_e \gg T_i$), assuming that ions immobile in comparison with electrons, the Debye length should be defined as:

$$\lambda_D = \sqrt{\frac{\varepsilon_0 k_B T_e}{n_e e^2}}$$

The plasma frequency ω_p is another important parameter, which describes the frequency of free longitudinal oscillations of space charges in homogeneous plasma in the absence of magnetic field. These oscillations are caused by the action of an electric field on charges, which arises due to a local violation of the plasma quasi-neutrality.

$$\omega_p{}^2 = \omega_{pe}{}^2 + \omega_{pi}{}^2$$

$$\omega_{pe} = \sqrt{\frac{n_e e^2}{\varepsilon_0 m_e}} \qquad \omega_{pi} = \sqrt{\frac{n_i Z^2 e^2}{\varepsilon_0 m_i}} \qquad (2.2)$$

Where Z is ionization multiplicity, m_e and m_i are masses of electrons and ions, respectively. Since $m_i \gg m_e$, it follows that $\omega_{pe} \gg \omega_{pi}$.

Not every system of charged particles can be called plasma. The plasma has the following properties:

- The Debye length must be small in comparison with the characteristic size of plasma L. This means that the collective interactions occurring in the plasma bulk are more significant than the effects on its boundary. If this condition is satisfied, the quasi-neutral plasma can be considered for the condition:

  $$\lambda_D \ll L$$

  If L is comparable with λ_D we deal with a group of separate charged particles, rather than with plasma.

- The density of charged particles n should high enough so that each of them interacts with many surrounding charged particles, rather than just with the closest particle. The number of charged particles in a sphere with Debye length as radius should be sufficient for the appearance of collective effects. Mathematically, this condition can be expressed as follows:

  $$\lambda_D{}^3 n \gg 1$$

- The average time between electron-neutral collisions τ must be large compared with the period of plasma oscillations. In this case the plasma is dominated by electromagnetic interactions over the processes of the neutral gas kinetics. It means:

$$\omega_p \gg 1/\tau$$

Plasmas exist naturally or can be created in the discharge reactor for specific purposes. If we take into account that all the stars and a significant part of the interstellar medium are plasma, it turns out that in the universe in such a state is more than 99% of matter. Plasmas cover a very large range of electron temperatures and densities (Figure 2.1).

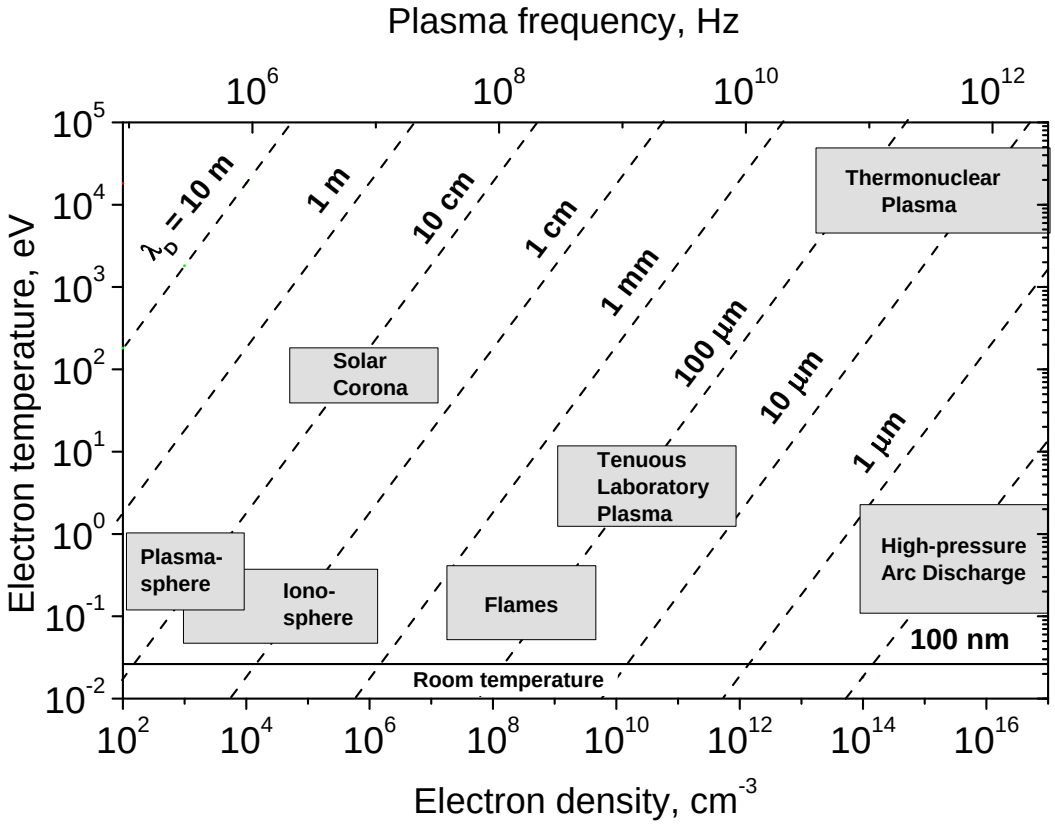

Figure 2.1. Examples of different plasmas and intervals of values of their typical electron density and temperature. Adapted from [46-48]

The ionosphere stretches from a height of about 50 km to more than 1000 km upward from the Earth's surface. It contains plasma with electron density up to 10^6 cm^{-3} and typical electron temperature of few tenths of an electron volt.[49,50] Solar corona is the outer layers of the solar atmosphere, beginning above the thin transition region above the chromosphere, in which the gas temperature increases to 100 times. The

integral brightness of the corona ranges from only $0.6 \cdot 10^{-6}$ to $1.3 \cdot 10^{-6}$ of the total brightness of solar disk. [51] Therefore, it is not visible in the absence of eclipses or without technological tricks (e.g. coronagraph). Solar radiation with a wavelength of less than 20 nanometers is entirely based on the corona. This means that on the images of the sun made at lesser wavelengths only the solar corona is visible, and the chromosphere and the photosphere are not seen.[52] The corona electron temperature is in the order of 100 eV and the concentration ranges approximately from 10^4 to 10^7 cm^{-3}.[53-55] Solar wind is a stream of ionized particles (mostly helium-hydrogen plasma) flowing out of the solar corona into the surrounding space at velocities of 300 - 800 km/s. Its electron temperature is in the range between 10 and 40 eV and the concentration is only about 5 cm^{-3}.[56] For thermonuclear plasma extreme values of electron temperature and density are usual. Thermonuclear reaction of hydrogen fusion to form helium is the source of Sun energy. Electron density of its core reaches 10^{26} cm^{-3} and electron temperature is about 1000 eV.

Among man-made plasmas are various types of laboratory discharges like DC glow discharges, inductively coupled plasma (ICP), capacitively coupled plasma (CCP), microwave plasma, barrier discharges (BD) and etc. Typical electron concentration in low pressure discharge ranges from 10^9 to 10^{12} cm^{-3}, while the electron temperature (two-thirds of the average energy) varies in most cases from 1 to 10 eV.[57]

This work concerns the capacitively coupled radio-frequency (CCRF) discharge at low pressures, which will be described in detail in the following paragraph.

2.2. Specifics of CCRF plasmas

The capacitively coupled plasma (CCP) is one of the most widespread plasma sources for materials processing. Standard CCP system is driven by a single radio-frequency (RF) power supply. Mostly, the CCRF discharges operate at low pressure of between 1 and 10^4 Pa, but also RF discharges at atmospheric pressure can be realized. The simplest setup consists of two metallic electrodes separated by a distance: one electrode is connected to the RF power supply, and the other one is grounded. The electrodes are placed either in the discharge chamber or outside the

chamber with dielectric walls, respectively. In contrast to the DC, for the AC the presence of a dielectric in the circuit is not an obstacle, a displacement current flows through a device even in the absence of the discharge. This configuration is like a capacitor in an electric circuit, and therefore, such discharge is called capacitively coupled discharge. RF corresponds to the frequency range from about 1 to 100 MHz. For laboratory setups the most often used frequency is 13.56 MHz, which corresponds to a wavelength of about 22 m.

Let's consider the characteristic case for RF low-pressure discharge: the electron mean free path is much smaller than the characteristic dimensions of the discharge plasma, the plasma density is low, typical electron concentration is about 10^{10} cm^{-3}. This allows us to ignore the influence of charged particles on each other and consider the motion the individual particles.

The equation of motion of an electron in RF field can be written in the form [58]:

$$m_e \frac{dU}{dt} = eE - gU \tag{2.3}$$

where U – drift velocity of electron; E – electric field strength; m_e – electron mass, e – electron charge; g – friction coefficient of electrons due to the presence of collisions in the plasma.

Due to the fact that the frequency of elastic collisions between electrons and heavy particles is much higher than the frequency of its inelastic collisions, the coefficient g can be expressed in terms of the effective elastic collision frequency ν_0. The expression follows from the fact that the friction force between these particles on the one hand equals gU, and on the other, it is the change in momentum per ν_0 collisions.

$$g = m_e \nu_0 \tag{2.4}$$

The electric field strength with angular frequency ω and amplitude E_0 can be expressed as follows:

$$E = E_0 e^{i\omega t} \tag{2.5}$$

Equation (2.3) with respect of (2.4) and (2.5) can be rewritten as follows:

$$m_e \frac{dU}{dt} = eE_0 e^{i\omega t} - m_e \nu_0 U \qquad (2.6)$$

At 13.56 MHz the wavelength is about 22 m and we can assume that the electric field strength do not alter along the trajectory of electron motion.

As the result the solution of equation (2.6) can be found in the following form:

$$U = \frac{eE}{m_e(i\omega + \nu_0)} = \mu_e E = -\mu_a E + i\mu_r E \qquad (2.7)$$

$$\mu_a = \frac{e\nu_0}{m_e(\omega^2 + {\nu_0}^2)} \qquad \mu_r = \frac{e\omega}{m_e(\omega^2 + {\nu_0}^2)}$$

The complex quantity μ_e is the coefficient of proportionality between the electron drift velocity and the electric field strength of RF field. It is called electron mobility in RF field.

The electron current density j flowing through the plasma in a local region of space, for which the electron density n_e and temperature T_e are constant, can be expressed trough velocity U:

$$j = -en_e U = en_e\mu_a E - ien_e\mu_r E = \sigma_a E - i\sigma_r E \qquad (2.8)$$

$$\sigma_a = \frac{e^2 n_e \nu_0}{m_e(\omega^2 + {\nu_0}^2)} \qquad \sigma_r = \frac{e^2 n_e \omega}{m_e(\omega^2 + {\nu_0}^2)}$$

Where σ_a and σ_r are the resistive and reactive components of plasma conductivity, respectively. It is seen that the behavior of the mobility and conductivity depends essentially on the relation between ω and ν_0.

Consider three cases where $\omega >> \nu_0$, $\omega << \nu_0$ and $\omega \sim \nu_0$.

1. $\omega >> \nu_0$. It follows that $\mu_a << \mu_r$, $\sigma_a << \sigma_r$. In this case the discharge plasma is a reactive load for the RF power generator. Electrons move mainly in a phase with the RF field alteration. During one half of RF

period electron is accelerated and takes energy, during second half it loses all energy. The electrons does not heat the plasma, no RF power is consumed over one RF cycle. The phase shift between the current and the field is close to π/2.

For this situation the mean free path of the electron λ_e should significantly exceed the amplitude of free electron oscillations A_0 in the RF field. The value of A_0 can be found from the equation of the free electron motion along the x coordinate, along which an RF field is directed.

$$m_e \frac{d^2x}{dt^2} = eE_0 \sin \omega t$$

$$m_e \frac{dx}{dt} = -eE_0 \cos \omega t$$

$$x = \frac{eE_0}{m_e \omega^2} \sin \omega t, \qquad A_0 = \frac{eE_0}{m_e \omega^2} \qquad (2.9)$$

As an example, we take ω = 85.20 MHz, which corresponds to one of the most commonly used in the practice oscillation frequency of 13.56 MHz. For the value of $E_0 \approx 10$ V/cm, $A_0 = 2.4$ cm. Electron mean free path at a pressure p = 100 Pa for H_2 and electron energies between 0 and 10 eV is about 300 μm. [59,60] Comparing these values, we conclude that the present case, where the plasma is predominantly reactive load, is realized only at relatively low pressures of less than 1 Pa.

2. As the pressure increases and the value of ν_0 approaches the value ω, the active component of mobility and conductivity increases. Plasma absorbs the energy of RF field increasingly. This is due to the fact that electrons in collisions with heavy particles change the direction of their movement, and more often this change coincides with the phase change of RF field and electrons are accelerated again over the next half-period of the electric field. Thus, the transfer of RF field energy to electrons in the plasma bulk occurs due to the presence of collisions. This is the main difference between the RF and DC discharge physics, where the only consequence of collisions between electrons and charged particles is the loss of the energy. Described case is called alpha mode.

3. $\omega << \nu_0$. In this case, mainly resistive current flows through the plasma. The situation takes place at relatively high pressures. This pressure range can be approximately determined from the condition $\lambda_e << A_0$. Let's take $A_0/\lambda_e > 100$, it gives $p > 100 - 200$ Pa for different

gases. The heating of heavy particles in the plasma enhances with the increase of pressure and ν_0. Gas temperature grows more, which does not provide a low-temperature processing of thin films. That is why, in practice, a relatively narrow range of plasma gas pressure 20 – 200 Pa is used.

An equivalent electric circuit of a CCRF discharge is shown in the Figure 2.2.[61,62] The power is applied to one electrode usually via a blocking capacitor C_b, which is a part of the matching network. The capacitor is not an obstacle for the RF field, but it acts like an open circuit for the direct current. Therefore, the net charge transport through the discharge averaged over one RF period cycle is zero. If the blocking capacitor is present and when both electrodes have different size, where the area of the powered electrode is usually smaller than the effective area of grounded electrode, a negative DC self-bias voltage is formed at the powered electrode. The massive ions do not follow instantaneously the alternating RF field. On the other hand, the electrons follow the field, reach the electrode and it becomes negatively charged. This causes a DC field and corresponding DC bias voltage V_{bias} (see Figure 2.3) in the plasma additionally to the RF field. The DC field accelerates positive ions towards the powered electrode.

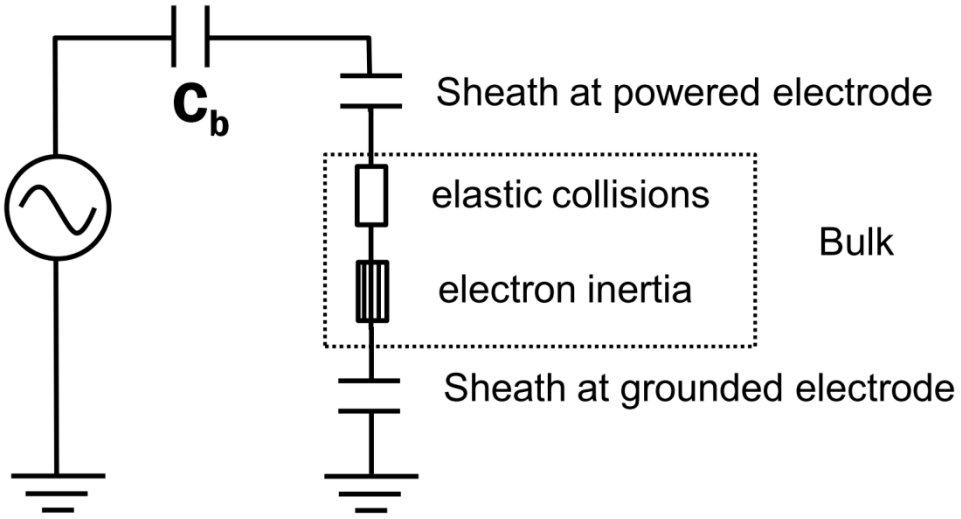

Figure 2.2. Equivalent electric circuit of CCRF discharge.

Consider the voltage on the powered electrode has the form:

$$V(t) = V_{bias} + V_{RF} \sin \omega t \qquad (2.10)$$

V_{bias} is the self-bias voltage; V_{RF} is the amplitude of RF field. If the sheath is purely capacitive, the plasma potential can be expressed as follows:

$$V_{pl}(t) = \overline{V_{pl}} + V_{pl0} \sin \omega t \tag{2.11}$$

$\overline{V}_{pl}$ – time-averaged plasma potential.

V_{pl0} can be determined by capacitive voltage division of V_{RF} [63]

$$V_{pl0} = \left(\frac{C_{pow}}{C_{pow} + C_{gr}} \right) V_{RF} \tag{2.12}$$

Where C_{pow} is the capacitance of the sheath at the powered electrode, and C_{gr} – at the grounded electrode.

The electron mobility is much higher than the ion mobility. It means that the instant plasma potential should be not less than the instant potential of any surface, which contacts with plasma. In the considered case it gives:

$$V_{pl\_max} = \overline{V_{pl}} + V_{pl0} \geq V_{bias} + V_{RF}$$

$$V_{pl\_max} = \overline{V_{pl}} - V_{pl0} \geq 0 \tag{2.13}$$

As far as the blocking capacitor is included in the circuit no net current flows through the powered electrode. Over an RF period the ion current is compensated by the electron current. The plasma potential reaches the potential of powered electrode and the sheath collapses for a brief period during the RF cycle to allow electron current to the electrode. For the grounded electrode the net current must also be zero, the plasma potential reaches ground potential, too.

Therefore, inequations (2.13) become equations (see Figure 2.4). For this case we obtain:

$$\bar{V}_{pl} = \frac{1}{2}(V_{bias} + V_{RF}) \tag{2.14}$$

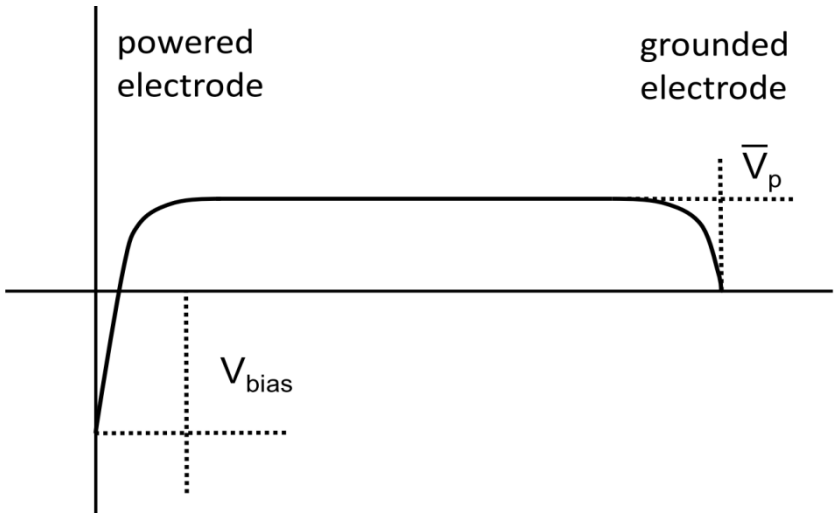

Figure 2.3. Time-averaged potential between powered and grounded electrode.

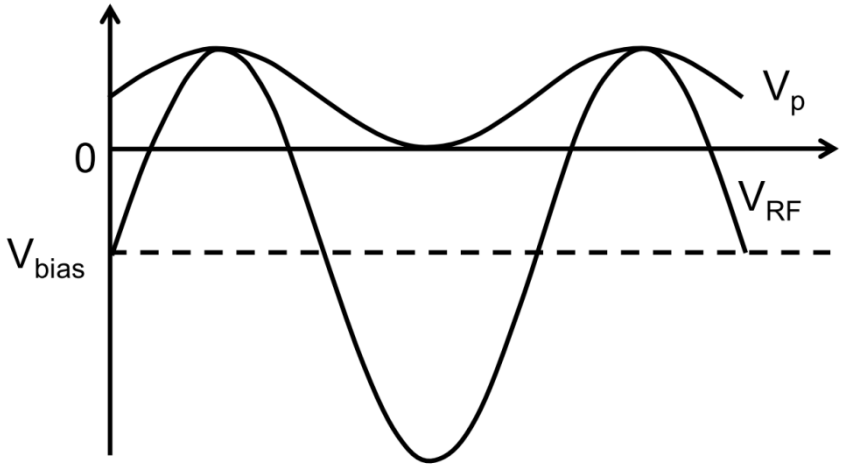

Figure 2.4. Temporal behavior of plasma potential V_p and the potential on the powered electrode for asymmetric CCRF discharge (idealized). The case of larger grounded electrode area relative to the powered one.

In combination with equation (2.12) it gives the self-bias voltage V_{bias} expressed trough V_{RF} and capacitances of the electrode sheathes C_{pow} and C_{gr}

$$V_{bias} = \left(\frac{C_{pow} - C_{gr}}{C_{pow} + C_{gr}}\right) V_{RF} \qquad (2.15)$$

3. Experimental setup, diagnostic methods and thin film preparation

3.1. Plasma apparatus and processing parameters

The film treatment was performed in a vacuum chamber using an asymmetric capacitively coupled RF discharge with the excitation frequency of 13.56 MHz. (see Figure 3.1) The vacuum chamber contains a circular planar electrode (Ø ≈ 10.73 cm), which was powered via the air-cooled matching network ENI MW-10D by a RF generator ENI ACG-6B. Walls and the electric shielding of the powered electrode were grounded. The RF power generator is able to deliver up to 600 watt and monitors simultaneously the forward and reflected power. The matching network consists of a tuner unit and a digital controller. It contains constant blocking capacitors C_b and two rotary variable capacitors to match the impedance for optimal energy transfer into the RF discharge. The tuner is connected with the powered electrode through a copper wire, which was specially made short for better transfer of the RF power and to avoid of RF interferences. The substrate was fixed by a ceramic (aluminum oxide) holder on the distance of 2 cm above the powered electrode and was kept under floating potential. It was oriented horizontally and the film was faced to the RF electrode surface. Before the treatment, the reactor chamber was evacuated to the base pressure, which did not exceed 0.1 Pa. Hydrogen was used as a processing gas at the pressure between 10 and 500 Pa, which was measured by the absolute capacitance monometer (MKS Instruments, Baratron 626AX, 0.001-10 mbar). The gas flow between 3 and 7 sccm was provided by the elastomer-sealed mass flow controller (MKS Instruments, Mass-Flo 1179BX, full scale range: 20 sccm of nitrogen). Before each treatment the samples were stored in the

processing chamber at the base pressure during 10 minutes for degassing. All main process parameters are listed in the Table 3.1.

Table 3.1. Main process conditions

Processing gas	H_2
Discharge type	CCRF, 13.56 MHz
Base pressure	< 0.1 Pa
Process pressure p	10-500 Pa
Gas flow f	3-7 sccm
Forward power	10-300 W
Full reactor volume V	ca. 5 L
Residence time t_r	63 s for 7 sccm and 150 Pa
Powered electrode surface area	90 cm^2
Treatment time	1-1800 s

Residence time is calculated from formula $t_r = {}^{pV}/_{f}$

3.2. Plasma diagnostics

3.2.1. VUV - vis emission spectroscopy

VUV monochromator

The plasma emission spectrum was registered by an Acton Research Corporation model VM-521-SG of vacuum monochromator with a focal length of 1 m. It was separated from the chamber by MgF_2 window with the light transmission cutoff at about 115 nm. Light enters the monochromator through a narrow entrance slit and is dispersed by a grating with 1200 grooves/mm. This configuration provides the possibility to measure between ca. 115 and 335 nm. In the experiments 500 μm width of entrance and exit slit resulted in the resolution of 0.4 nm. The

typical operation pressure inside the monochromator was better than 10^{-6} mbar.

VUV power meter

The Hamamatsu C9536 VUV power meter with the H9535 sensor head was applied to measure the integral VUV emission intensity through a short tube with a narrow MgF_2 window on the top side of chamber. This tube has a thread, which effectively decreased the reflection of plasma radiation from its inner side. The detector contains a phototube with the circular photocathode of 6 mm diameter. The diamond layer of the cathode is the wide-bandgap semiconductor with the bandgap of about 5.5 eV.[64-67] Thus, it is blind to the light with a wavelength above 225 nm. The device is able to measure intensities in the range from 1 $\mu W/cm^2$ to 200 mW/cm^2. The detector was calibrated at the wavelength of 146 nm, for which the relative expanded uncertainty is 11% ($k = 2$, level of confidence ca. 95%). The gap with the atmosphere between phototube window and the chamber window is 90 ± 20 μm, which amounts in 75 ± 5 % transmittance for 160 nm.[68-71] The relative standard deviation for all measurements of VUV intensity didn't exceed 12%.

UV-visible monochromator

UV-visible spectrum of plasma emission was monitored by Acton Research Corporation SpectraPro-750i monochromator. It was applied trough a soda-lime window on the side face of chamber. The plasma emission was imaged by a lens with the focal length of 175 mm and an iris diaphragm with the aperture of 3 mm to the entrance of the quartz glass fiber, which guided optical signal to the entrance slit. The lens focus was 2 cm over the surface of powered electrode and on the discharge axis. The device has Czerny-Turner design and includes a triple grating turret with 300, 1800 and 2400 grooves/mm. The latter was used for most of measurements. The focal length is 75 cm and the aperture ratio is f/6.5 for 68x68mm gratings. An acceptable signal level and the resolution of 0.2 nm were obtained setting the entrance and exit slits to 500 μm widths. The signal from the Acton Research Corporation photomultiplier PD-438 is registered by the oscilloscope Textronix TDS 520, which sends the data to the computer via General Purpose Interface Bus (GPIB). The high voltage DC power supply of PMT is provided by Stanford Research PS325/2500V-25W.

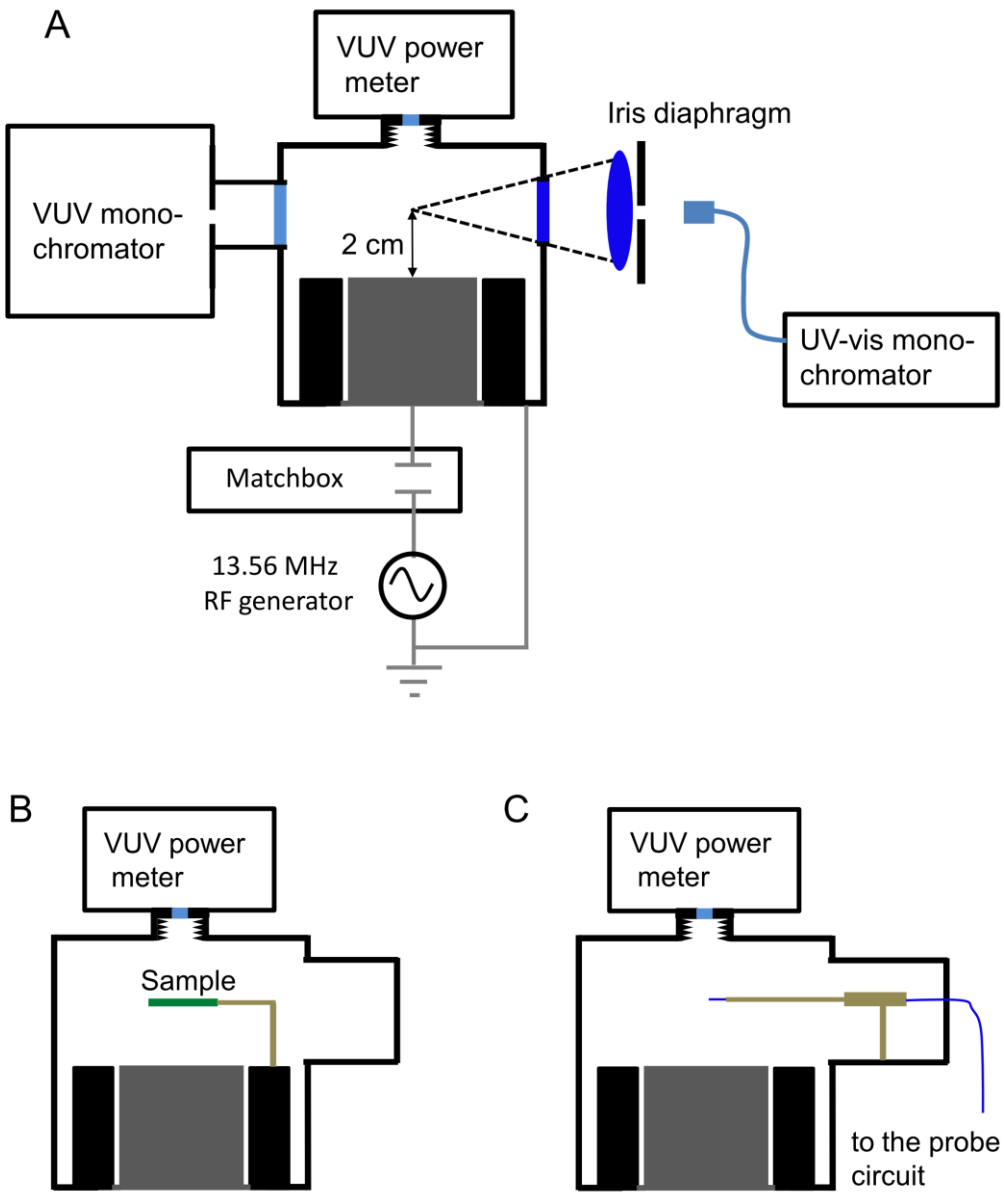

Figure 3.1. Schematic of the experimental setup (side-look).

The scheme (A) shows the adaption of the RF power supply, the spectroscopic techniques and VUV power meter, whereas the schemes (B) and (C) present additionally the sample holder and the Langmuir probe position, respectively. The light blue windows are made of MgF_2, dark blue – of ordinary soda-lime glass.

3.2.2. Electric probe measurements

Probe circuit design

A self-made system for probe measurements was applied from the the side face (Figure 3.1 C). A multimeter Keithley 2400 Sourcemeter was used to set the probe potential relative to the ground potential and to measure the probe current. The communication of the multimeter with the computer was arranged through the GPIB interface.

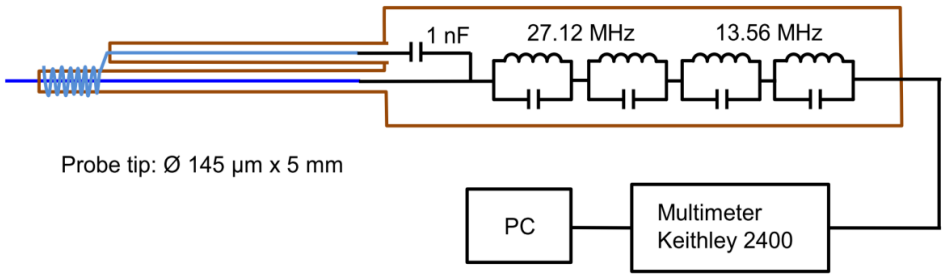

Figure 3.2. Probe circuit design. Light and dark blue wires are made of tungsten.

The probe tip made of tungsten has the length of 5 mm and the diameter of 145 µm. It was situated on the discharge axis and 2 cm over the surface of the powered electrode. The probe wire was threaded into a thin alumina tube with the outer diameter of 1 mm. For the compensation of an RF pickup on the probe the system proposed by Sudit and Chen was manufactured.[72] The RF filter consisted of two pairs of RF chokes for the first and second harmonic of an RF field (Figure 3.2). It was installed inside the plasma chamber to reduce a length of probe wire and, therefore, to minimize its stray capacitance, which can decrease the efficiency of filtering. The whole filter was protected in a glass jacket, which was covered by several layers of aluminum foil. The RF compensation electrode was coupled with the probe circuit trough a 1 nF capacitor. It was realized in the form of tungsten coil with 20 windings and had the total length of 8 mm and the diameter of ca. 1.5 mm.

3.3. Thin film diagnostics
3.3.1. Spectroscopic ellipsometry

Ellipsometry is a sensitive and precise technique for investigation of dielectric properties of thin films. It measures a relative change in polarization state of light transmitted or reflected from material. Thus, the technique does not depend on absolute intensity until the signal is sufficient for detection. In ellipsometry linearly polarized light at an oblique incidence becomes elliptically polarized (see Figure 3.3.). An amplitude ratio psi (Ψ) and the phase difference delta (Δ) represent the change in polarization state. The measured signal is a function of optical properties (refractive index and absorption coefficient) and thickness of thin films, which, therefore, can be evaluated by ellipsometry. Other possible application of ellipsometry is the determination of the surface roughness and the thickness non-uniformity.

Investigations on ellipsometry can be performed by single wave-length technique (Single Wavelength Ellipsometry (SWE)) with laser as a light source. In this case two measured values Ψ and Δ determine only two properties. It is enough for transparent films to evaluate the refractive index n and the thickness d. However, if the film absorbs light ($k \neq 0$) the results on determination of n and d will be incorrect. Even for a transparent film the ellipsometric data (Ψ, Δ plot) is a periodic function of the film thickness.[73] The solution gives multiple possible thicknesses separated by a cycle period, and thus an additional guess is needed to find the real thickness.

Nowadays, spectroscopic ellipsometry (SE) is common in different research fields. It uses broad band light sources emitting in VUV, visible or IR regions. The amount of acquired data is increased as measurements are done for many wavelengths. Unlike the refractive index, the film thickness does not depend on the wavelength, and therefore SE overdetermines it. E. g. 100 wavelengths provide 100 (Ψ, Δ) pairs of data for only 101 unknowns. This gives a unique result and helps to overcome the problem with periodical solution for the thickness.

The mathematical theory of ellipsometry is based on Fresnel equations, which result from solutions of Maxwell's equations.[74] The basic equation of ellipsometry, which connects the ellipsometric parameters Δ

and Ψ and the complex Fresnel reflection coefficients of the sample r_p and r_s for p- and s- polarizations is:

$$\rho \stackrel{\text{def}}{=} \frac{r_p}{r_s} = \frac{E_{pr}/E_{sr}}{E_{pi}/E_{si}} = \frac{|r_p|}{|r_s|} e^{-i\Delta} = \tan(\Psi)\, e^{-i\Delta} \qquad (3.1)$$

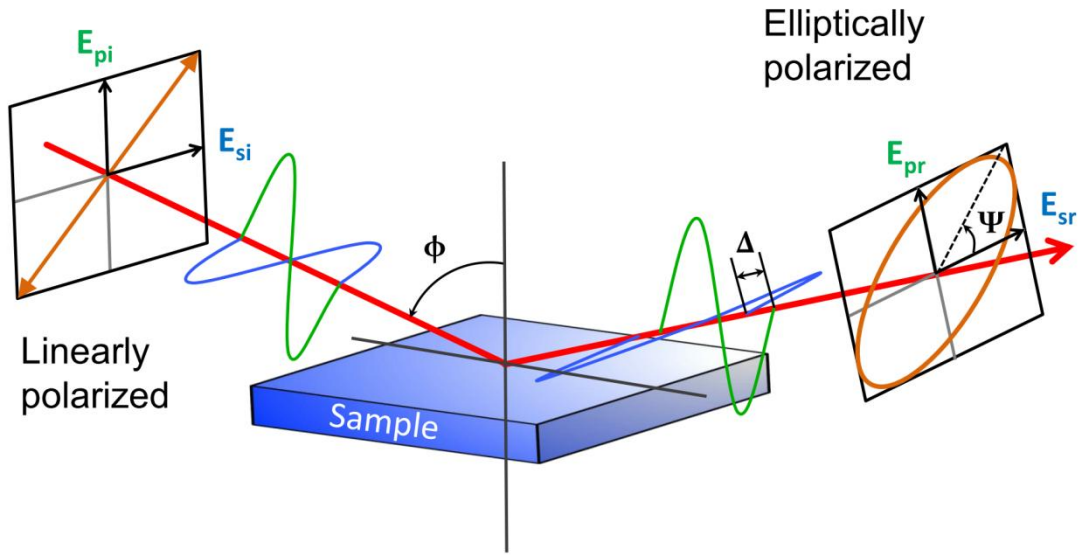

Figure 3.3. The general principle in ellipsometry.

For a model ambient/film/substrate SE measures ρ as a function of $n_0, \tilde{n}_1, \tilde{n}_2, \lambda, \phi, d$, where n_0 is refractive index of ambient, $\tilde{n}_1, \tilde{n}_2$ are complex refractive index of a film and a substrate, respectively, λ – wavelength, ϕ – angle of incidence and d is a film thickness. Complex refractive index $\tilde{n} = n + ik$ represents refractive index n and extinction coefficient k, which are functions of wavelength. n describes a change in the phase velocity and k describes a change of an amplitude of the electromagnetic wave propagating through a substance. For transparent materials k is zero. From measured values of Δ and Ψ one solves the inverse problem using a selected optical model, which results in the determination of unknown $\tilde{n}_1 = n_1 + ik_1$ and d.

Figure 3.4 outlines the process of measurement and analysis used in SE. At the beginning Δ and Ψ data is acquired in certain wavelength range. Next an optical model for a sample should be created, and then optical constants and a thickness of each layer should be selected. If the optical

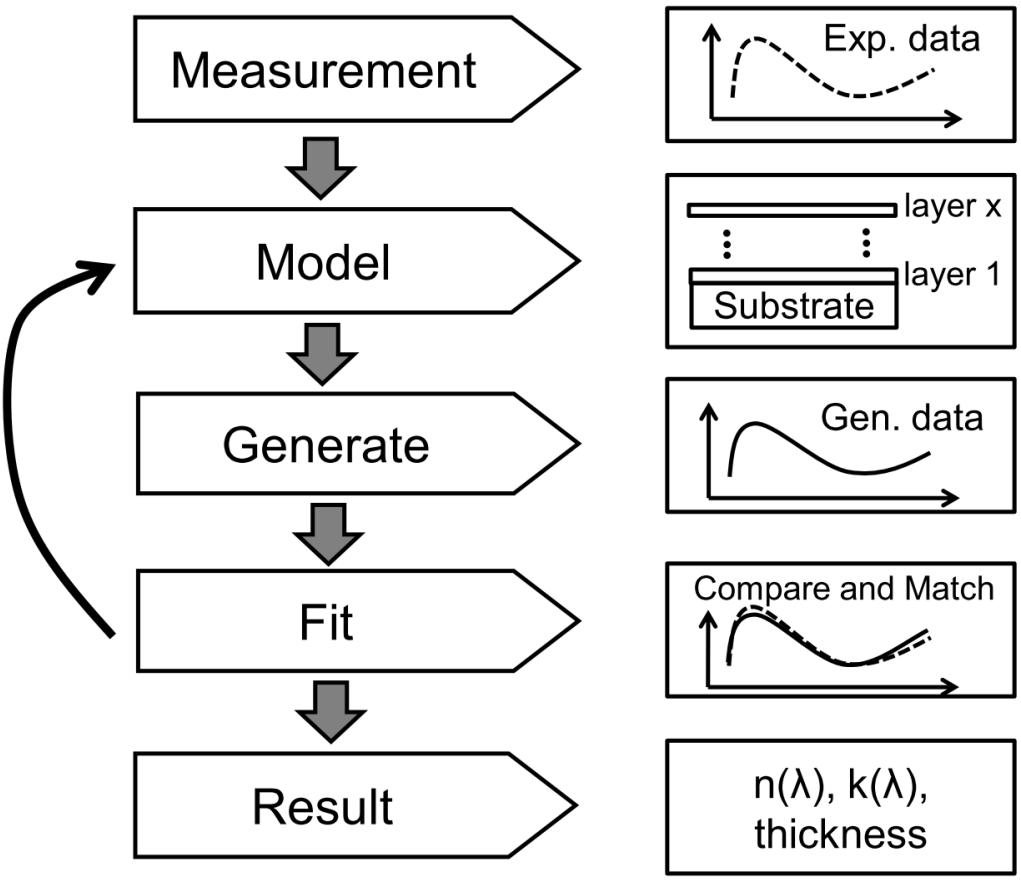

Figure 3.4. Flow chart for the solution process in ellipsometry. Adapted from [73].

constants and the thickness of some layers are unknown, a model is proposed to describe them. There are different models, which are suitable for different type of materials.[75-77] They contain mathematical dispersion equations to describe the dependence of optical constants versus wavelength for several layers. Additionally, the models may describe macroscopically inhomogeneous media (Effective Medium Approximation (EMA)), e.g. metal − dielectric composite, porous and polycrystalline materials.[75,78] They can contain the information about roughness of a surface or interfaces and a thickness gradient. In the next step the data analysis is performed by linear regression analysis. Usually, the Levenberg - Marquardt regression method is used.[76] The predicted values of Δ and Ψ are compared with experimental data. Parameters of a model for layers with unknown optical constants and thicknesses are varied to find the best coincidence between predicted and measured data. The Mean Squared Error (MSE) estimation is used to quantify the

difference between experimental and predicted data.[75,76] As less this value as the result is better.

$$MSE = \sqrt{\frac{1}{2N-M}\sum_{i=1}^{N}\left[\left(\frac{\Psi_i^{Mod}-\Psi_i^{Exp}}{\sigma_{\Psi,i}^{Exp}}\right)^2+\left(\frac{\Delta_i^{Mod}-\Delta_i^{Exp}}{\sigma_{\Delta,i}^{Exp}}\right)^2\right]} \quad (3.2$$

Where N is number of (Ψ, Δ) pairs, M − number of variable parameters in the model, Ψ_i^{Mod} and Δ_i^{Mod} − data calculated from a model, Ψ_i^{Exp} and Δ_i^{Exp} − the set of experimental data, σ − standard deviation for experimental data.

If a reasonably good result cannot be achieved, it may be useful to change or upgrade the model, e.g. to introduce the surface roughness or surface oxide layer, and repeat the routine. Even if a low MSE is achieved, it does not guarantee that the solution is correct. The result may be non-unique if too many models parameters are used for fitting. It is necessary always to justify the result using additional information obtained from other measurement techniques. An educated guess may also help to weed out incorrect results.

Instrumentation for spectroscopic ellipsometry

Nowadays different ellipsometer configurations are available. Each of them has different features and advantages.[74-76,79,80] The null ellipsometer was historically the first ellipsometer. This type has simple construction and can be operated manually. It contains a polarizer and a compensator (quarter-wave plate), which has a ”fast” and a ”slow” axis leading to a phase shift of 90° between the components of electric field strength E along these axes. The quarter-wave plate transforms a linearly polarized light into elliptically polarized. When linearly polarized light is incident on a sample, the reflected light will have in general an elliptical state of polarization. The same elliptical state of polarization with a reversed sense of rotation after reflection from a sample will become a linearly polarized state. With the combination of a polarizer and a quarter-wave plate it is always possible to find an

elliptical polarization that produces a linearly polarized reflection. This linearly polarized state can be determined using the second polarizer as an analyzer after a sample. The beam will be extinguished when the analyzer transmission axis is set perpendicularly to the axis of the linear polarization.

Another class of ellipsometers is a photometric ellipsometer. Photometric ellipsometer construction contains a rotating analyzer or a rotating polarizer. The ellipsometer measures the radiation intensity as a function of periodically modulated azimuthal angle of polarizer or analyzer.

In this work a Rudolph Research spectroscopic ellipsometer S2000 was used. The system consists of a 75 W xenon short arc lamp → collimator → fixed polarizer → rotating polarizer → sample → fixed analyzer → monochromator and photomultiplier, it is so-called PRPSE configuration.[81,82]. The operating range of device is 250 – 850 nm. The angle of incidence was equal to 70° in all measurements. The resulting signal is modulated at 2ω and 4ω, where ω is an angular frequency of rotating polarizer. The ellipsometric parameters tan(Ψ) and cos(Δ) are derived from Fourier coefficients of the second and fourth harmonics of the signal and azimuthal angle positions of fixed polarizer and analyzer.[81,82] Each value of Ψ and Δ was measured 10 times and averaged. The acquired data was analyzed by WVASE32 software.[77] Finally, for the best fit with the lowest MSE the relative standard deviation of film thickness was below 5 % for all experiments.

3.3.2. Fourier Transform Infrared Spectroscopy.

Fourier Transform InfraRed (FTIR) spectroscopy is a fast, and non-destructive technique used to identify functional groups of chemical compounds by their vibrational modes.[16,83-86] This technique employs the interference of two beams to obtain an interferogram, – the signal being a function of the path length between two beams. The interferogram can be transformed to the absorption spectrum, a function of frequency, by the Fourier transform.[87] The principal scheme of an FTIR spectrometer is shown in Figure 3.5.[85] The mid-IR radiation is typically generated by Globar source, as it was in this work. Globar is a thermal light source, which is made of an electrically heated SiC ceramic rod. It emits an IR radiation like approximately a black-body

radiator. The main part of the FTIR spectrometer is the Michelson interferometer, which consists of a beam splitter, a fixed and a moving mirror.

In this work the beam splitter was made from KBr material. Ideal beam splitter reflects 50% of the incident radiation towards the fixed mirror and 50% is transmitted towards the moving mirror. The two beams reflected from the mirrors return back to the beam splitter where they interfere. Finally, 50% of the original light passes into the sample compartment while 50% is reflected back in the direction of the source. When the sample compartment is empty the background interferogram is measured by a detector. When a sample is loaded the background interferogram is affected by absorption bands of a sample compound.

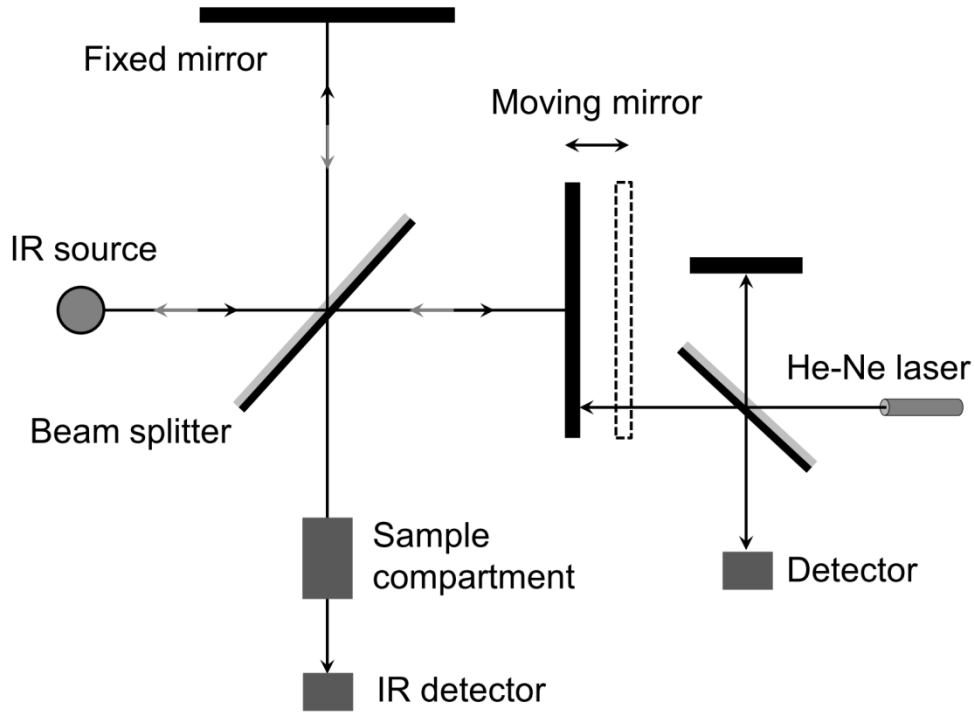

Figure 3.5. Principal scheme of an FTIR spectrometer.

There are two types of detectors commonly used for the mid-IR region: deuterium tryglycine sulfate (DTGS) and mercury cadmium telluride (MCT).[86,88,89] MCT detectors are more sensitive because their high quantum efficiency. The limitation of MCT detectors is that they need to be cooled by liquid nitrogen to reduce noise produced by thermally excited

charge carriers. In this work pyroelectric DTGS detector was employed for measurements. It operates at room-temperature conditions.

Optical path difference (OPD) is the product of the distance difference between the beams travelling through the two arms of an interferometer and the refractive index of the medium in the interferometer. Moving mirror provides the variation of OPD. An interferogram is recorded by the detector as interference signal vs. varied OPD. The second reference interferometer with He-Ne laser (632.8 nm) as a radiation source is used for the detection of position of the moving mirror.[86] The sampling of the main interferogram is triggered in zero-crossings of sinusoidal reference interferogram. This method provides high wavenumber accuracy in the resulting infrared spectrum.

The interferogram I(δ),− the intensity of radiation coming to the detector as a function of the difference in path length δ, can be represented as follows:

$$I(\delta) = \int_{-\infty}^{+\infty} B(\tilde{\nu}) \cos 2\pi\tilde{\nu}\delta \, d\tilde{\nu} \qquad (3.3)$$

It is one-half of a cosine Fourier transform pair. The other shows the variation in intensity as a function of wavenumber $\tilde{\nu}$.

$$B(\tilde{\nu}) = \int_{-\infty}^{+\infty} I(\delta) \cos 2\pi\tilde{\nu}\delta \, d\delta \qquad (3.4)$$

Each of them can be converted into the other by Fourier transformation.

There are three main advantages for FTIR spectrometers over dispersive spectrometers.

1. **The multiplex or Fellgett's advantage**. The signal from all wavelengths is measured simultaneously. It results in a shorter scan-time for a given resolution.

2. **The throughput or Jacquinot's advantage**. The energy throughput in an interferometer can be higher than in a dispersive spectrometer. The FTIR spectrometer does not require entrance and exit slits to improve resolution. The slits restrict the amount of radiation passing through the monochromator. The interferometer throughput is restricted only by the diameter of the collimated beam coming from the source.

3. **Connes advantage.** This advantage arises from the fact that noving mirror position is determined by a reference interferometer with He-Ne laser as a source. The wavelength of the laser is known accurately. As a result, a wavelength (or wavenumber) calibration of FTIR spectrometer is more precise.

Fourier Transform Infrared Reflection Absorption Spectroscopy (FT-IRRAS)

Conventional FTIR transmission techniques allow to measure absorption spectra of various material. However, if a film is very thin the special methods have to be applied to improve the sensitivity. One of such methods, the InfraRed Reflection Absorption Spectroscopy (IRRAS) was employed in this work.[16,86,90-92] In this method the absorption spectrum of a film deposited onto a plane substrate (usually metallic) is obtained at grazing incidence.

Let's consider the situation when the IR light is reflected from a metallic surface (Figure 3.6). It is seen that for an electric field directed across a metal surface an oppositely directed field will be induced. As a result, the net tangential component of electric field in the reflection point is zero. Thus, a film of an absorbing material at the metal surface which thickness is much less than the wavelength of the IR light will not interact with the tangential electric field. For the normal component in the point of reflection the constructive interference will take place and the resulting component of field E_z will be doubled. From the Figure 3.6 it is clear that the closer the angle of incidence to 90° the higher the enhanced electric field in the point of reflection. This is well illustrated by the behavior of the phase shift of the electric field in reflection at different angles of incidence (Figure 3.7). For s-polarized light the phase shift remains at approximately 180°. Another situation is for p-polarized light, for which the phase shift varies monotonically from 180° to 0° as the incidence angle varies from 0° to 90°. The intensity of radiation is proportional to the square of the electric field amplitude. Therefore, for p-polarized light and grazing incidence of light the increase of intensity is nearly four times. Another reason to use grazing incidence for investigations is that the path of beam inside the film with the

thickness d increases as the angle of incidence φ rises like d/cos φ. Robert Greenler calculated in his work that the absorbance of a thin layer obtained by IRRAS at optimum conditions strongly exceeds the absorbance obtained by transmission through the unsupported film at normal incidence.[91]

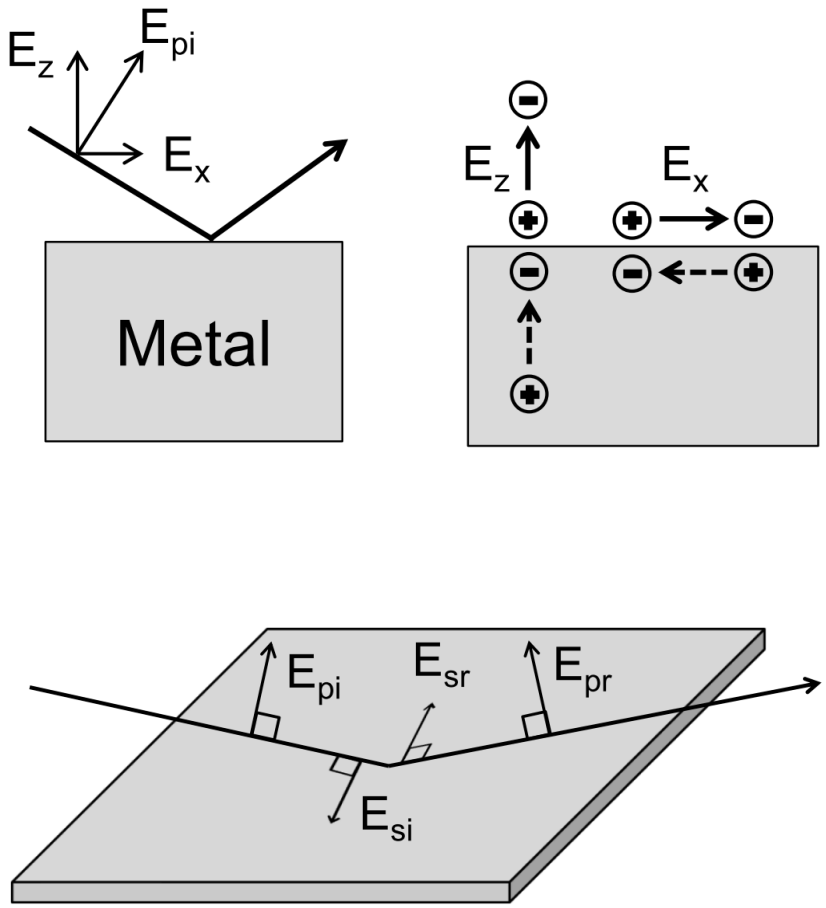

Figure 3.6. Reflection of light from metallic surface. Dashed arrows denote the electric field induced in metal.

Index "pi" is for incident p-polarized beam,
"si" – for incident s-polarized,
"pr" – for reflected p-polarized,
"sr" – for reflected s-polarized.

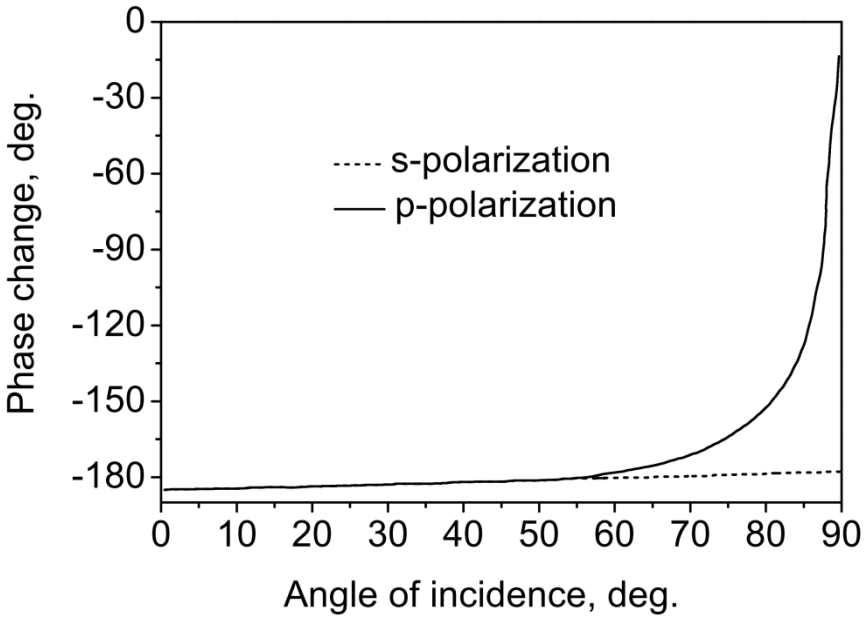

Figure 3.7. Variation of the phase change for an IR beam reflected from metallic surface as a function of the incidence angle. The figure is adapted from [86]

Instrumentation for FT-IRRAS

The IR absorption spectrum of PDMS thin films and the following changes due to the plasma treatment were studied by means of IRRAS. For this the vacuum FTIR spectrometer (Bruker, VERTEX 80V) was applied with a special reflection unit which allows the variation of the incidence angle and the state of polarization. Prior measurements the optical bench and the sample compartment were evacuated to 2 mbar to reduce the absorption of water vapor and CO_2. All spectra were obtained in the wavenumber range from 4000 cm^{-1} to 600 cm^{-1} with the spectral resolution of 0.7 cm^{-1}. In this work all absorption spectra are presented as the decadic absorbance. The IR light was p-polarized. The size of the beam spot on the sample surface at grazing incidence may become larger than the sample dimensions. Moreover, in practice the light propagates to the sample in the cone with the apex angle of 5° – 12°.[16,86] Therefore, for incidence angles close to 90° a part of light will go out of the sample. Thus, the incidence angle of only 75° was selected for measurements.

Optimal settings for FT-IRRAS measurements

Absorbance of thin film vs. incident angle and polarization state

The dependence of peak absorbance for one of the main PDMS absorption bands is presented in Figure 3.8. The other absorption bands show the same behavior up to a constant factor. We see that, as it was expected, the absorbance strongly grows at grazing incidence. At 75° the absorbance amounts to 40 % of absorbance at 88°, which should be the maximal value according the following literature.[16,91,93] Similar behavior was also demonstrated by K. Molt.[94] In this work the absorbance at 75° for all important bands is strong enough for the thinnest investigated films and significantly exceeds the noise level.

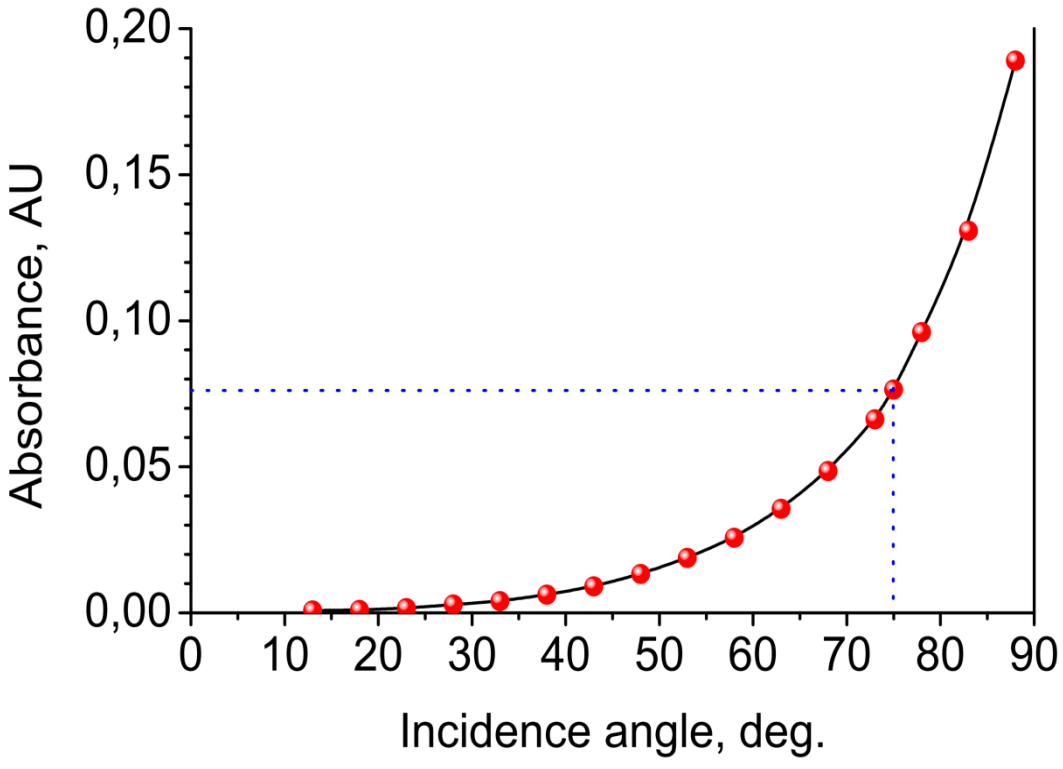

Figure 3.8. The decimal peak absorbance of Si-O-Si asymmetric stretching band as the function of incidence angle. The film thickness is 27 nm; the incident IR light is p-polarized.

Figure 3.9 demonstrates the absorbance as a periodic function of polarization plane orientation. As it was shown in the previous section, for s-polarization the change of phase is near 180°, which results in the absence of absorption for thin films. On the contrary, in the case of p-polarization the absorbance is maximal because of constructive interference in the point of reflection.

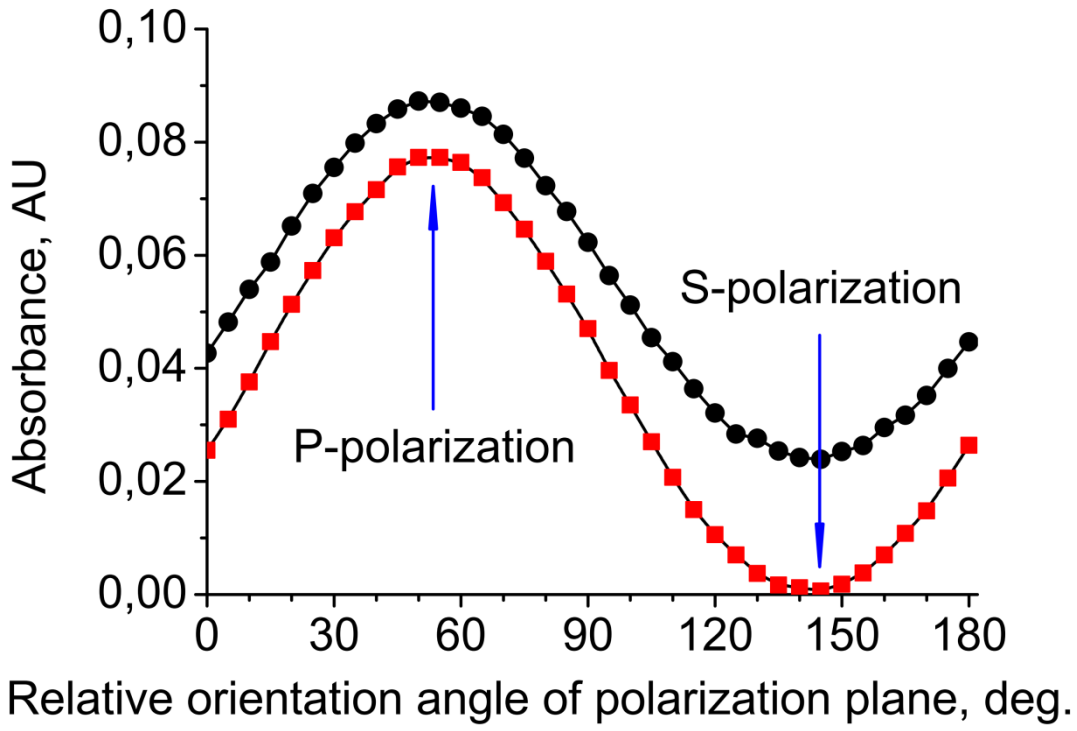

Figure 3.9. Decimal absorbance of the band peak as a function of orientation of the polarization plane at the incidence angle of 75°.

Red squares: Si-O-Si asymmetric stretching at 1112 cm^{-1} (~ 8990 nm). The film thickness is 27 nm. Black circles: CH_3 asymmetric stretching at 2965 cm^{-1} (~ 3370 nm). The film thickness is 310 nm.

As the film thickness comes closer to the IR radiation wavelength an additional absorption of the bulk takes place, which is similar with the absorption regime in the standard transmission measurements. For very thick films the bulk absorption will dominate. In our case the film thickness does not exceed 1 μm. Thus, both, the absorption from the layer near the interface metal - film and from the bulk, can make a comparable contribution to the absorbance (it depends on relation between IR radiation wavelength and film thickness). In this case the resulting absorbance is also a periodic function, but it is not equal to zero at s-polarization as demonstrated in Figure 3.9. However, even in this case

the p-polarized light remains the most advantageous case for measurements.

3.3.3. Scanning electron microscopy (SEM)

The scanning electron microscopy utilizes a high-energy electron beam to produce different signals at a sample surface. Among these signals are x-rays, secondary and backscattered electrons. Their analysis provides information about surface morphology, chemical composition, and crystalline structure of sample material. The electron beam scans the surface in a raster mode. As the result, the detected signal in combination with the beam position provides the information to build a surface image. In this work Zeiss Supra 40 VP microscope was used for experiments described in the Section 4.4.1. To prevent an accumulation of negative charge on the surface, a golden layer of the thickness of ca. 10 was deposited on the sample by magnetron sputtering. An in-lens detector was used to collect secondary electrons.

3.4. Preparation of Thin Polydimethylsiloxane (PDMS) Films

3.4.1. Physical Properties of PDMS

Polydimethylsiloxane (PDMS) belongs to a group of inorganic polymers, which are called linear siloxanes. Their backbone is a chain of alternating silicon and oxygen atoms. In addition, each silicon atom in PDMS is bonded with two methyl groups. The backbone can be terminated by various groups, in our case it always will be the trimethylsiloxy group (see Figure 3.10).

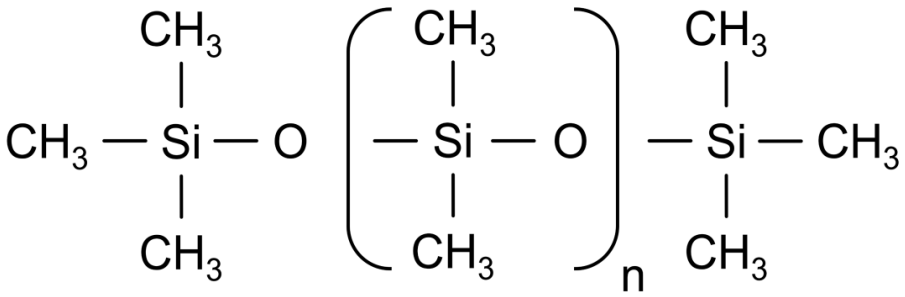

Figure 3.10. Chemical structure of trimethylsiloxy-terminated polydimethylsiloxane.

At ambient conditions the polymer can be a pourable or viscous liquid and rubberlike solid material. Because of weak intermolecular forces the polysiloxanes remain liquid over a very wide range of molecular weights. They are insoluble in water, their physical properties, such as viscosity and thermal conductivity, depend weakly on the temperature.[95-97]

The compound with n = 0 is called hexamethyldisiloxane (HMDSO, see Figure 3.10). As it is seen from Table 3.2, it has the smallest density and viscosity. With the increase of the monomer unit number n the polymer chains become loosely entangled and the kinematic viscosity grows. It ranges from 0.65 cSt for the shortest possible chain (HMDSO) to more than $2 \cdot 10^7$ cSt for elastomers with high polymerization degree. [97] At molecular weights above 10000 the PDMS molecules become entangled and the polymer exhibits a viscoelastic response.

Thermal stability

The strong difference of the electronegativities for Si (1.9) and O (3.44) leads to a very polarised Si-O bond, highly ionic and with a large bond-dissociation energy, 5.9 eV.[98] This results in considerable thermal stability to PDMS, the degradation starts at ambient conditions only at temperatures exceeding approximately 350 °C.[98-100] The Si-O bonds are much more strong than the C-C bonds of carbon based polymers (C-C dissociation energy ~ 3.6 - 3.9 eV), which are, therefore, less durable to thermal degradation.[101] This makes PDMS very attractive to use in high-temperature applications, e. g., lubricant for brake components and heat transfer fluids. In this work the sample temperature during the plasma modification did not exceed 60 °C. Thus, no thermal decomposition of PDMS films takes place.

High permeability for different compounds

Membranes made of PDMS have high permeability coefficient for oxygen, nitrogen and other gases, which is attributed to the large free volume of the compound.[102-106] The cornea receives oxygen normally by diffusion from atmosphere rather than from blood vessel, and, therefore, soft contact lenses contain sometimes siloxanes.[107] PDMS is permeable to different organic vapors even more than to oxygen and nitrogen. This makes it useful for cleaning of air or decontamination of water by pervaporation.[108,109]

Table 3.2. Properties of polydimethylsiloxanes with different monomer unit number in the chain.

Approximate Molecular Weight, M_n	Calculated number of monomer units, n	Kinematic Viscosity, cSt, 25 °C	Density, g/cm^3, 25 °C	Refractive Index, n_D 25 °C
162	0	0.65	0.758	1.3748
384	3	2	0.868	1.3902
1200	14	10	0.937	1.399
1900	23	20	0.947	1.400
3700	48	50	0.952	1.402
6700	88	100	0.965	1.403
11300	151	200	0.968	1.4031
15800	210	350	0.969	1.4032
19000	255	500	0.969	1.4033
26400	355	1000	0.971	1.4035
35000	471	2000	0.971	1.4035
63400	855	12500	0.974	1.4035
91700	1237	30000	0.976	1.4035
116500	1572	60000	0.976	1.4035
139000	1876	100000	0.977	1.4035

Data is taken from [96,98,110,111]. Number n is calculated from the molecular weight according $n = \frac{M_n - 162}{74}$

Physiological compatibility and medical use

Silicone is a suitable material for use in medical applications. It is non-toxic and has excellent physiological compatibility with human tissue. Therefore, it is used for artificial organs, prostheses, objects for facial reconstruction, tubing and catheters, and vitreous substitutes in the eyes.[112,113] Simethicone, a mixture of polydimethylsiloxane and hydrated silica gel, is an anti-foaming agent that helps to reduce bloating, discomfort and pain caused by excess gas in the stomach. It decreases

the surface tensions of gas bubbles and joins them so that gas is more easily released away.[114]

Optical transparency and resistance to oxidation and photo-ageing

PDMS is optically transparent in UV and visible regions.[115-118] Because of this reason, it suits for the fabrication of waveguides.[119] Some other polymers absorb UV light, which initiates their chemical changes. Under solar radiation at ground level PDMS oxidizes very slowly and show relatively little change in physical properties. It was shown in experiments [120] that silicone elastomers survive the natural ageing conditions very well. Even after 20 years bent loop elastomers in the most cases were still intact and uncracked at temperate climate conditions. However, the hot-wet jungle climate caused considerable damage. Good sustainability to photo-ageing and, additionally, high electric resistivity ($4x10^{13}\ \Omega \cdot m$ [102]) makes PDMS elastomers ideal to use as high voltage outdoor insulators. [121]

3.4.2. Preparation of PDMS/HMDSO mixture

The focus of this work is directed on the plasma treatment of PDMS films with the thickness ranging from ten to several hundreds of nanometers. Al-covered glass slides with the size of 26×60 mm were used as substrates, for a part of experiments they were substituted to Si polished wafers (Cemat Silicon S.A., (111) crystalline orientation) of the same size. The metallic film with the thickness of about 150 nm, deposited on the glass slide, play the role of the reflective layer used in Fourier Transformed Infrared Reflection Absorption Spectroscopy (FT-IRRAS). It was applied by the evaporation of Al wire in vacuum. The wire was placed inside the tungsten coil and heated by current in the range between 1 and 2 A. Before the evaporation process the chamber was evacuated to the pressure of $3 \cdot 10^{-4}$ mbar to avoid the oxidation of Al. The film deposition on the Al layer is performed by spin-coating, for that the liquid PDMS in the form of SILFAR® 1000 (Wacker Chemie GmbH, Germany) was used. Its mean kinematic viscosity is about 1000 cSt. To reach the required diapason of thickness it is necessary to decrease the original viscosity. For this reason PDMS was mixed with HMDSO (Fluka Chemie AG, purity ≥ 98.5 %) in various volume proportions of

PDMS/HMDSO ranging from 1/5 to 1/250. Initially these mixtures were stored in glass flasks with rubber stoppers over the long period for regular use. During storage the original transparent liquid became straw-colored. Figure 3.11 shows the alteration of the IR absorption spectrum. The appearance of CH_2 group was seen already after 2 weeks, further its concentration was increasing gradually. From the set of the appeared peaks one can suggest that the formed structure is likely $\equiv Si\text{-}CH_2\text{-}CH_n\text{-}CH_3$. The progressed alteration was observed over one month.

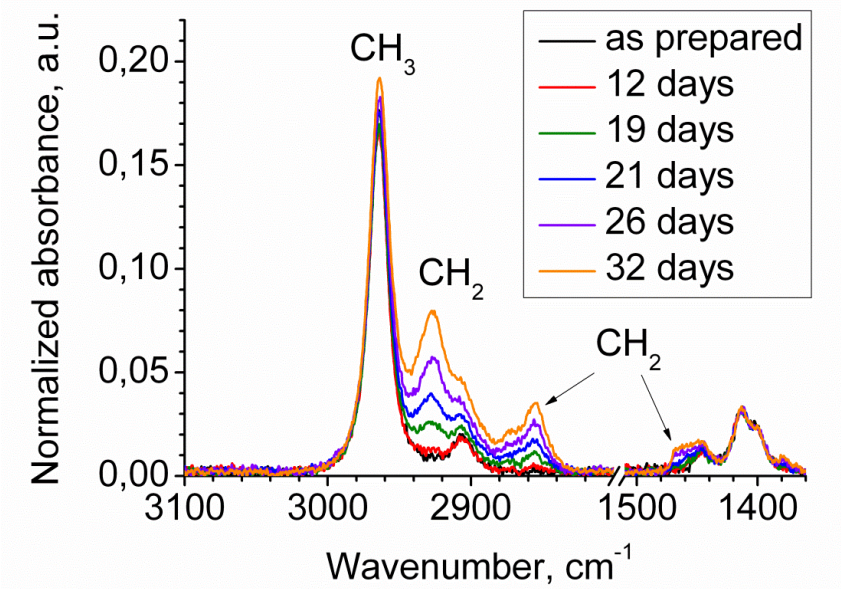

Figure 3.11. Normalized IR absorbance of PDMS films with the thickness of ca. 85 nm. The films were prepared from mixture stored in a flask with rubber stopper after various periods. The spectra normalization is done for $Si\text{-}CH_3$ symmetric deformation vibration peak at 1265 cm^{-1}, which is absent here.

This modification is due to the interaction of mixture with stopper: it evaporates, reacts with the stopper and flows down. To overcome this problem rubber stoppers were changed to polyethylene (PE) ones. In Figure 3.12 are liquids stored in flasks with 2 different stoppers: with PE stopper neither yellowing nor alteration of IR absorption spectrum is observed over at least one year. Another problem for the mixture preparation was the presence of transparent globular particles in SILFAR 1000 (see Figure 3.13). The size of particles varied between 5 and 15 μm. FTIR analysis of the liquid showed the absence of other chemical compounds. Therefore, most probably, these spherical particles are solid agglomerates of entangled long-chain PDMS molecules. If such non-

filtered film is modified in H_2 CCRF discharge, globular inclusions become solid together with the film. In the places of solidified globular particles the film is fragile. Slight rubbing removes them leaving numerous holes in the film. To avoid this problem the silicon oil SILFAR 1000 was filtered through the disposable vacuum filtration system VACUFLO with 0.2 µm cellulose-mixed-ester membrane (Whatman Schleicher & Schuell). As a result, the liquid was clean of any microparticles.

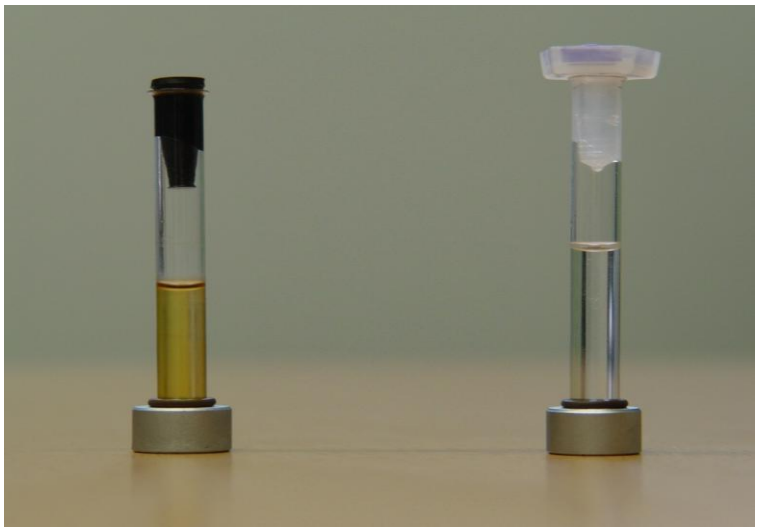

Figure 3.12. Photograph of PDMS/HMDSO mixtures stored over one year in a flask with rubber (straw liquid) and PE stopper (transparent, unmodified liquid).

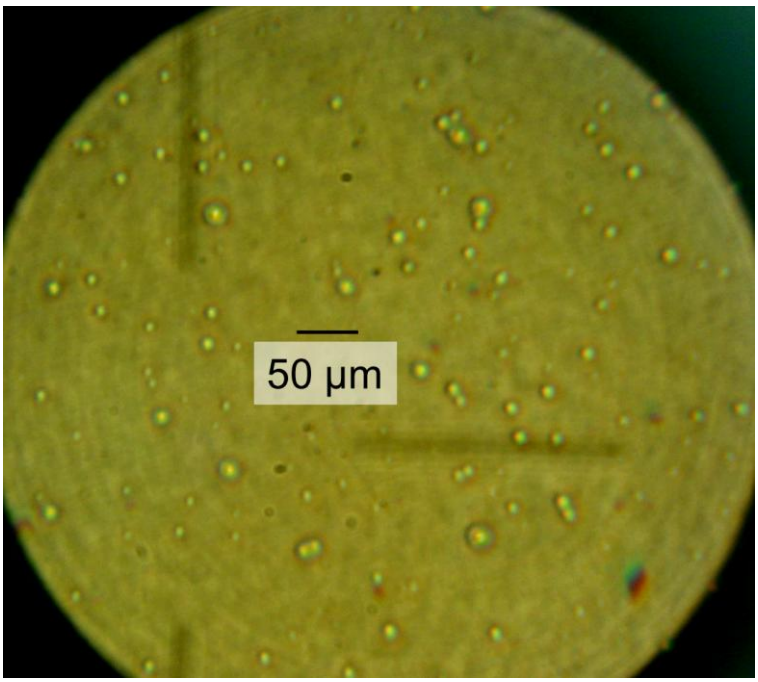

Figure 3.13. Micrograph of non-filtered silicone oil SILFAR 1000.

3.4.3. Spin-coating

For spin-coating a self-made device "Mister Twister" was manufactured. The stationary part contains a current circuit with a coil. The rotating platform has two magnets disposed diametrically opposite. Each time a magnet goes past the coil the excited current is registered by an oscilloscope, this way the setup measures the frequency of rotation. In the deposition process it is between 7600 and 7800 rpm. The drop of mixture with the volume of 20 μL is deposited in the time of spinning. It is enough to cover the entire surface of the substrate by a homogeneous film. The thickness decreases rapidly versus the spin time and reaches quickly a constant level after about 10 s.[122,123] For convenience the spin time was set to 30 seconds in all procedures. In stored mixtures more heavy PDMS molecules go the bottom of flask. Therefore, just before the deposition the mixture is stirred to avoid the separation of PDMS and HMDSO.

Figure 3.14 demonstrates the behavior of the thickness versus the relative content of PDMS in the drop by volume, which is proportional to the concentration of PDMS in the mixture. The explanation of the behavior, supported by theory and experimental results are given in the article of D. Schubert and T. Dunkel.[123] They distinguish three regimes

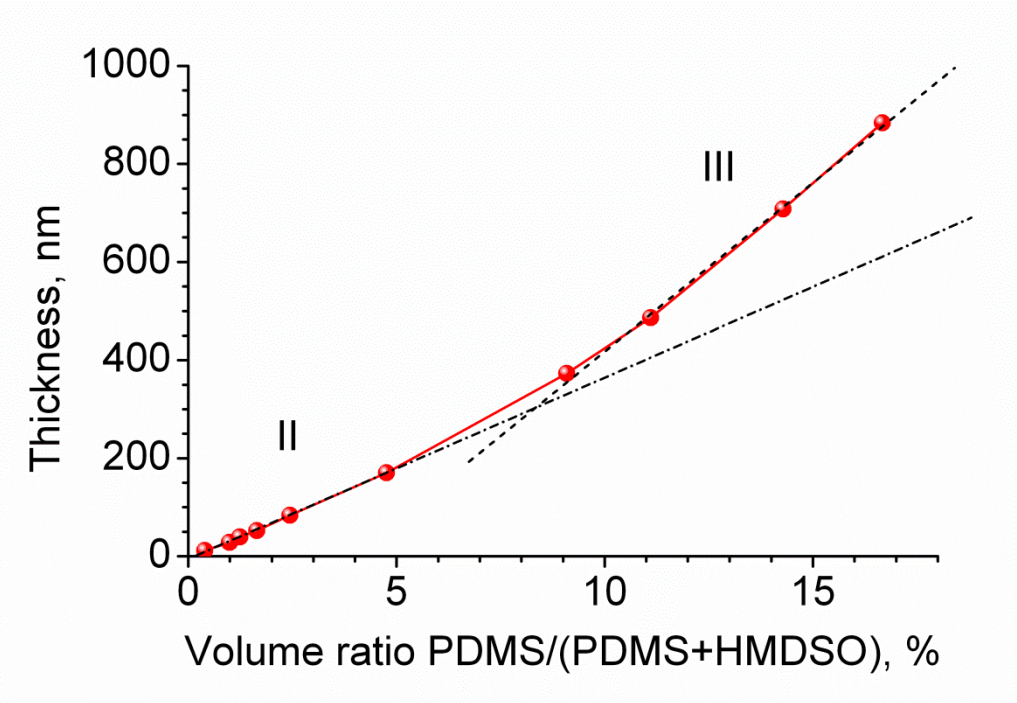

Figure 3.14. Thickness of spin-coated films vs. relative content of PDMS in the drop. Dash-dotted line is for regime II, dashed describes regime III.

of the film formation corresponding to three different ranges of solution concentrations. Regime I denotes the case where the film cannot be deposited. It happens if the concentration of PDMS is so small that its molecules do not overlap with each other to form continuous film during the spin coating process. They are washed off the substrate together with the solvent. In Figure 3.14 this region absents. Apparently, the value of minimal concentration, which is necessary for film formation, is so small that it cannot be defined from the plot. In regime II, at concentration higher than minimal one the film can be deposited. Here, the film thickness is proportional to the volume ratio until it is less than 5 %. The concentration of PDMS is already high enough for the efficient formation of the film since some spinning time. In regime III the situation is similar. But due to higher concentration of PDMS in HMDSO the interaction of molecules starts since very beginning of spinning, less PDMS is washed off the substrate and the film thickness increases faster.

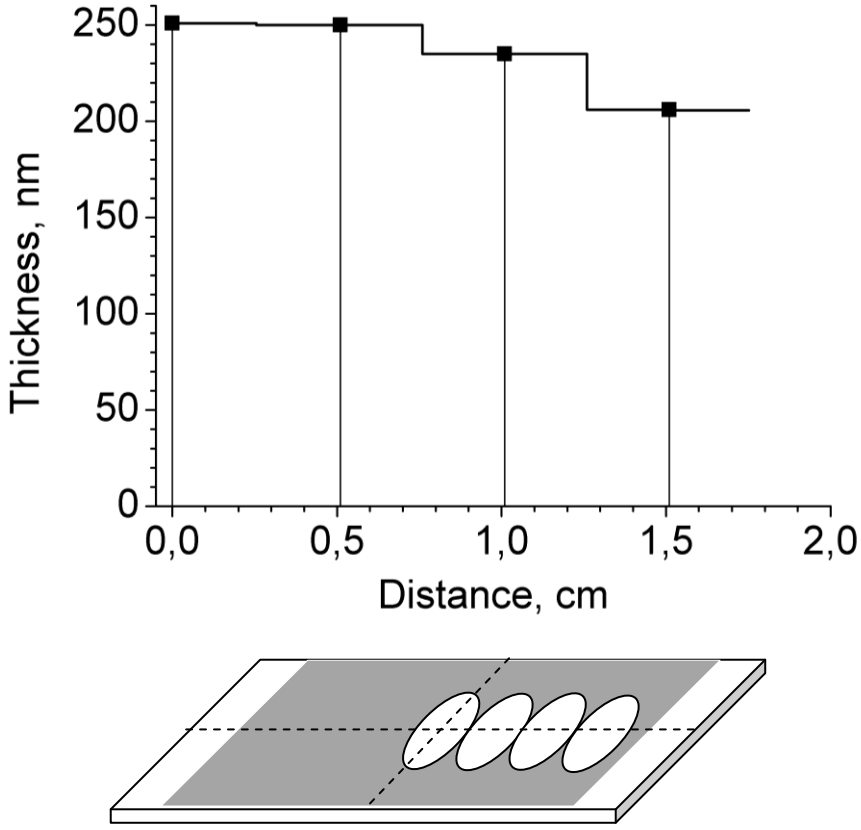

Figure 3.15. Thickness profile of a spin-coated film and scheme of beam spot positions in the measurements of thickness by the spectroscopic ellipsometry.

The centrifugal force is responsible for the dispensation of liquid over the surface. It increases linearly versus the radial distance, and, therefore, the thickness profile of a film is not uniform along the whole radial direction. The absolute film thickness measured by spectroscopic ellipsometry (SE) at different positions is presented in Figure 3.15. The length of the rectangular area covered by PDMS is 4 cm, the width is 2.5 cm. The film thickness averaged over an elliptical beam spot was measured in four positions (see Figure 3.15). Major axis of an ellipse was 1.5 cm long, minor - 0.25 cm. It is seen that the thickness varies weakly within the circle with the radius of 1 cm. Beam spots of any experimental technique used in this work were located in the substrate center and always were inside this quasi-uniform area.

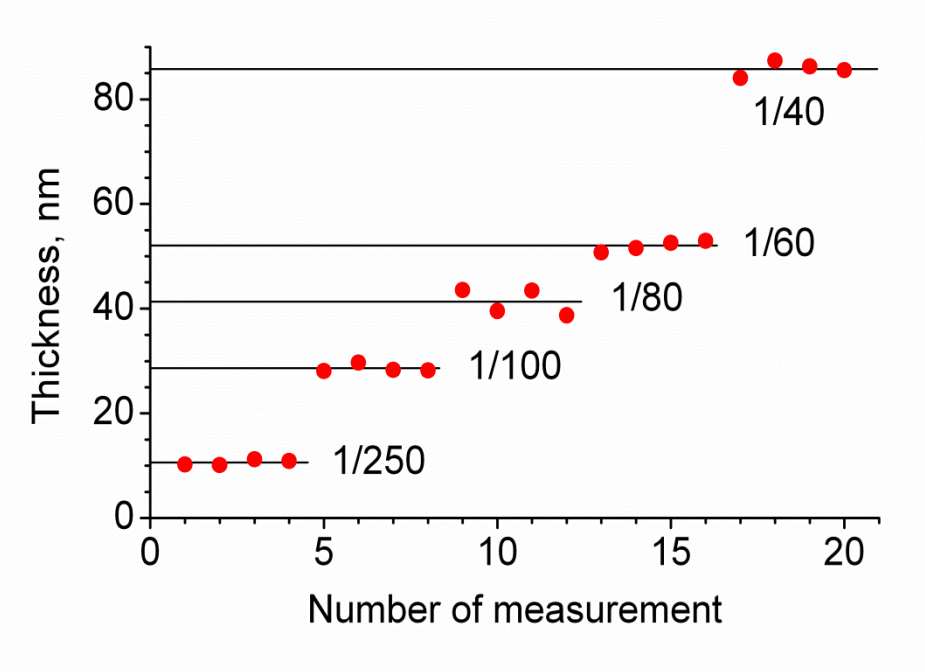

Figure 3.16. Variation of film thickness in series of four spin-coatings for different mixtures of PDMS/HMDSO (1/40, 1/60, 1/80, 1/100, 1/250). Horizontal lines show the average of each series.

As it can be seen from the Figure 3.16 the thickness deviation is small, when one mixture is used for all spin-coatings in the series. Relative deviation from an average does not exceed 10%, and the reproducibility of the sample preparation is good.

In conclusion, it is demonstrated that a mixture of HMDSO and PDMS can be stored over very long time period without any chemical modification. The spin-coating method is characterized by

- short time of deposition process
- reasonably good uniformity of thickness
- good reproducibility of film thickness for a series of depositions
- very low consumption of material.

4. Experimental results and discussion

The information about internal plasma parameters and processes is crucial to select main factors affecting on the modification process of PDMS coatings. Going from this information the potential of the innovative method to produce thin film coatings with nanoparticles can be understood and the plasma processing can be optimized.

4.1. Influence of different plasma components in the interaction with PDMS

In the direct hydrogen plasma treatment different components, which modify thin PDMS films, have to be considered: neutral atoms and molecules, radicals, ions (H^+, H_2^+, H_3^+) and the VUV radiation. The penetration depth of particles is very limited. For example, the interaction of atomic hydrogen with amorphous hydrogenated carbon (a-C:H) films was studied by von Keudell et al., and the depth of H atom penetration into a-C:H film was estimated to 2 nm. [124] The interaction depth of impinging ions from hydrogen plasma is also very low. In the main experiments the PDMS sample was at floating potential. The electric probe measurements have shown that the typical difference between plasma and floating potential does not exceed $10-20$ V (see Figure 4.12). This means that the maximum kinetic energy of positive hydrogen ions bombarding samples was in the order of 10 eV. As it will be shown later the near-surface region of PDMS films is very rapidly transformed into a SiO_x layer upon the plasma treatment. The TRIM (Transport of Ions in Matter) simulations demonstrated for H^+ ions striking the SiO_2 material the penetration depth of 3 nm for 10 eV monoenergetic ion flux.[125] Even for significantly higher ion energy of 100 eV the penetration depth is only 10 nm. It was also verified that there is no etching or sputtering of the top SiO_x layer in the experiment. For this, the PDMS films of 10 nm thickness were prepared and treated in the hydrogen discharge. After at most 30 s the whole film is converted in a methyl-free SiO_x layer. The following extended plasma treatment up to 30 min showed no further thickness reduction.

Thereby, particles in plasma cannot modify bulk of films with a thickness of hundreds nanometers. However, their contribution in the modification of top near-surface region is important as it was shown in the following works.[41,126,127]

On the other hand, the VUV radiation has typical penetration depths in the order of few hundred nanometers.[128,129] The dissociation energies of chemical bonds in PDMS amount to about 4.2 eV for C-H, 3.4 eV for Si-C and 5.9 eV for Si-O.[130,131] The photon energy of the H_2 plasma corresponding to the VUV range and over the cut off (115 nm for MgF_2 window) is in the range between 6 and 10.8 eV. Hence, the VUV photons are able to cleave chemical bonds and initiate photochemical reactions in the PDMS film.

4.2. VUV radiation of capacitively coupled low-pressure discharge in H_2, O_2, Ar, Xe and H_2O.

Different gases were used to investigate, for which of them the plasma produces the most intensive VUV radiation. For that the capacitively coupled discharge was ignited in a glass reactor at low-pressure and the excitation frequency of 165 kHz.

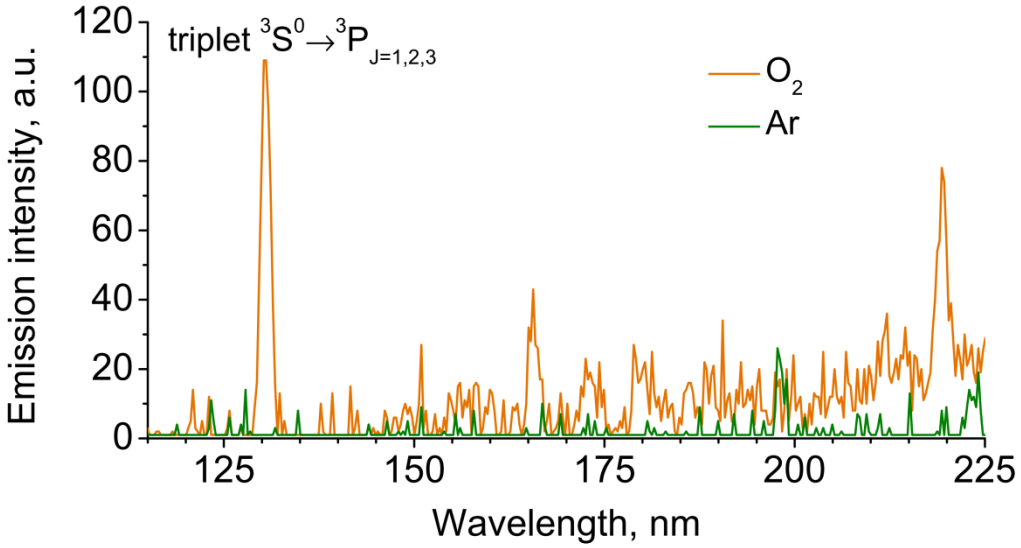

Figure 4.1. VUV emission spectra of the O_2 and Ar discharge (excitation frequency 165 kHz, forward power 10 W, pressure 27 Pa).

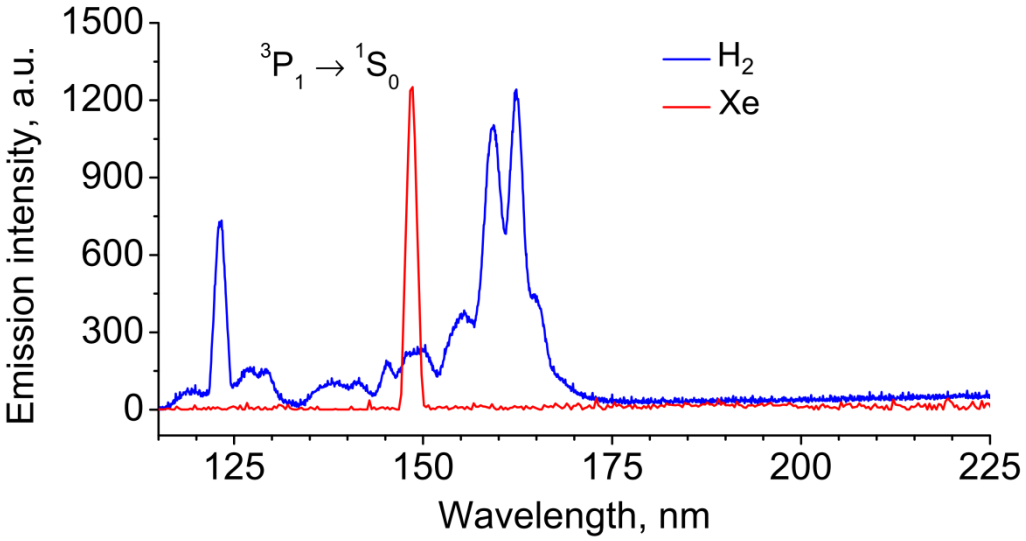

Figure 4.2. VUV emission spectra of H_2 and Xe discharge (excitation frequency 165 kHz, forward power 10 W, pressure 27 Pa).

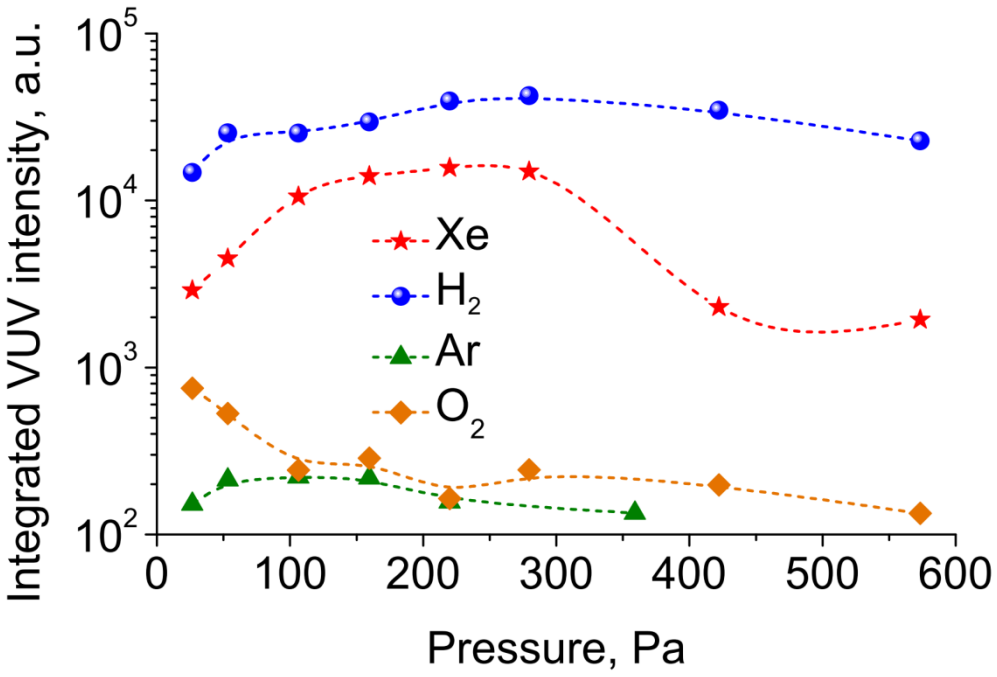

Figure 4.3. Integral emission intensity between 115 and 200 nm versus gas pressure for O_2, Ar, H_2 and Xe discharge (excitation frequency 165 kHz, forward power 10 W, pressure 27 Pa).

The excitation frequency of discharge, described in this section, is less than that of discharge, where films were treated (165 kHz vs. 13.56 MHz). Nevertheless, qualitative relations between the VUV

emission intensity of O_2, Ar, H_2 and Xe plasmas are similar for both mid-frequency and radio frequency discharges.[132,133] The argon discharge demonstrates minor emission in the range between 115 and 200 nm as it can be seen in Figure 4.1. It is known, however, that Ar plasma has strong emission lines at 104.8 and 106.7 nm.[134-136] For these wavelengths, as it will be shown later, the penetration depth into PDMS is very limited. In test experiment it was confirmed that the bulk of PDSM films is not affected by VUV radiation of the Ar plasma. For the top layer of ca. 10 – 30 nm the modification effect was similar with those of H_2 plasma. Oxygen atoms in plasma emit weak resonance triplet lines around 130.4 nm.[132,133,137-139] Its intensity further decreases with increasing pressure from 27 to 575 Pa. The low-pressure discharge in Xe exhibits only one, but strong emission line at 147 nm (Figure 4.2). However, Xe is an expensive gas to use it industrial plasma technologies. Furthermore, it loses in comparison with H_2 discharge, which demonstrates continuous emission in the VUV range (Figure 4.2). Figure 4.3 represents the integrated VUV emission intensity in the region 115 – 200 nm. It is seen that the absolute champion is H_2 plasma, which shows the strongest integral intensity at all pressures in the range between 27 and 575 Pa. The flat maximum of the integral H_2 emission intensity is between about 250 – 300 Pa.

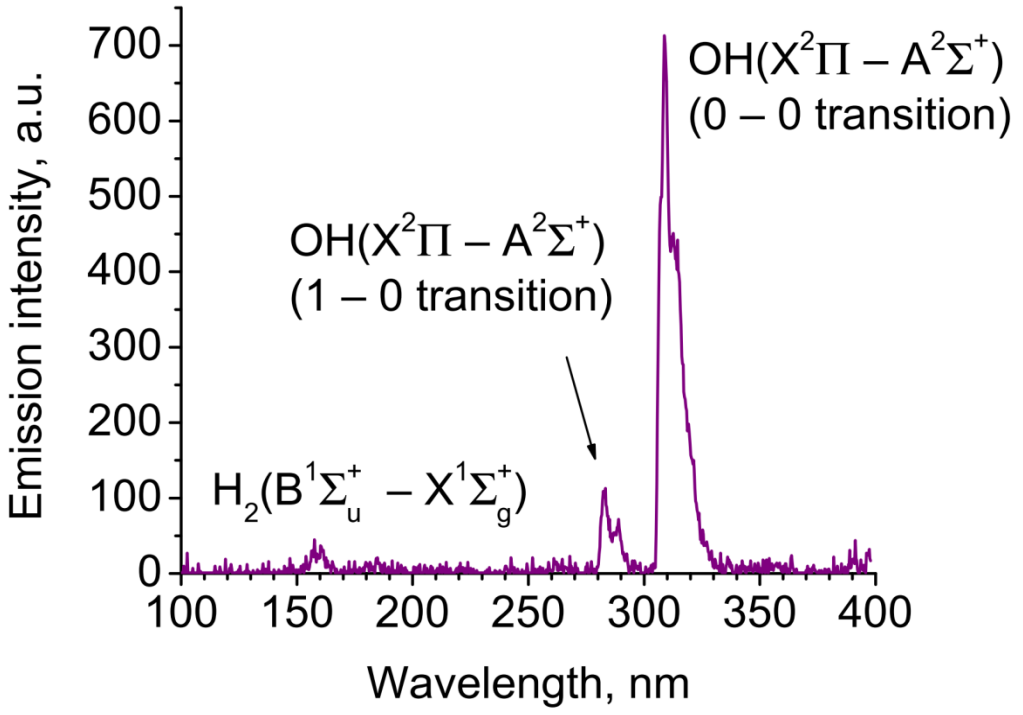

Figure 4.4. VUV emission spectrum of H_2O discharge (excitation frequency 165 kHz, pressure 55 Pa and forward power 10 W).

Another potential candidate for the treatment of thin PDMS films was the low-pressure discharge in H_2O. However, it showed the strong emission only in the less energetic UV region (peaks at 283 and 309 nm) due to the transition $X^2\Pi - A^2\Sigma^+$ for OH radical (see Figure 4.4). The molecular hydrogen emission in H_2O discharge in the VUV region is very weak. Its integrated value for example shown in Figure 4.4 is only about 1% of that in H_2 discharge at the same pressure and forward power.

4.3. CCRF hydrogen discharge for plasma-chemical modification of thin PDMS films

4.3.1. Electron energy probability function.

Well-defined plasma processing of material requires information about the internal plasma parameters. Electric probe measurements provide us floating and plasma potentials, the electron energy distribution function (EEDF) or the electron energy probability function (EEPF, ($EEDF = \sqrt{E} * EEPF$)), from which it is possible to calculate electron concentration n_e and electron mean energy (or effective electron energy T_e). The setup, described in Chapter 3, measures probe current as a function of probe voltage. A typical current-voltage (I-V) characteristic curve is presented in Figure 4.5. It can be divided into three regions. When the voltage is sufficiently negative, the probe collects mostly positive ion current, which is called the ion saturation current. To the right from this region, at more positive voltages, positive ions and electrons contribute to the probe current. This region is called the transition region. The voltage at which the electron current compensates the positive ion current, defines the floating potential V_{fl}. Further increase of the positive probe potential repells more and more positive ions. Firstly, the plasma potential will be reached, at which no plasma sheath exist and the electron collection corresponds to wall current according to their EEDF. Shortly after, the curve will go into the electron saturation region. Basically, the shape of this part of I-V curve depends on the probe geometry. In the electron saturation region the electron flux remains constant, but the probe sheath thickness growth continuously with increasing probe voltage. Therefore, the electron current rises with increasing voltage for cylindrical or spherical probe tip, and remains constant for a planar probe geometry. The knee, which approximately defines the position of plasma potential V_{pl}, is distinct for a planar probe,

round-off for a cylindrical probe and absents for spherical one. In practice, the plasma potential is derived as the position of inflection point from the zero value of the second derivative of the I-V curve.

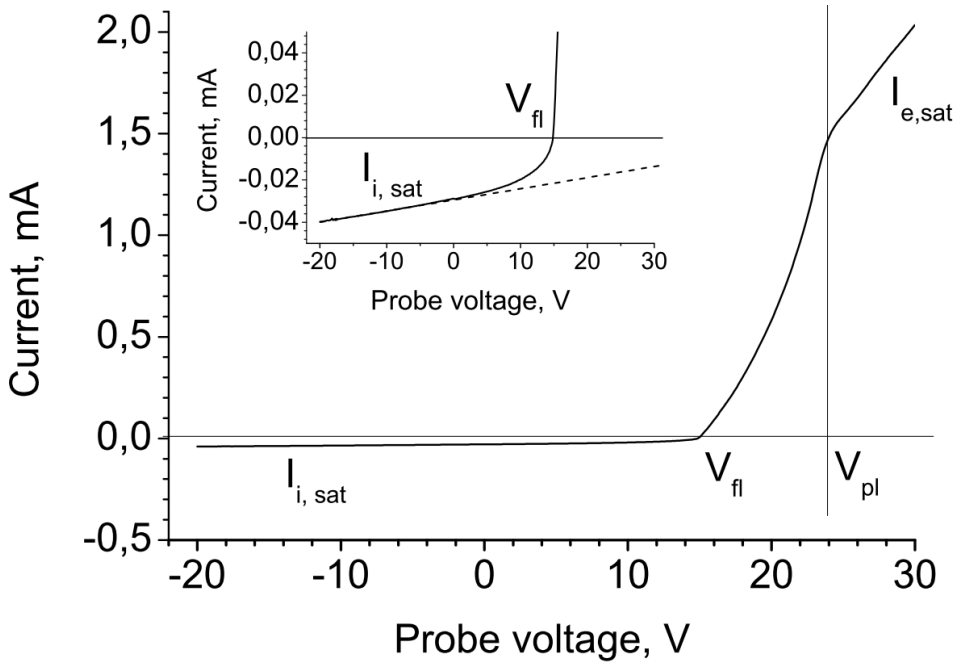

Figure 4.5. Typical I-V curve of a cylindrical probe in hydrogen RF plasma discharge (27 Pa, 200 W). The subplot plot demonstrates the same curve in the ion saturation region.

In this work the determination of EEDF from I-V curves is based on the Druyvesteyn method.[140] Additionally to that theory, practical and technical guidance for the probe diagnostics can be found in following works. [72,141-154] The Druyvesteyn method ideally should be applied in the collisionless regime, when electron mean free path is much less than the sum of characteristic probe dimension and probe sheath thickness. The data on collision cross-sections can be found elsewhere.[59,60] The sheath thickness can be estimated from the following formula [58,155]:

$$h \approx 1.1 \cdot \lambda_D \left(\frac{e|V|}{k_B T_e} \right)^{3/4} \qquad (4.1)$$

Where V is the probe potential relative to plasma potential V_{pl}.

For a typical electron temperature of 3.5 eV and electron concentration of 10^{10} cm^{-3} λ_D equals to 140 μm. Then for V equal to a typical value of

floating potential V_{fl} = 8 eV, we have h = 285 μm. The characteristic probe dimension for cylindrical probe is given by the following expression:

$$d = R\ ln\ \frac{\pi L}{4R} \tag{4.2}$$

Taking into account the probe radius R = 72 μm and length L = 5 mm the characteristic probe dimension results in d = 290 μm. In Figure 4.6 the mean free paths of electrons for different pressures are compared with the sum d + h.

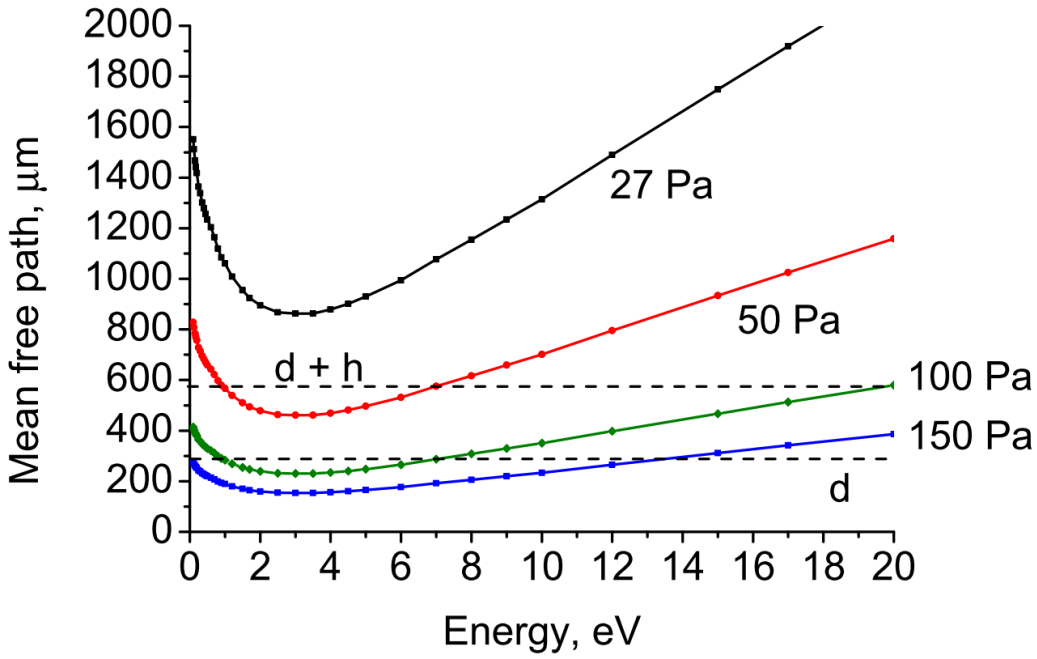

Figure 4.6. Mean free path of electrons related to elastic collisions for different pressures and compared with the probe dimension d and the sheath thickness h. The data on cross-section is taken from Yoon [60].

It is seen that no ideal collisionless regime takes place for all pressures. It means that calculated EEDF will have differences with real one, and as the pressure is higher as the difference will be stronger. The influence of relation between the probe geometry and the electron mean free path on the deviation of EEDF derived by the Druyvesteyn method from some model EEDF was investigated in [156,157].

4.3. CCRF hydrogen discharge for plasma-chemical modification of thin PDMS films

According to the Druyvesteyn method the electron energy probability function f_p(eV) can be evaluated from the second derive of the I-V curve:

$$f_p(\mathrm{eV}) = \frac{2\sqrt{2m_e}}{e^3 S} \cdot \frac{d^2 I_e}{dV^2} \qquad (4.3)$$

Here, V is with respect to the plasma potential. S is the probe area.

From EEPF the effective electron temperature T_e and the electron concentration n_e can be calculated.

$$n_e = \int_0^\infty f_p(\varepsilon) \cdot \sqrt{\varepsilon}\ d\varepsilon \qquad (4.4)$$

$$T_e = \frac{2}{3}\langle\varepsilon\rangle = \frac{2}{3n_e}\int_0^\infty f_p(\varepsilon) \cdot \varepsilon^{3/2}\ d\varepsilon \qquad (4.5)$$

It has been found that EEPFs in H_2 discharge are neither Maxwellian nor Druyvesteyn under the investigated discharge conditions. Figure 4.7 shows the effect of discharge power on the EEPF in H_2 RF discharge at the pressure of 26.7, 50, 100 and 150 Pa. With the increase of pressure the measurements of EEPFs at low forward powers were technically unable. The plasma potential shifted to more positive values, and the attempts to reach it by the probe potential caused always the glowing in the sheath around the probe. In this mode a part of the I-V curve was inappropriate for analysis.

A second peak in EEPFs is observed under most discharge conditions. Its position drifts to higher energies when the forward power is decreased (see Figure 4.8). In the same time the second peak decreases. When the gas pressure is increased, the second peak shifts stronger to higher energies with decreasing RF power. A similar second peak and dependence on process parameters were observed by Hong Li in ICP discharge in N_2 at 0.7 and at 13.3 Pa, and in H_2 in the pressure range 0.7 – 6.7 Pa.[158] In another work the second peak was observed by Mahony et al. in CCRF discharge at 13.56 MHz.[159] The operating pressure was in the range from 33 to 133 Pa. The time-averaged electron energy probability functions were measured in H_2 and D_2 discharges using a passively compensated Langmuir probe technique like in this work.

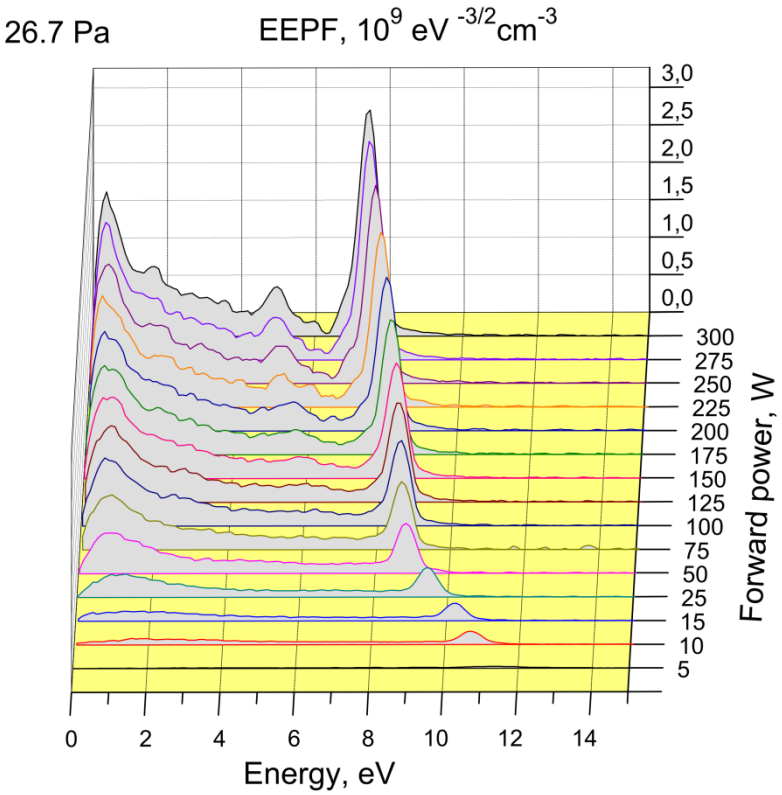
26.7 Pa
EEPF, 10^9 eV^-3/2 cm^-3
3,0
2,5
2,0
1,5
1,0
0,5
0,0
300
275
250
225
200
175
150
125
100
75
50
25
15
10
5
Forward power, W
0
2
4
6
8
10
12
14
Energy, eV

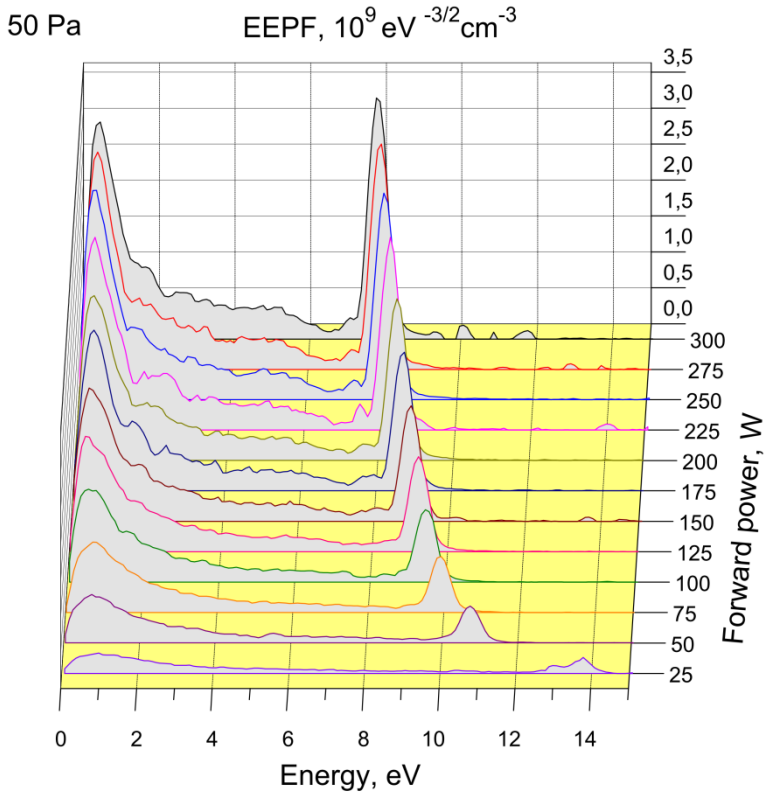
50 Pa
EEPF, 10^9 eV^-3/2 cm^-3
3,5
3,0
2,5
2,0
1,5
1,0
0,5
0,0
300
275
250
225
200
175
150
125
100
75
50
25
Forward power, W
0
2
4
6
8
10
12
14
Energy, eV

4.3. CCRF hydrogen discharge for plasma-chemical modification of thin PDMS films

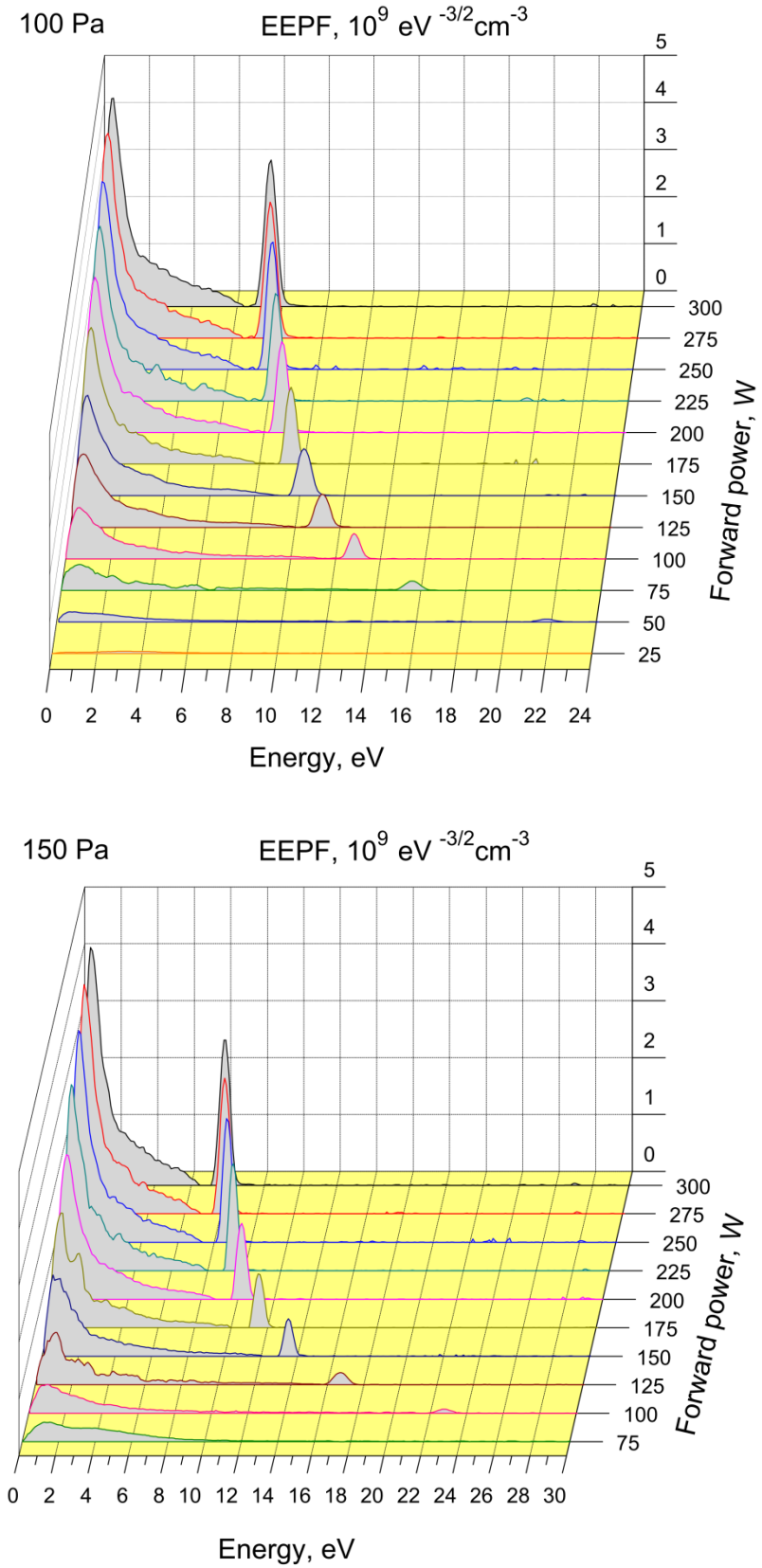

Figure 4.7. EEPFs for different forward powers and pressures.

The existence of the second peak was theoretically predicted by Francis F. Chen.[160] The distribution function of the non-thermal electrons depends on the acceleration mechanism. According the model it is assumed that the electrons are concentrated at the maximum of the RF field at which the electric field is directed properly to accelerate them. A runaway population of these electrons is rapidly accelerated well above their thermal speeds before a collision. These electrons will remain accelerated by the electric field until they fall out of phase or make a collision with a particle. It is supposed that collisional mechanism dominates. If their collision cross section changes like 1/v (v is their velocity), then the collision frequency will be constant. This means that the velocity gained by each electron will be the same regardless of its initial value. This will lead to the shift of Maxwellian EEDF. In another case, if the cross section is constant, the electrons will be averagely accelerated for a given distance. The energy gained by each electron will be the same, leading to the transformation of Maxwellian EEDF to another one with a second peak. According to the author's comments the real distribution will probably lie in between these two extreme cases. In the case of H_2 the mean free path close to its minimum is nearly constant vs. electron energy as it seen from Figure 4.6.

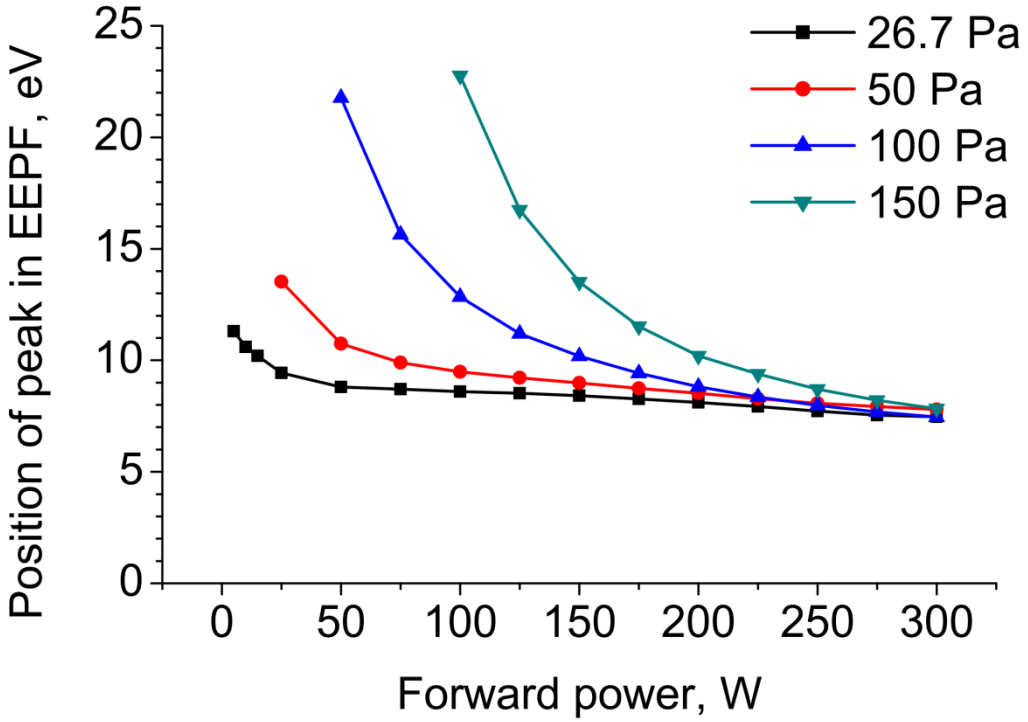

Figure 4.8. Position of the second peak in the EEPF for various pressures and powers.

4.3. CCRF hydrogen discharge for plasma-chemical modification of thin PDMS films

To calculate the concentration from EEPFs all electrons were separated in two groups: beam electrons belonging to the second peak and the rest – electrons of the main group. The electron concentration of the main group is presented in Figure 4.9. For all investigated pressures the electron concentration grows monotonically with increasing RF power.

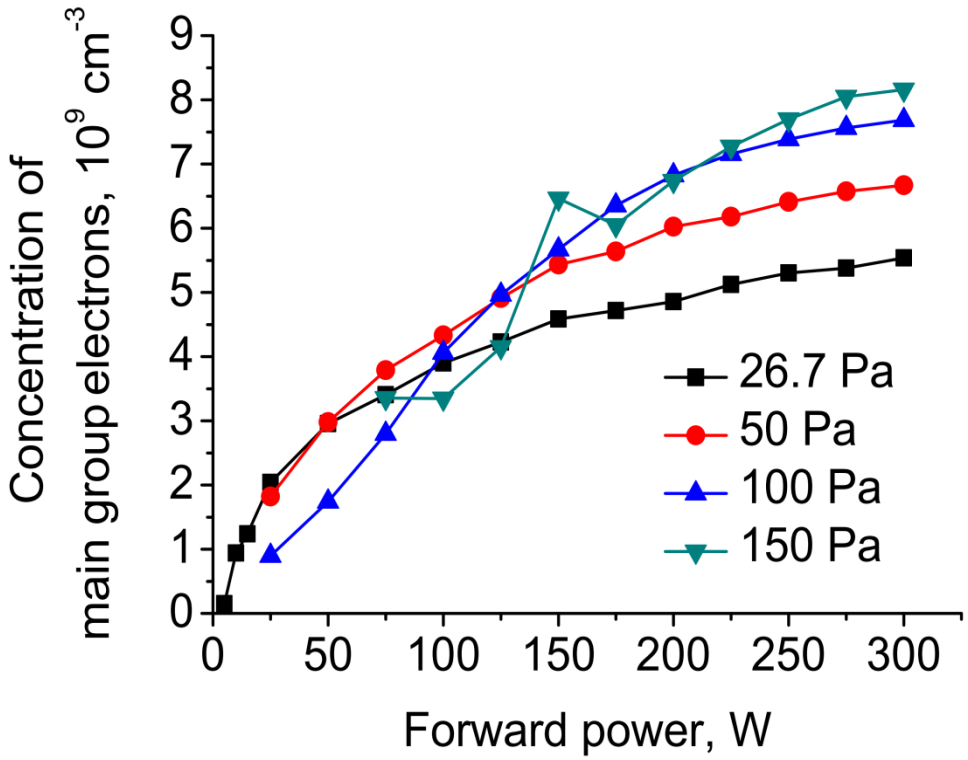

Figure 4.9. Electron concentrations of the main group for different pressures and forward powers.

Another behavior was found for the electron concentration of the second peak in the EEPF (Figure 4.10). With the exception of small RF powers, the beam electron concentration rises linearly with increasing RF power. The slopes of all graphs are very close to each other. There is only a slight difference between concentrations at 26.7 and 50 Pa, while for higher pressures the difference is stronger. With the decrease of the forward power the second peak of beam electrons disappears.

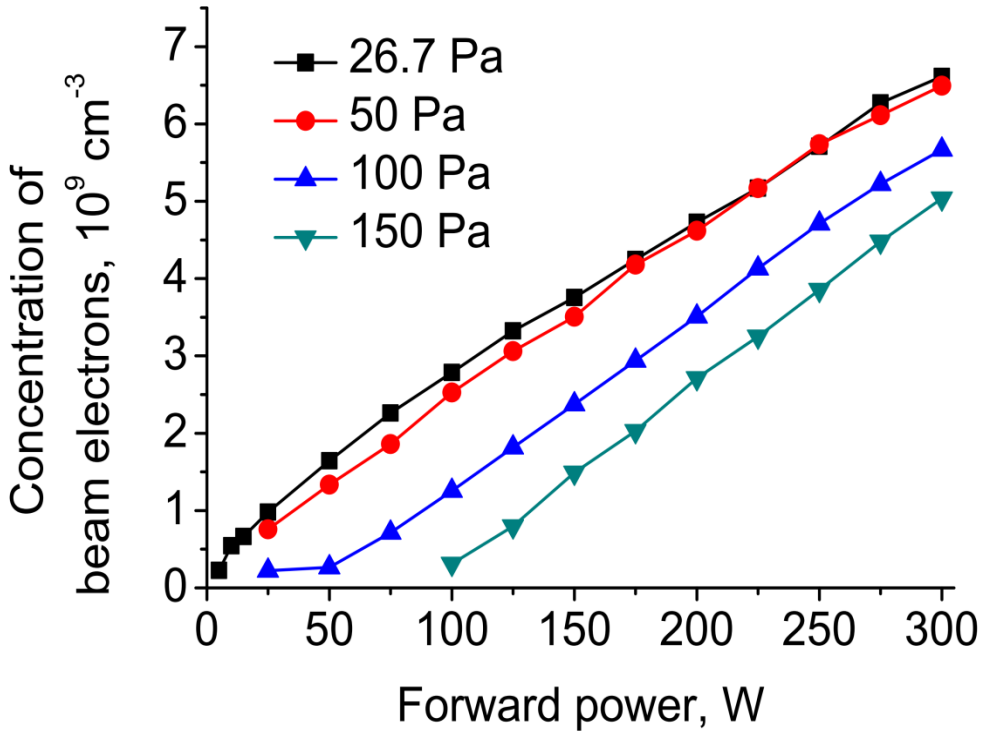

Figure 4.10. Beam electron concentration for different pressures and forward powers.

The effective electron temperature is presented in Figure 4.11. For both groups it decreases with increasing RF power. For beam electrons and low forward power a pressure increase leads to a rising effective temperature. With increasing forward power the temperature becomes less dependent and, finally, almost independent of the pressure. Such behavior of a convergence to an equal effective temperature was not observed for the main group electrons. It is interesting that the mean energy of hot electrons from the second peak can exceed the energy, necessary for the excitation of molecular levels. In this case such electrons should stimulate the emission of plasma. If their energy exceeds about 11.3 eV, they will be involved in the excitation of the $B^1\Sigma_u^+$ state. If the electron energy exceeds about 12.3 eV, than they reach the threshold to excite the $C^1\Pi_u$ state.[60,161]

4.3. CCRF hydrogen discharge for plasma-chemical modification of thin PDMS films

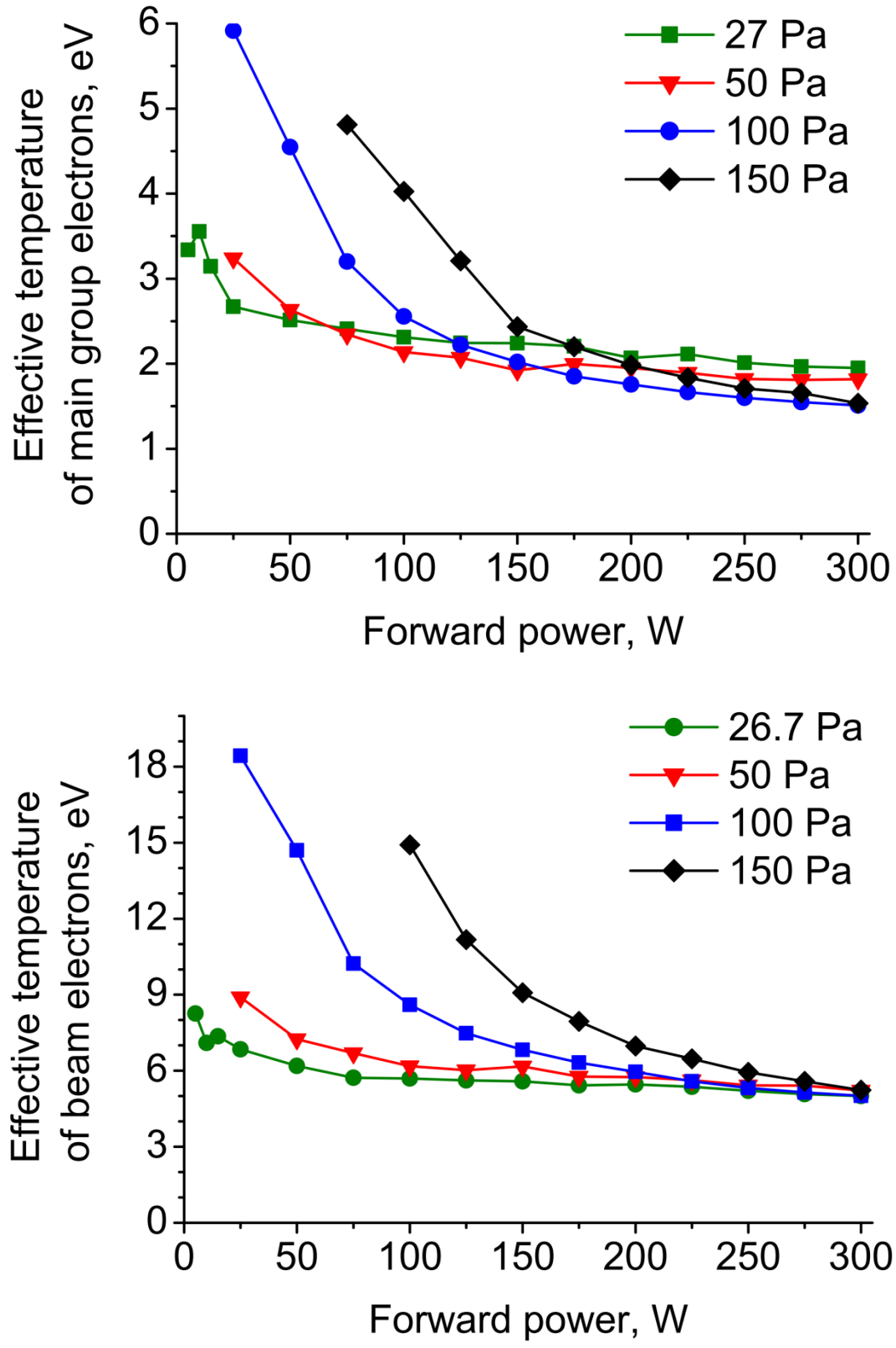

Figure 4.11. Effective temperature of the main group and beam electrons as functions of RF power and pressure.

The measured set of plasma and floating potentials for different pressures and forward powers is presented in Figure 4.12. Both potentials were measured relative to the ground potential. The difference of plasma and floating potentials defines the maximal kinetic energy of positive hydrogen ions accelerated in the sheath towards the film surface. From Figure 4.12 we see that for 26.7 and 50 Pa the difference $V_{pl} - V_{fl}$ depend weakly on the forward power and is about 8 – 11 V. For higher pressures it decreases from 25 – 27 V to ca. 8 V with the increase of forward power.

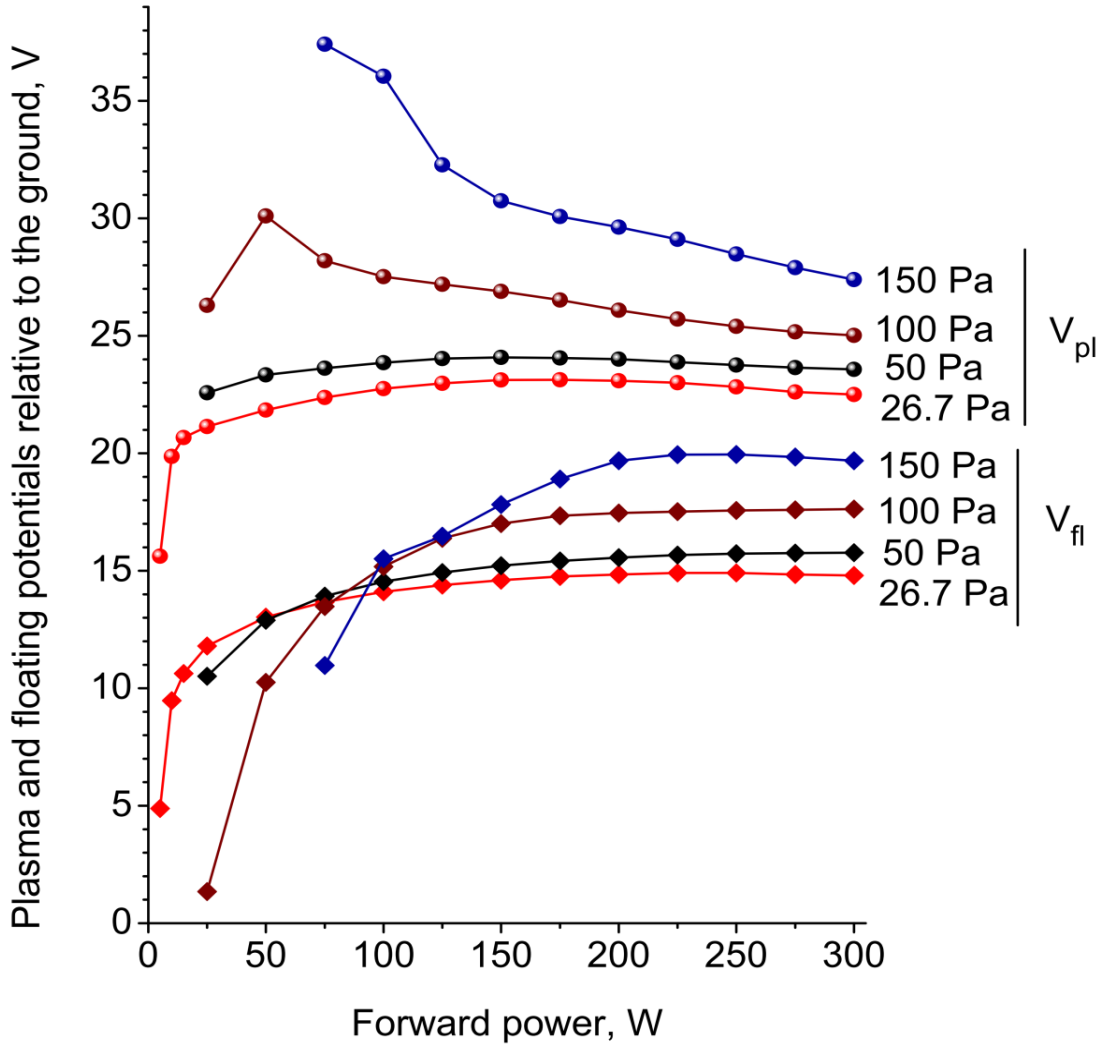

Figure 4.12. Plasma and floating potentials as functions of forward power and pressure.

4.3. CCRF hydrogen discharge for plasma-chemical modification of thin PDMS films

It is interesting to observe the dependence of the ratio $\frac{V_{pl} - V_{fl}}{T_e}$ vs. forward power and pressure. (Here, T_e is in eV). For electrons of the main group for forward powers above 100 W this ratio does not depend on the power, but depend only on the pressure: the higher the pressure is the higher the ratio is. For hot electrons from the second peak the ratio is also almost constant vs. forward power. But, unlike the case of main group electrons, it decreases weakly vs. pressure. If the ratio is known at one value of forward power, its constancy can be used to calculate the electron temperature T_e from the difference $V_{pl} - V_{fl}$ at other forward powers. In the case of second peak electrons it can be done as estimation for different pressures. The difference $V_{pl} - V_{fl}$ can be measured, for example, by the emissive probe or the floating emissive probe technique.[162]

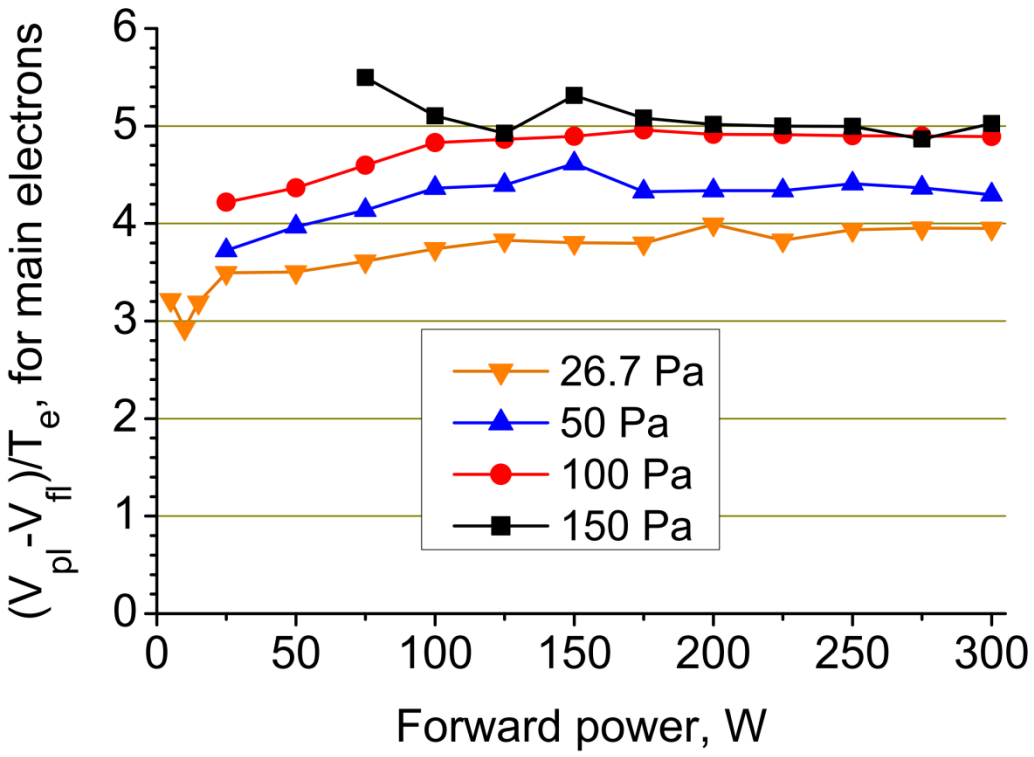

Figure 4.13. Ratio of plasma and floating potential difference, and the effective temperature for main group electrons. See the next page for continuation.

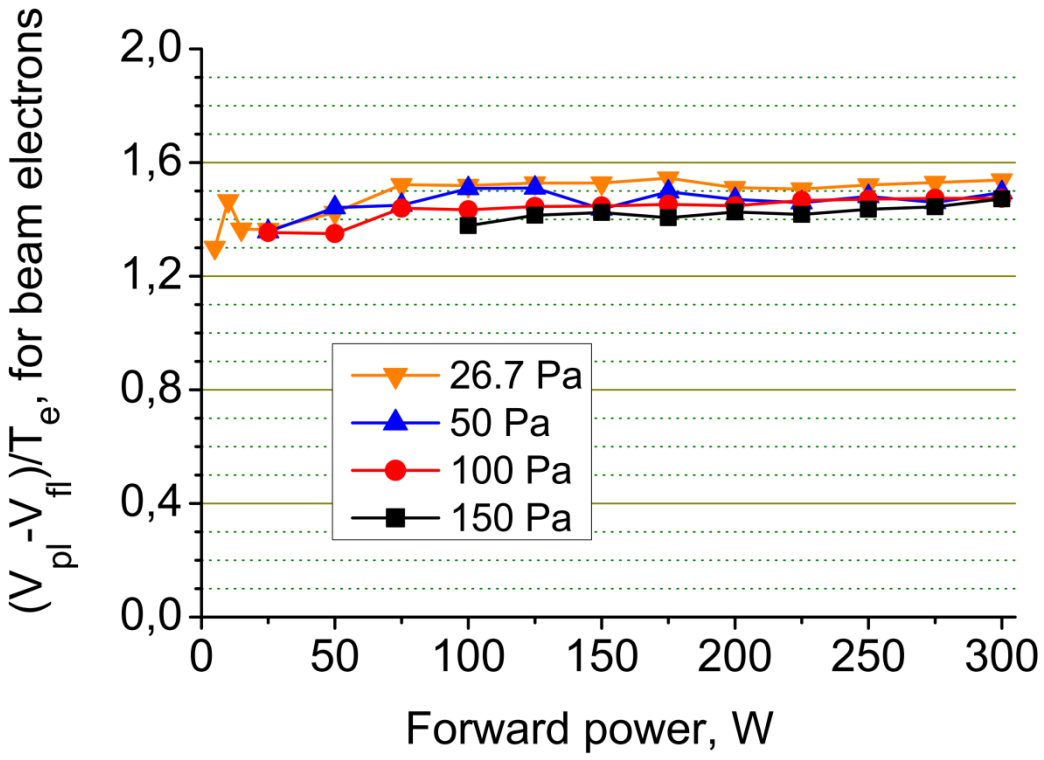

Figure 4.13. Ratio of plasma and floating potential difference, and the effective temperature for beam electrons.

4.3.2. VUV - visible radiation of the H_2 plasma

Going from results presented in the previous section the H_2 gas was selected for the plasma processing of PDMS films. The emission spectrum of CCRF discharge ignited in the setup, described in the 3rd chapter, was measured between 115 and 335 nm. The strongest radiation in this region comes from molecular Lyman bands emission which is marked in red in Figure 4.14. This emission appears due to transitions from vibration levels of the upper state $B^1\Sigma_u^+$ to vibration levels of the ground state $X^1\Sigma_g^+$ (Figure 4.15). It occupies the wavelength region from the cutoff at 115 nm to 170 nm with the most intensive peaks at 158 and 161 nm. The detailed scheme of vibronic transitions for $B^1\Sigma_u^+ \rightarrow X^1\Sigma_g^+$ is given in following works.[163,164] This emission is contributed also by cascade transitions from higher states.[163,165]. The primary cascade contribution appears due to the transition $E,F^1\Sigma_g^+ \rightarrow B^1\Sigma_u^+$ (Figure 4.15). Additionally, the molecular Werner bands marked in green in Figure 4.14 arise from rovibronic transitions $C^1\Pi_u \rightarrow X^1\Sigma_g^+$. These Werner bands are overlapped with the atomic Lyman alpha line at 121.6 nm and molecular Lyman bands.[166-168] The emission from Werner bands was quite weak at all processing conditions. Moreover, this emission is below 130 nm, where, as it will be shown in the next section, the depth of radiation penetration into PDMS films is small.

From the side of larger wavelengths the emission is represented by the transition $a^3\Sigma_g^+ \rightarrow b^3\Sigma_u^+$.[169] Although this emission is not very intensive, it is continuous, extending from approximately 160 nm, where it overlaps with $B^1\Sigma_u^+ \rightarrow X^1\Sigma_g^+$, to about 500 nm. In

Figure 4.15 the upper bound and the lower repulsive state for the transition $a^3\Sigma_g^+ \rightarrow b^3\Sigma_u^+$ are presented by blue potential curves. The spectrum features denoted "2nd order" in Figure 4.14 come from the 2nd diffraction order of the diffraction grid of the VUV monochromator. They are situated at doubled wavelengths of real plasma emission bands and Ly-α line.

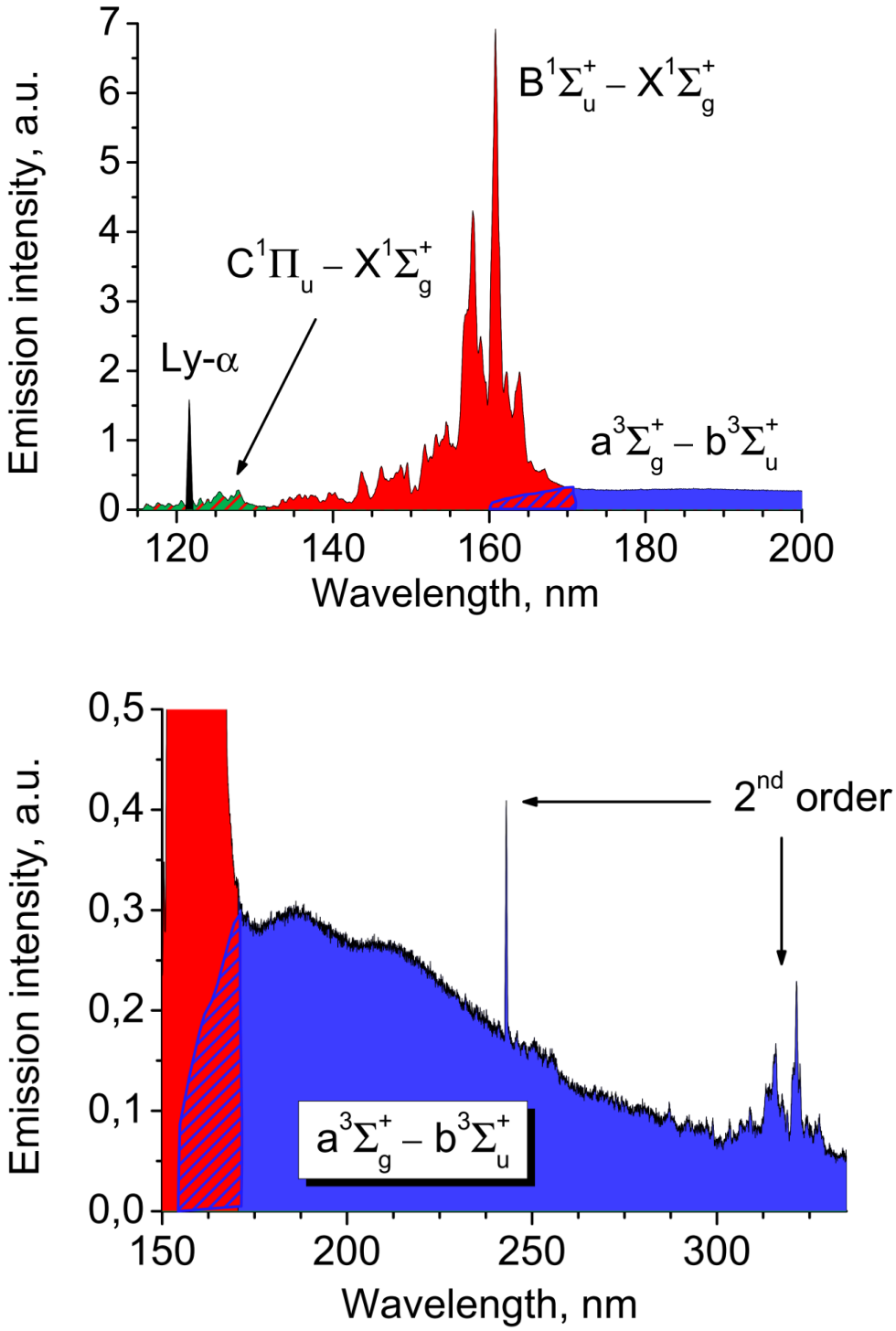

Figure 4.14. VUV and UV spectrum of a CCRF discharge in H_2 for the forward power of 250 W and the pressure of 150 Pa.

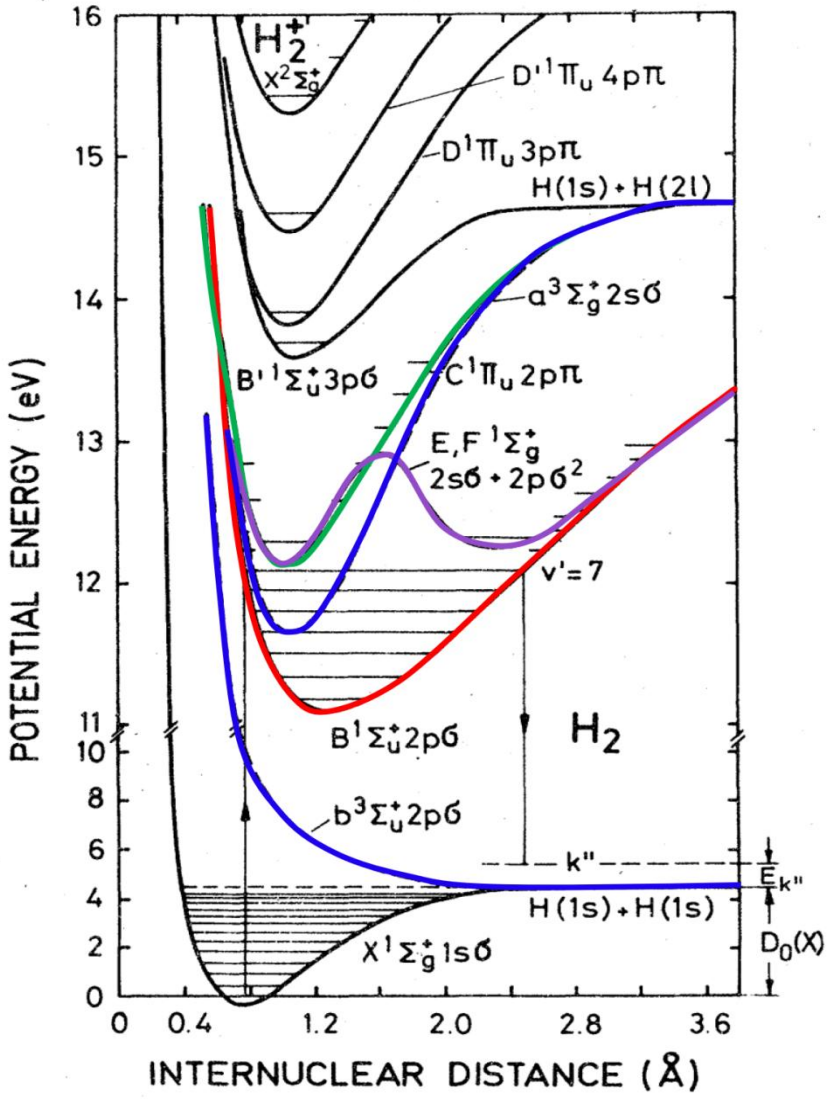

Figure 4.15. Potential curves and energy levels diagram of the hydrogen molecule. Adapted from [164].

The visible emission of H_2 plasma was investigated in the region 330 – 800 nm. Any traces of emission of other gases were not observed. The emission from OH radicals from H_2O, which always presents in the chamber as impurity, is below the cutoff. Additionally, in the case of PDMS plasma treatment any emission from CH_3, CH or C_2 radicals was not detected in the flow mode with 3 sccm and in the case of a closed chamber.

The emission shown in Figure 4.16 is typical for a hydrogen RF discharge. For example, a similar spectrum is presented in the PhD thesis of K. Dittmann.[170] The atomic radiation is represented by 4 observable lines of the Balmer series: H_α at 656.3 nm, H_β at 486.1 nm,

H_γ at 434.1 nm and H_δ at 410.2 nm. The molecular radiation is more complicated. The dissociation continuum $a^3\Sigma_g^+ \rightarrow b^3\Sigma_u^+$ starts in VUV region and continues up to about 500 nm. (The VUV/UV part of dissociation continuum was demonstrated previously in the Section 4.3.2). A part of other molecular bands is overlapped with the dissociation continuum and with each other. Their detailed identification can be found in following work.[171] The information about other molecular bands between 550 and 800 nm is presented elsewhere.[172,173]

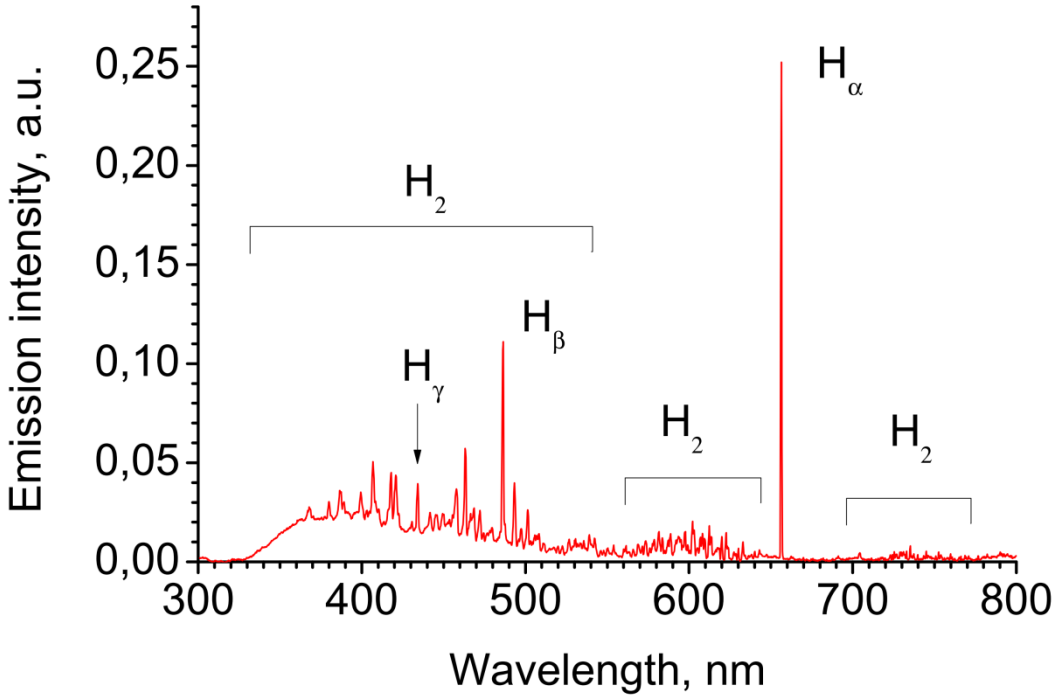

Figure 4.16. Typical emission spectrum of the CCRF hydrogen plasma (200 W, 150 Pa) in the range from 330 to 800 nm. The cutoff of glass window is at 330 nm.

4.3.3. Absorption coefficient of PDMS, TMS and SiO_x in VUV region

Absorption coefficient of PDMS and TMS

Now it is important to compare the VUV emission spectrum of the H_2 plasma with the absorption coefficient of PDMS to obtain additional information about the PDMS modification under the action of radiation. The data on the absorption coefficient can be found in various articles.[128,129,174,175] It is seen in Figure 4.17 that the onset of

absorption is close 190 nm. Next, the absorption coefficient rises up to the local maximum at 175 nm due to the absorption band and declines to the minimum at 163 nm. From approximately 160 nm (7.7 eV) the VUV radiation is so energetic that causes the ionization of PDMS increasing photoconductivity of PDMS.[176,177] (Additional data on the photoelectron emission for PDMS can be found in Koizumi et al.[178]) This contributes strongly to the increase of the absorption coefficient. Thus, the depth of radiation penetration decreases rapidly with the decrease of wavelength. For example, close to the emission maximum at 160 nm the transmittance is equal to 10% for PDMS film with thickness of 470 nm, with the thickness of 130 nm at the wavelength of 140 nm and with the thickness of only 30 nm at 120 nm.[128,175]

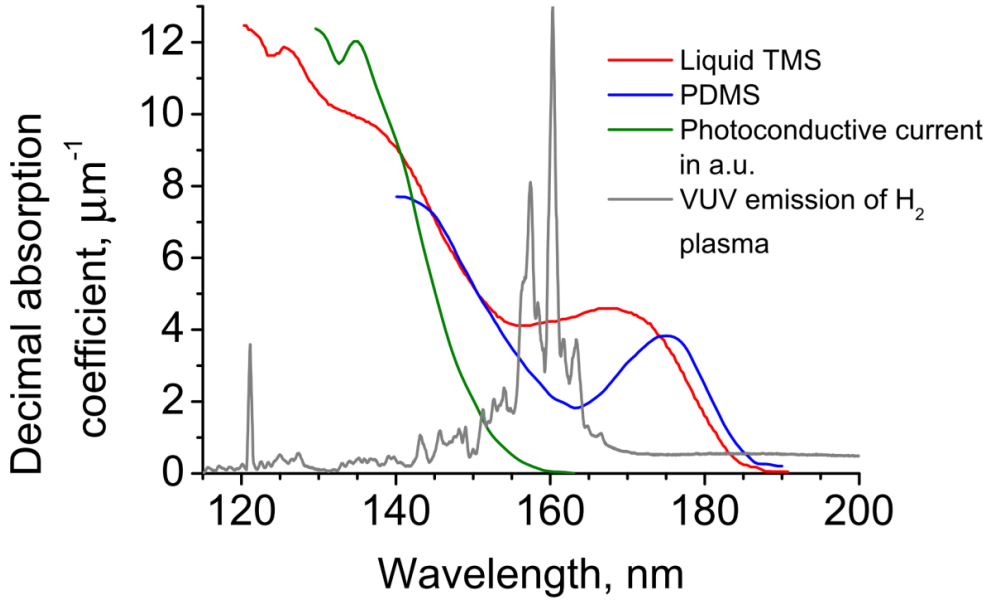

Figure 4.17. Decimal absorption coefficient according Cefalas et al. [128] (blue) and photoconductive current of PDMS (green) according Gulefucci et al. [176,177] (in a.u.), decimal absorption coefficient of liquid TMS according Saik et al.[179] and typical emission of H_2 plasma in this work vs. wavelength.

The information on the correlation of the absorption coefficient behavior and photophysical processes can be found in literature for tetramethylsilane (TMS), which consists of four methyl groups bonded to Si. Thus, the TMS molecule can be compared with PDMS because of the similar monomer unit. Accordingly, the absorption coefficient of PDMS and TMS behave similarly (see Figure 4.17)[179,180]. Saik et al.[179] on the basis of scientific works [180,181] (and others cited therein) stated that Rydberg transitions dominate the absorption spectrum of TMS in the region 125 – 190 nm. In particular, the band with the onset at 189 nm and the maximum at 166 nm is due to the allowed N → 4s Rydberg

transition, and the minimum at 155 nm appears due to the symmetry forbidden N → 4p Rydberg transition.[180]

The VUV photolysis of TMS was studied in different works.[182-184] It was found out that the photodecomposition goes in two channels: the photoexcitation into the Rydberg state is followed by simple Si-C bond breaking or by methane elimination. The cleavage of Si-C bond, which has the least dissociation energy among all in PDMS, and the following release of CH_3 radicals or CH_4 molecules are in agreement with the results observed by FTIR in this work for PDMS. It was measured clear degradation of vibration bands indicating the destruction and removal process of CH_3 and Si-CH_3 groups. Additionally, in Lee and Graves the influence of VUV radiation on low-k SiOCH films was studied.[135] It was shown that the VUV photons cause the demethylation of material and the formation of SiO_x overlayer. Here, the release of CH_3 radicals was detected by mass spectrometry. In other works stable products such as CH_4, H_2 and C_2H_6, composed of two CH_3 radicals, were also observed. [129,185]

Absorption coefficient of SiO_x

During plasma modification the top layer of the PDMS film experiences the most intensive influence of VUV radiation. As a result it is transformed into SiO_x layer, where all CH_3 groups are destroyed and removed. This layer can have the absorption coefficient more or less than that of PDMS and, therefore, to hinder or to ease the penetration of VUV radiation to deeper layers of the film. The data on optical properties of SiO_x in VUV region is found in following works [186,187]. In Figure 4.18 the natural absorption coefficient of SiO_x for different x is compared with that of PDMS. In the region below about 180 nm the absorption coefficient of PDMS is between the absorption coefficients of $SiO_{1.5}$ and $SiO_{1.75}$. The original ratio Si/O in PDMS is equal to 1. However, during transformation of the top region into SiO_x this ratio can change. Spectroscopic investigations of the H_2 discharge showed no traces of air inside the chamber (no emission from N_2 and O_2 and their derivatives). But an observed weak emission from OH radical with a maximum at 306 nm revealed the presence of H_2O vapor in the discharge, which is the source of additional oxygen. The thickness of the SiO_x layer in experiments was between 10 and 60 nm. This layer, whole or in part, can be influenced by the presence of oxygen, and the stoichiometric index x can be increased. In this work the index x was not measured, and the question about the absorption of VUV radiation by the SiO_x top layer remains open.

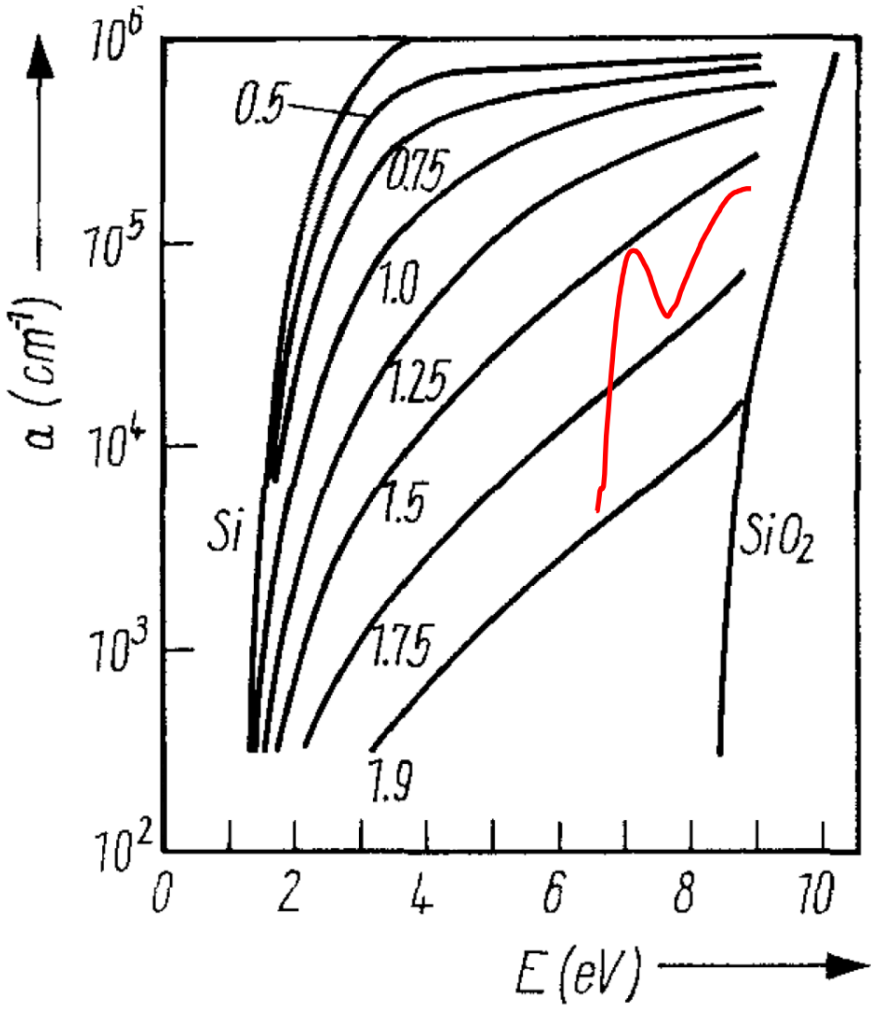

Figure 4.18. Natural absorption coefficient of SiO_x for different x, and of PDMS (red curve) [128]. Adapted from [187].

4.3.4. Integrated VUV spectrum of the CCRF hydrogen plasma.

To optimize the intensity of the VUV radiation of H_2 CCRF plasma the pressure and forward power were varied. The spectrum was registered by the VUV monochromator from the side face of the plasma chamber as shown in Figure 3.1. The entrance slit of monochromator with the height of 5 mm and the width of 500 μm was located at the height of 1 cm above the surface of the powered electrode and at the discharge axis. This position was chosen to acquire the most intensive radiation in the discharge near the sheath edge at the powered electrode.[188]

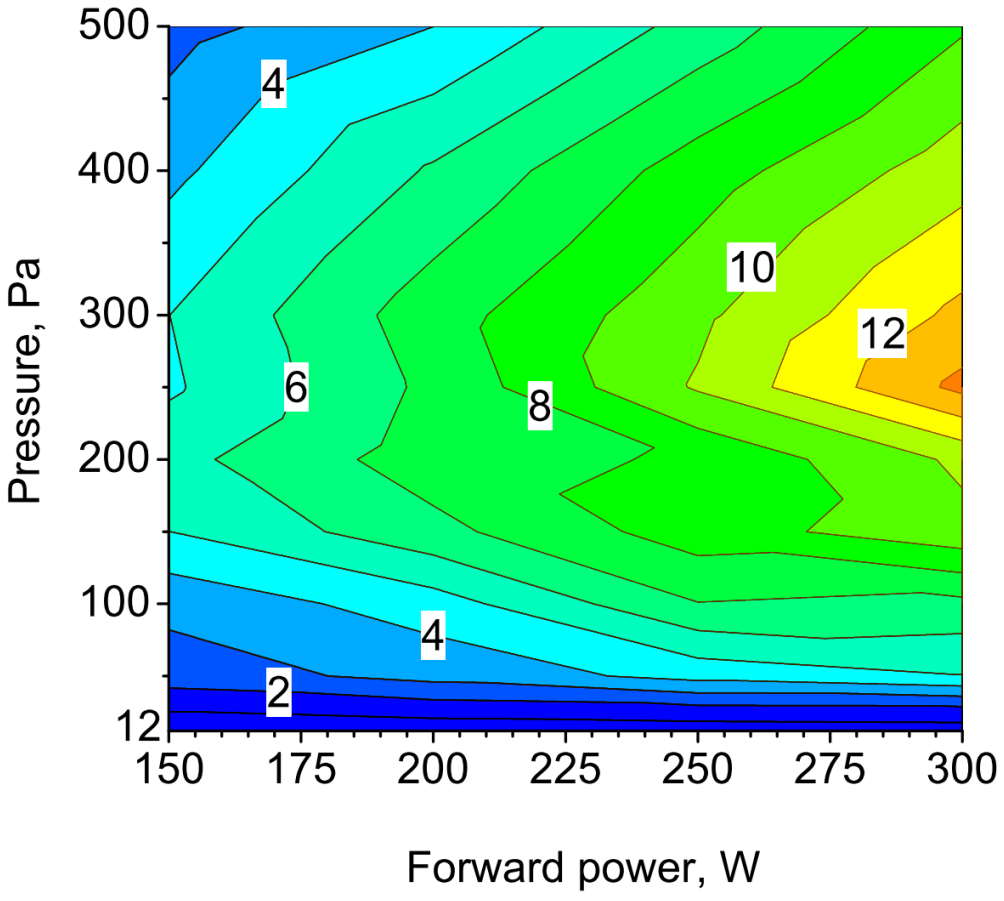

Figure 4.19. Integrated intensity of VUV radiation (115-200 nm) in a.u. vs. forward power and pressure. The intensity was normalized for comparison with the Figure 4.23.

The intensity integrated over the VUV region is presented in Figure 4.19. As it was already demonstrated in the section 4.3.2 the vast contribution to the integral intensity comes from the Lyman bands. For the case presented in Figure 4.14 the Lyman band contributes ca. 73% of the total integral value in the range $115-200$ nm, dissociation continuum $a^3\Sigma_g^+ \rightarrow b^3\Sigma_u^+$ – ca. 22%, the Werner bands and the Ly-α line – 3.5 and 1.5 %, respectively. The total integrated intensity rises monotonically with the increase of the forward power for all pressures. At rising pressure from 12 to 500 Pa the intensity shows a flat maximum. The position of this maximum gradually drifts from 200 to 250 Pa as the forward power is increased from 150 to 300 W. The absolute maximum of intensity for the given range of forward power and pressure was found at 300 Pa and 300 W.

4.3.5. Absolute VUV intensity of the H_2 plasma radiation.

The absolute VUV irradiance (mW/cm^2) was measured by a power meter applied from the top of the plasma chamber with the detector on the discharge axis (see Figure 4.20). The photocathode of detector is made of diamond semiconductor with the bandgap of 5.5 eV and, therefore, it is blind to the UV and visible radiation.

The power of radiation coming from plasma is decreased due to the absorption of the MgF_2 window and the oxygen in the gap (90 ± 20 μm) between the window and the detector head. The gap appears due to a constructional feature of the detector. The transmittance of window with the thickness of 4 mm is taken from the manufacturer Korth Kristalle, the transmittance of oxygen – from [69,189]. This data is in a good agreement with that from other sources [68,70,71]. Additionally, the detector has variable spectral response and it is calibrated for the wavelength of 146 nm. (see Figure 4.21).

All these factors taken into account in an appropriate manner give the formula to recalculate the real irradiance from measured one:

$$I = I_m \int_{\lambda_1}^{\lambda_2} E_\lambda \, d\lambda \Big/ \int_{\lambda_1}^{\lambda_2} T_w T_g \frac{S}{S_{146}} E_\lambda \, d\lambda \qquad (4.6)$$

I_m is the measured intensity, E_λ is the spectral irradiance in a.u. (spectrum measured by VUV monochromator), T_w – transmittance of MgF_2 window, T_g – transmittance of air gap, S – relative spectral response, S_{146} = 0.934 – value of relative spectral response at 146 nm.

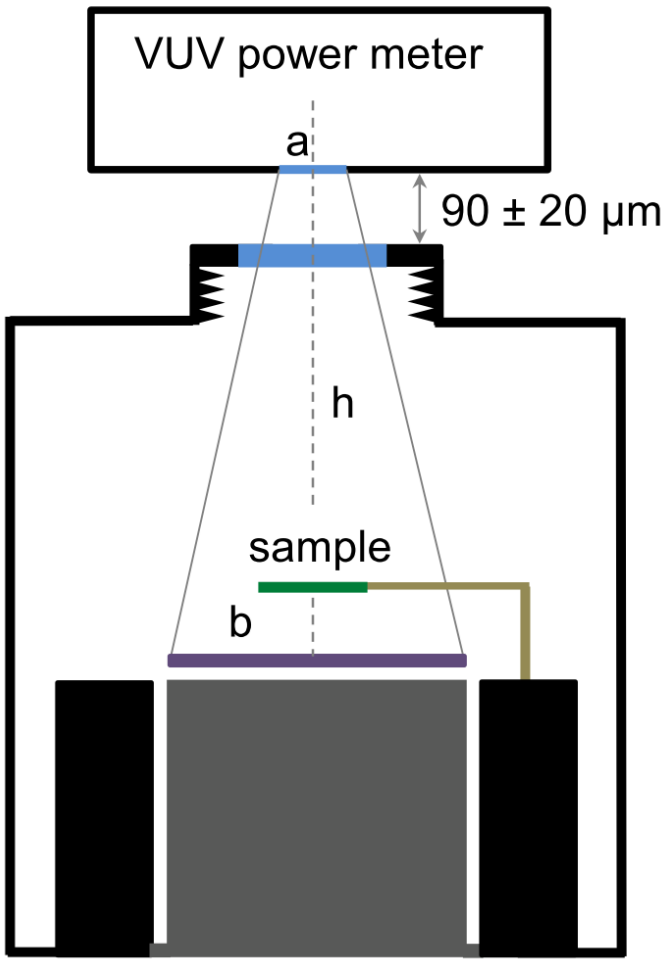

Figure 4.20. Schematic of the plasma chamber and the applied sensor head of the VUV power meter. The sample with PDMS film was absent during the measurement of VUV irradiance.

4.3. CCRF hydrogen discharge for plasma-chemical modification of thin PDMS films

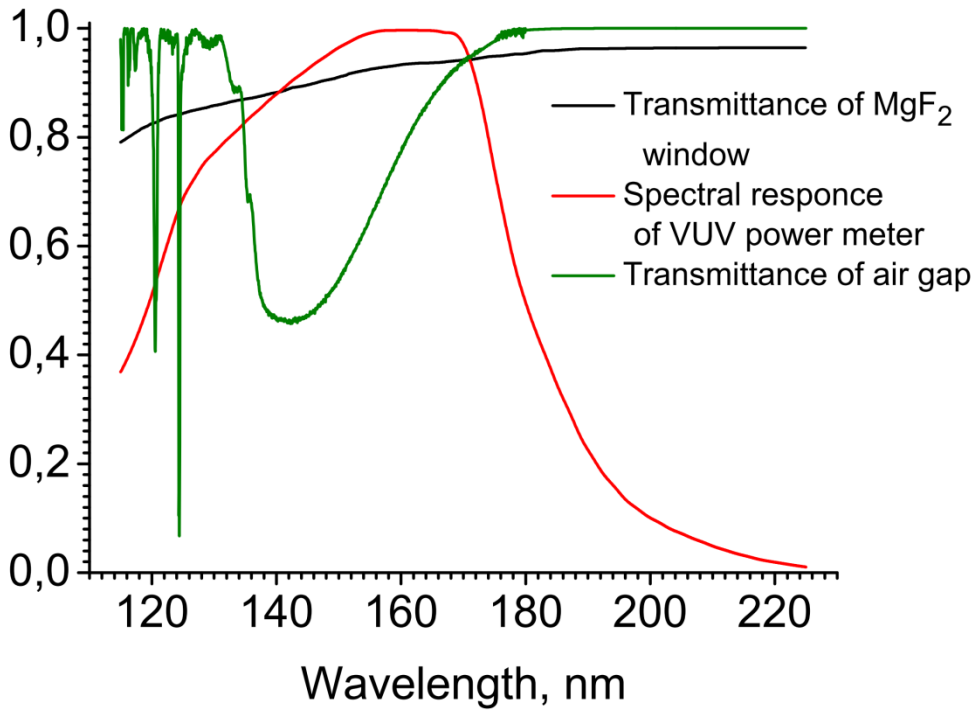

Figure 4.21. Transmittance of the MgF_2 window with the thickness of 4 mm, transmittance of oxygen in the air gap with the thickness of 90 μm and relative spectral response of the power meter. Data for absorption of oxygen is taken from Lu et al. and Ackerman et al.[69,189]

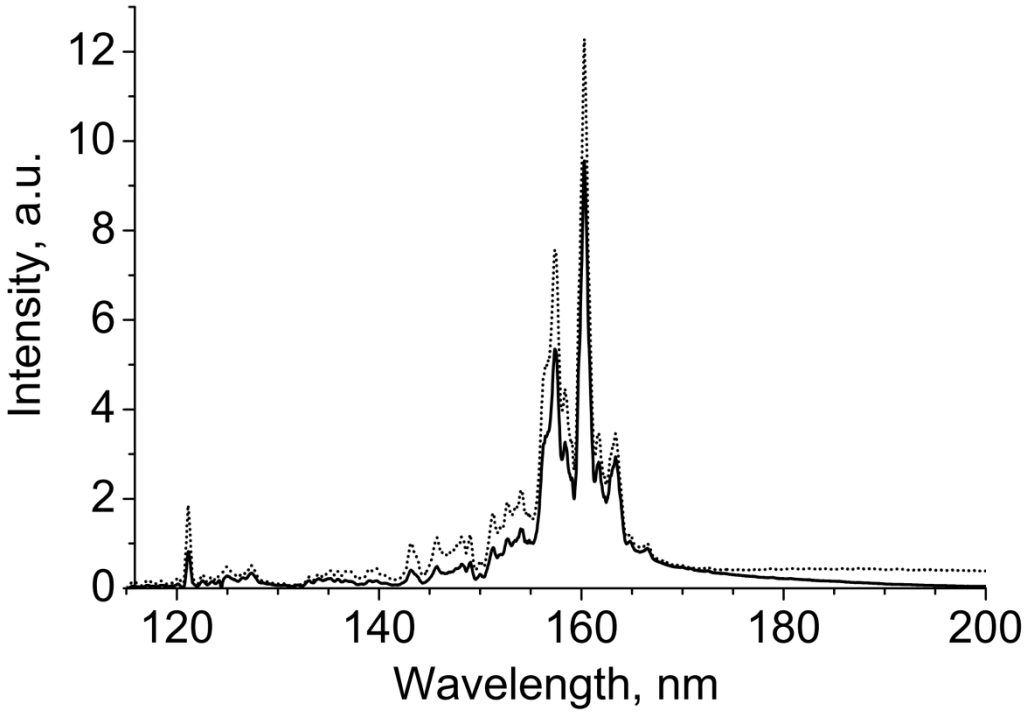

Figure 4.22. The emission spectrum of the CCRF hydrogen discharge at 300 W and 250 Pa (dotted line) and the same spectrum distorted due to the absorption in the optical system and the influence of the spectral response.

Figure 4.22 compares both integrals for example with the RF power of 300 W and the pressure of 250 Pa. Their ratio is equal to 1.54. From the formula it is seen that this ratio depends on the spectral irradiance. But as the spectral distribution for different RF powers and pressures are similar, the ratio remains almost constant.

The detector was applied from the top of the plasma chamber and the PDMS samples were treated inside at the height of 2 cm above the surface of the powered electrode. The difference in positions means the difference in the intensity of radiation coming from plasma to the surface of film and to the detector. To recalculate the intensity a simple model is proposed. The VUV radiation comes to the photocathode surface of circular the detector with the radius a = 0.33 cm from the circular disc located slightly above the powered electrode. The distance between the detector and the emitting disc is 11.8 cm. The radius of this disc is equal to that of power electrode (b = 5.4 cm). It emits the VUV light like a Lambertian radiator. Lambertian radiator - is an emitter, which luminance is constant and does not depend on the direction, i. e. it is independent of the position of a point on the surface and the angle of observation. In this case the luminous flux of photon Φ trough the surface of detector is expressed as follows: [190]

$$\Phi = \frac{L}{2}\pi^2\left[h^2 + a^2 + b^2 - \sqrt{(h^2 + a^2 + b^2)^2 - 4a^2b^2}\right] \qquad (4.7)$$

L is a luminance of the emitting disc.

To compare irradiancies one can select a circular area in the center of the sample of the same area as the area of the detector photocathode. Then, the ratio of geometrical factors in brackets for different distances can be used to calculate the irradiance of circular area on the sample from measured one. Taking into account all factors: the absorption in the optical system, the spectral response, the position of the detector head and the sample, we obtain the factor 8.4. The resulting VUV irradiance is presented in Figure 4.23. Its dependence vs. pressure and forward power is similar with the previously presented dependence of the integrated intensity (see Figure 4.19). The strongest irradiance of a sample appears at 300 W and 200 − 250 Pa and amounts to about 13 mW/cm^2. This value exceeds more than 1000 times the irradiance from the Sun in the range 115 − 200 nm and beyond the atmosphere.[191]

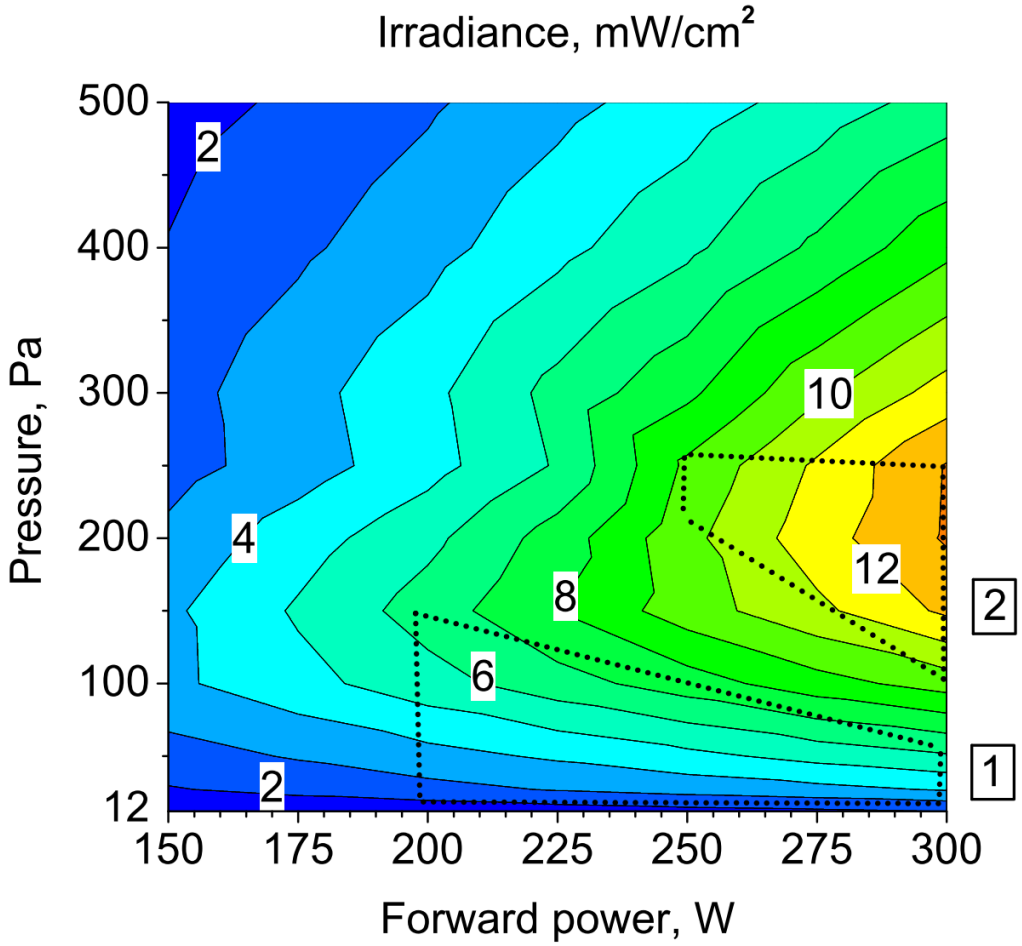

Figure 4.23. VUV irradiance (mW/cm²) vs. forward power and discharge pressure. On the right [1] denotes the region of pressures and powers at which modified films remain undamaged, [2] – become damaged.

In Figure 4.24 and Figure 4.25 the same data is presented as irradiance vs. forward power and as irradiance vs. pressure. For pressures in the range between 12 and 150 Pa a linear increase of the irradiance with rising RF power is observed. At that, the higher is the pressure, the faster increases the irradiance. For another range from 200 to 500 Pa the linearity is not observed anymore and the irradiance increases slightly faster than linearly. The dependence of irradiance vs. pressure is non-monotonic. As the forward power increases the main maximum gradually shifts from 100 to 250 Pa. Another ill-defined peak at 300 Pa exists in the power range from 150 to 225 W, in the range 250 – 300 W it is absent.

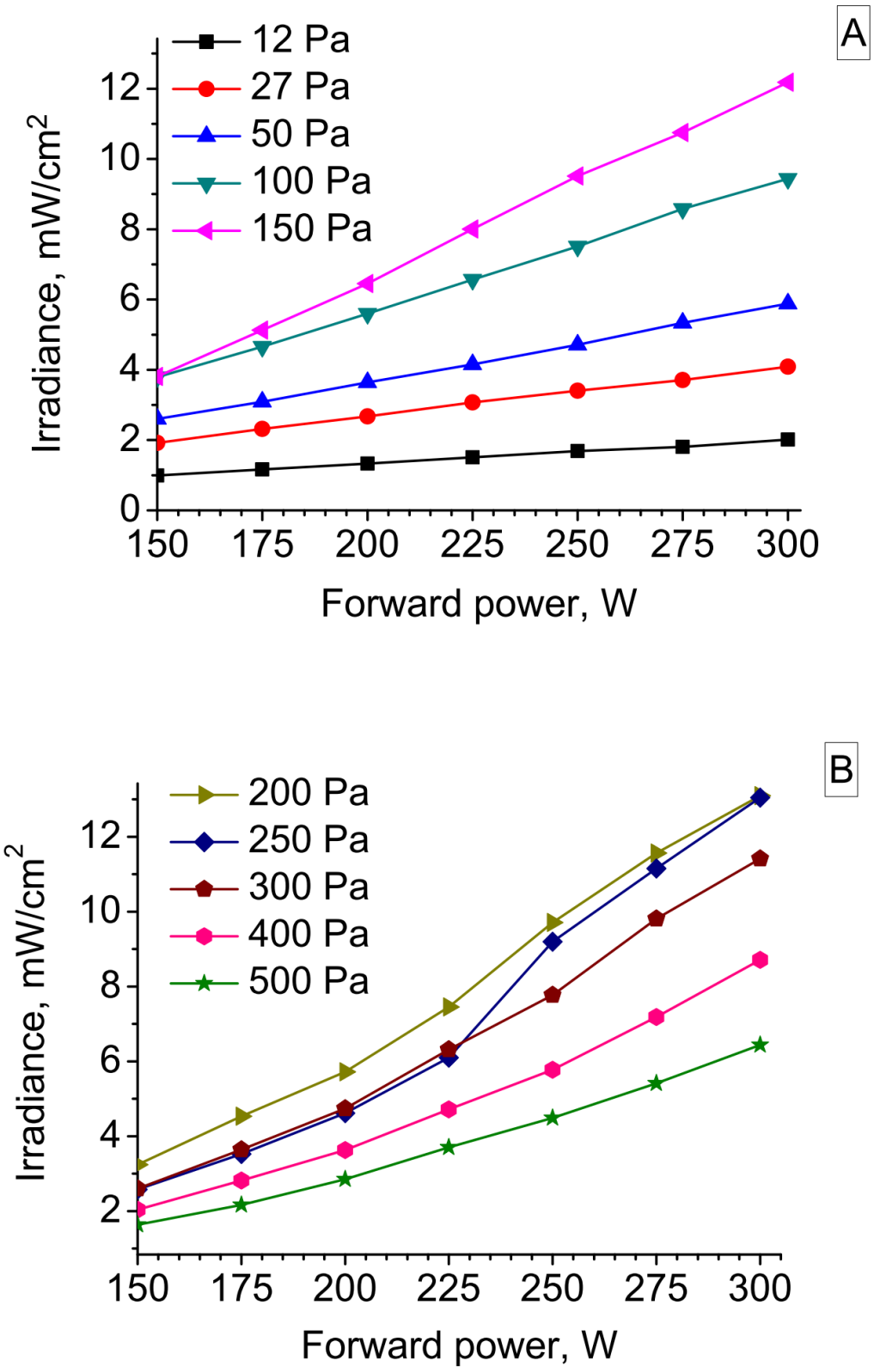

Figure 4.24. VUV irradiance (mW/cm²) vs. forward power at different hydrogen pressure, (A) 12 – 150 Pa and (B) 200 – 500 Pa.

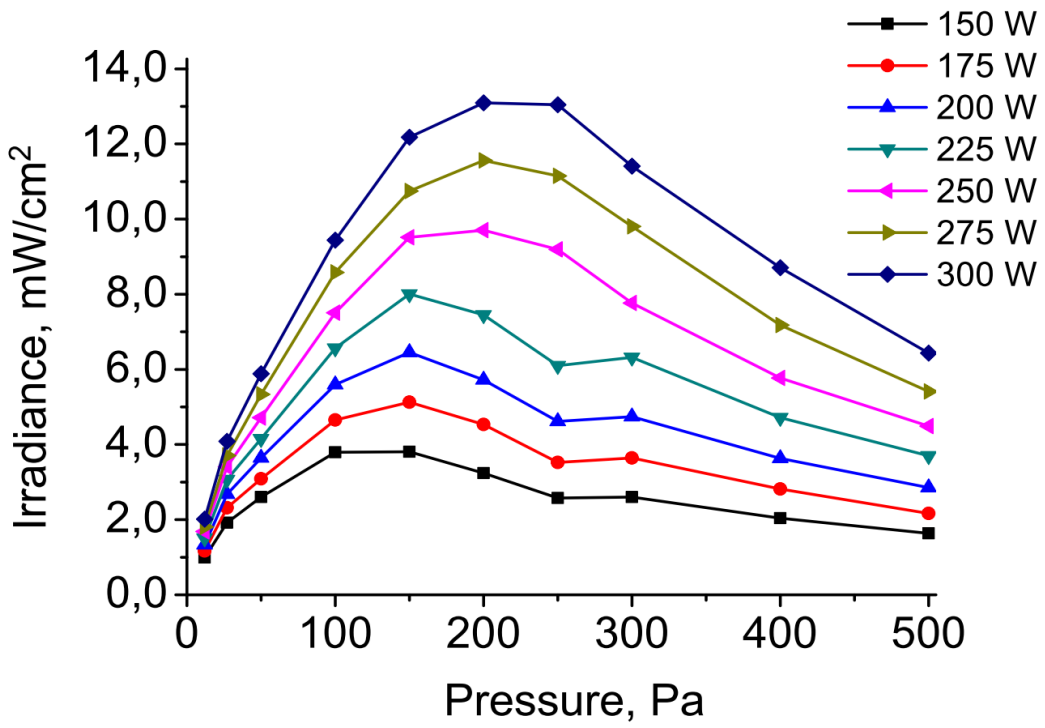

Figure 4.25. VUV irradiance (mW/cm^2) vs. pressure for different RF forward power (150 – 300 W).

When the pressure is decreased the intensity of VUV plasma emission quickly drops down, and the film treatment becomes disadvantageous since the treatment time should be strongly increased to irradiate a film with a sufficient dose. In conclusion, it should be added that the sample with a film located in the chamber will disturb the plasma. Therefore, the plasma emission intensity in experiments with and without a sample treatment can be different. To investigate it, instead of a sample a MgF_2 dummy, transparent for VUV (made of MgF_2), was installed. At low pressures the sheath edge at the powered electrode with intensive emission extends to the position of dummy and is influenced by it. As the result for pressure of 25 Pa the irradiance amounts in only 70 % from the initial value. With an increase of pressure the difference reduces and disappears completely above 50 Pa.

4.3.6. Damage of thin films at high VUV intensities

In Figure 4.23 two regions are marked by dotted lines. There, the influence of VUV radiation on the quality of film surface was studied. It was found that the intensive radiation may cause the damage of thin films (Figure 4.26 (a)).

The dynamics of PDMS damage by hydrogen plasma radiation can be divided in several periods depending on the treatment time at fixed RF power and pressure. After about 0.5 - 1 min of treatment time bubbles are produced with a diameter below 2 mm. Between 1 min and 5 min their diameter continuously increases up to 2 - 4 mm, and new bubbles appear. After approximately 3 - 5 min the bubbles start to explode intensively and damage the film. Then, the bubble production decelerates and the damage process stops completely after about 5 -10 min, a strongly eroded surface remains.

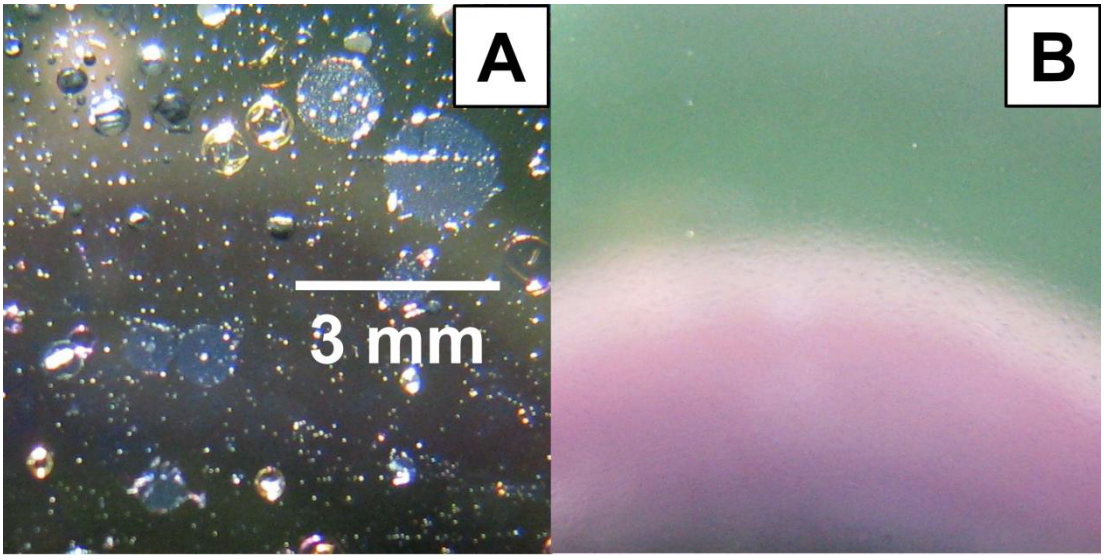

Figure 4.26. Photograph of films modified during 10 minutes at different pressure and forward power: (A) 250 Pa , 300 W, (B) 150 Pa, 200 W. The violet bright field in (B) is the reflection of the camera objective.

As it was already written the treatment of PDMS films causes the cleavage of the Si-C bond and the release of CH_3, H and other radicals. The association reaction of radicals leads to the formation of stable products: H_2, CH_4 and C_2H_6.[129,185]

As it was shown in our paper the top layer of PDMS is completely modified into SiO_x material.[192] According Chatham the SiO_x layer acts like a barrier for oxygen.[193] In our case this top layer may prevent the

release of the above mentioned gaseous products and leads to their accumulation with further film damage.

The simplest way to avoid damages is to perform the modification at optimized radiation intensities. Bubbles do not appear for lower intensities, even if the treatment time is increased and the irradiation dose is comparable with that for higher intensities and shorter time. It means that gas products are released due to the diffusion through plasma-modified film or/and pores with a rate equal or less a production rate.

4.4. Characterization of plasma-modified PDMS films

4.4.1. Characterization of thin plasma-modifed PDMS film surface by optical and SEM microscopy

In Section 4.3.6, Figure 4.26 B the image of undamaged plasma modified film was presented. Here, in addition to it, the scanning electron microscopy (SEM)[194] image demonstrates a successfully modified PDMS film. For SEM imaging technique the film surface should be conductive to prevent the accumulation of negative charge. For this purpose the H_2 plasma-modified film was covered by a golden layer with the thickness of about 10 nm by means of magnetron sputtering technique. Because of its small thickness the golden layer can mask only small defects like open pores and cracks. Grains, which are especially prominent in Figure 4.27 B, are the part of the golden layer, but not of modified PDMS film. From Figure 4.27 A and B it is seen that the surface is smooth, flat and without strong defects. The initial thickness of this film measured by spectroscopic ellipsometry (SE) was 185 nm. During the H_2 plasma modification the PDMS undergoes cross-linking and also losses methyl groups. This results in a shrinking of the film. The reduced film thickness was measured by SE and compared with that determined by SEM. Both results are in the good agreement: 135 and 140 nm. (The value 140 nm obtained by SEM is derived as 150 – 10 nm of golden layer.) The effect of film shrinking for different process parameters like treatment time, discharge pressure and forward power will be described in the next chapter.

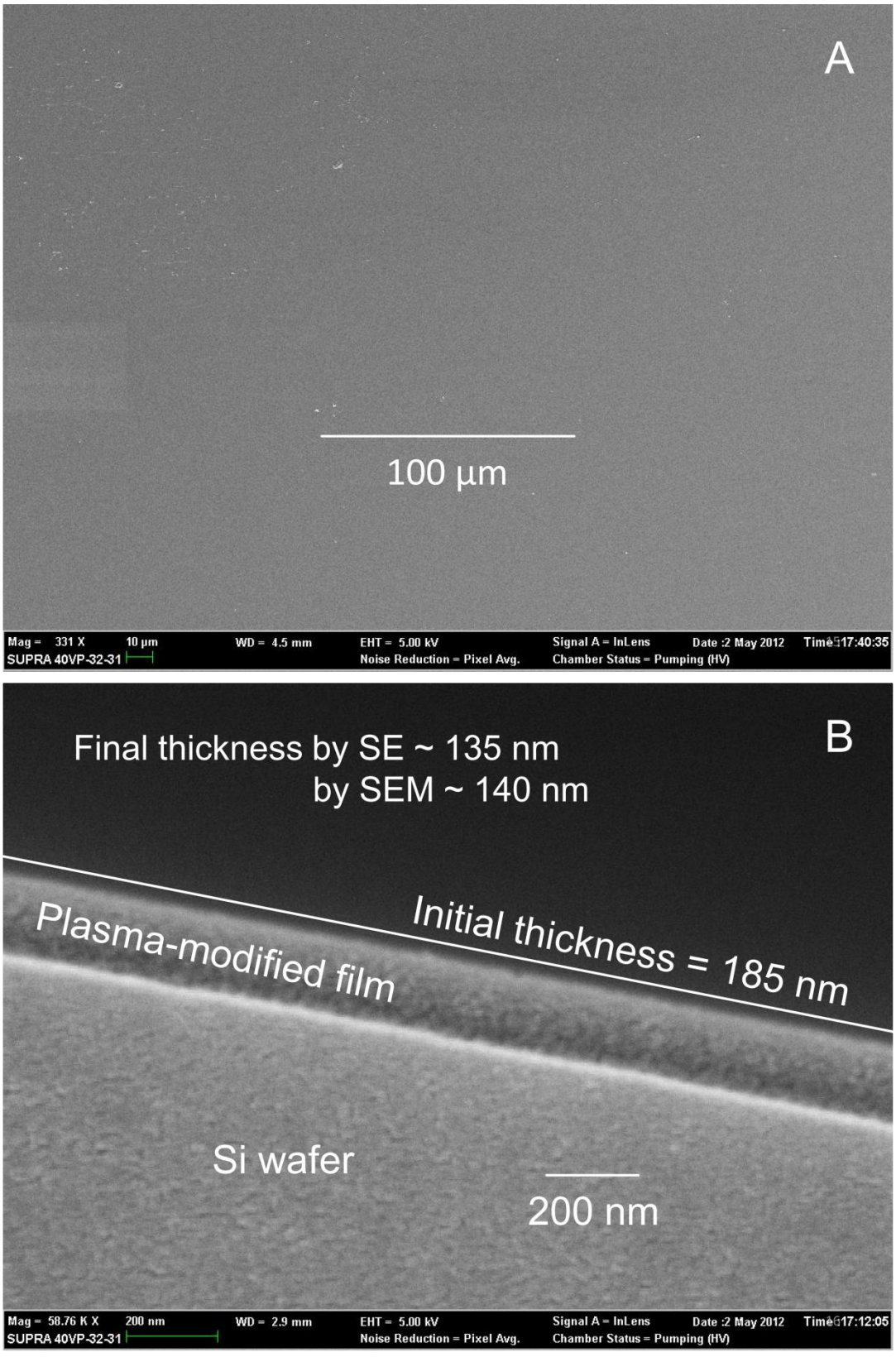

Figure 4.27. SEM image of the top (A) and side (B) view of a plasma modified PDMS film with the initial thickness of 185 nm. In (A) the light rectangular on the left side is a burnout arisen from an intensive electron beam used in SEM.

Even if the film silicone oil is filtered, the ideal case presented in Figure 4.27 does not occur always. Figure 4.28 demonstrates the H_2 plasma-modified PDMS film with a wavelike structure, which contains a dust particle in the centre. This particle stuck to the liquid PDMS film before treatment. Similar structures of plasma-modified PDMS films were observed in other works.[22,195-200] Figure 4.29 demonstrates images reprinted from them. In the case "A" we see the unordered wavelike structure.[22] Crosslinked PDMS film containing the stabilizer Tinuvin® 770 was exposed to 2.2 h corona discharge in dry air at atmospheric pressure. In the case "B" the silicone based paint CV-1146 was heated in the effusion cell at the temperature of 125 °C for 12 to 24 h.[198] Outgassing product of this paint was identified by FTIR spectroscopy as PDMS. Afterwards, collected PDMS was treated by VUV radiation of deuterium lamp or RF discharge in Ar. In the case "C" and "D" the structures were prepared in a three-step procedure: heating of PDMS to expand it, its exposition in oxygen plasma to produce a thin surface layer of silica-like material and, finally, the cooling.[196]

The procedure started with heating the PDMS in an oven at a constant temperature between 50 and 250°C during no less than 45 min. Then PDMS was taken from the oven and immediately loaded into a Anatech SP100 plasma cleaner and oxidized in RF plasma in oxygen at a pressure of at a pressure of 0.04 – 0.13 Torr. Due to the dissipation of energy from plasma the inner tube of the cleaner had a temperature of ca. 80°C maintaining the PDMS slab warm. After the oxidation, the PDMS was extracted from the cleaner and allowed to cool down to ambient temperature. During the cooling the waves were formed on the surface. If initial PDMS was flat and without bas-reliefs, the surface was covered by waves locally ordered, but globally disordered (Figure 4.29 C). (In our work similar disordered structures were also observed in the absence of dust particles in vicinity.) When the surface was patterned with bas-relief, the wavelike structure became ordered like in Figure 4.29 D. This structure is like that presented in Figure 4.28, where the dust particle plays the role of bas-relief. In the above-described and in our work the top surface of PDMS is modified by plasma in SiO_x layer with x between 1 and 2. The volumetric thermal expansion coefficient of SiO_2 material is equal to about $1.5 \cdot 10^{-6}$ °C^{-1}, for SiO_x films it is $(0.6 - 10) \cdot 10^{-6}$ °C^{-1},[201-203] and for PDMS at temperatures in the range between 20 and 200 °C it is $(0.9 - 1) \cdot 10^{-3}$ °C^{-1}.[102,204] (In some mentioned sources the data is given in the form of linear thermal expansion coefficient. For isotropic materials and for small expansions it is approximately 1/3 of the volumetric one.) The difference is great; it means that during cooling the

bulk volume will decrease much stronger and produce the compressive stress in the SiO_x top layer. This stress buckles the plasma-modified SiO_x layer leading to formation of observed wavelike patterns.

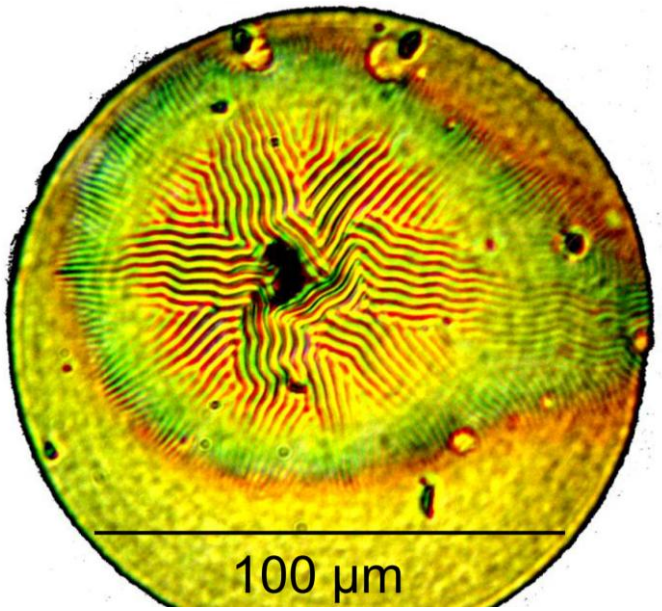

Figure 4.28. Optical image of a wavelike surface topography of the H_2 plasma-modified thin film with the initial thickness of ca. 180 nm. Here, in the centre of the structure is a dust particle.

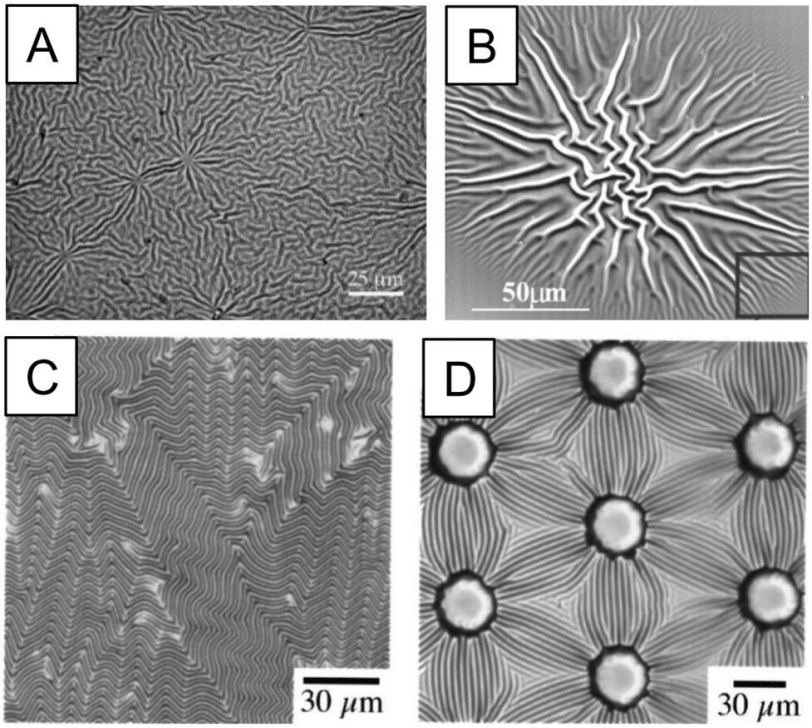

Figure 4.29. Wavelike structures of plasma modified films reprinted from different articles: A from [22] and B from [198], C and D are from [196].

In some series of experiments in this work the samples were placed on the surface of the powered electrode. There they became heated to the temperature of ca. 65 – 70 °C due to the dissipation of energy in plasma. In main series, when samples were above the powered electrode at floating potential, their heating resulted in lower temperature of ca. 35 – 40 °C. In this second case, unlike the first one, the effect of buckling was absent on the flat dust-free part of film. It existed only around dust particles, which create additional stress as bas-reliefs in aforementioned work [196].

It should be added that in our case the VUV radiation of H_2 CCRF discharge crosslinks the film bulk under the SiO_x top layer. Therefore, its thermal expansion coefficient can differ from that of non-modified PDMS. However, deep regions are weakly affected by the VUV radiation, and it is expected that the thermal expansion coefficient of the bulk material remains higher than that of SiO_x top layer.

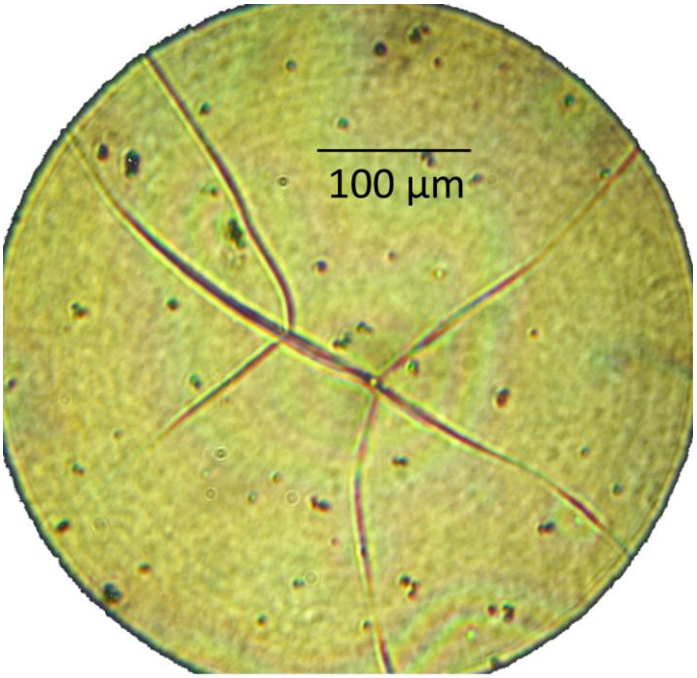

Figure 4.30. Cracked surface of a H_2 plasma modified PDMS film, which had initial thickness of ca. 480 nm. Blurred dark spots arise from dust particles in the optical way of microscope. More clear spots are dust particles appeared on the film after the modification.

Another example of surface defects is given in Figure 4.30. If the initial thickness of PDMS films exceeds 300 – 400 nm, then plasma-modified films become covered with a net of microcracks over their total area. In this case the VUV radiation absorbed in upper layers is not able to modify

the bottom of films. As a result, the films are not adhered to the substrate. In the case with the formation of wavelike structures all films were thinner and, therefore, modified across the whole depth and well adhered to substrates. The reaction force from the interface substrate-film bottom prevents strong compression in the lateral direction. (The substrate material, either Al coated glass or Si, - in both cases the volumetric expansion coefficient is strongly less than that of PDMS.) For thicker films with a liquid bottom the reaction force is negligible and the lateral compression should be stronger and. Thus, it leads to the cracking of SiO_x top layer.

Conclusions

Careful monitoring of the film deposition and the plasma processing conditions on all stages allows avoiding the. Specifically, it is necessary:

- To avoid the accumulation of dust in the liquid film. Samples should be immediately loaded to a plasma chamber. The work in a cleanroom will be useful in this case.

- The intensity of ultraviolet radiation should not to exceed $5 - 7$ mW/cm^2 to prevent the accumulation of gaseous products of VUV photolysis in the film leading to film damage.

- To prevent film heating (e.g. by cooling), which leads to their expansion and, afterwards, to buckling or cracking during cooling down.

- The thickness of the film should not exceed 300 - 400 nm to avoid the film cracking. Otherwise, the film should be crosslinked over the whole depth in a more efficient way, e.g. by more intensive excimer or exciplex lamps/lasers (Xe_2^*, ArF^*), which have a narrow emission spectrum in the region of relatively small absorption coefficient (see Figure 4.17).

Following these requirements it is possible to produce solid films of good quality. Such films are well adhered to the substrate, can withstand moderate load during rubbing and scratching. Their surface is smooth, what was necessary for their diagnostics and characterization by means of IRRAS and SE in this work.

4.4.2. Optical properties of prepared and plasma modified PDMS films

A single layer Cauchy model without absorption [75,76] was used to for non-modified and modified PDMS films to calculate the film thickness and dispersion of the refractive index from the measured ellisometric angles Psi and Delta in the wavelength range from 300 nm to 800 nm.

$$n(\lambda) = A + \frac{B}{\lambda^2} + \frac{C}{\lambda^4} \tag{4.8}$$

As it will be shown later, modified thicker films have non-uniform structure across the film thickness: the SiO_x top layer, transitional cross-linked region with gradual increase of CH_3 group concentration and very weakly cross-linked region. Nevertheless, the single layer model for plasma modified film was applied because of following reasons. In the film the refractive index changes gradually between two limit values for top SiO_x and for non-modified PDMS (see Figure 4.31).

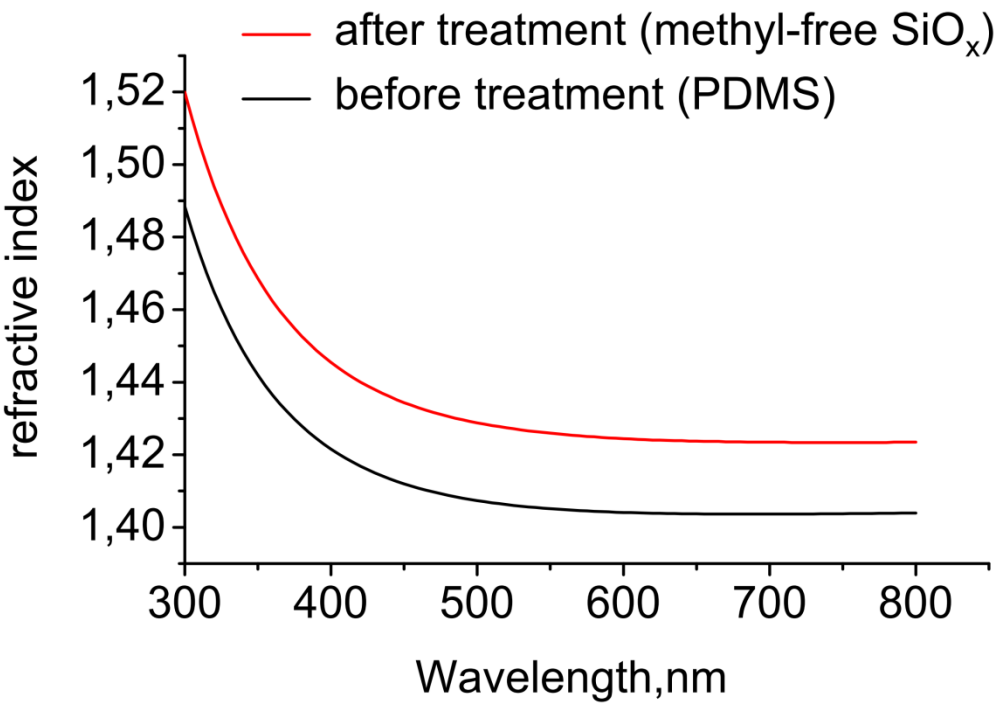

Figure 4.31. Refractive index of PDMS, measured from 12 nm film and refractive index the same film, measured after its complete transformation to methyl-free SiO_x layer by H_2 plasma treatment.

It is seen that the refractive index dispersion curves for these two cases are close to each other. Moreover, there is no distinct interface between the top methyl-free SiO_x and the below-lying region. It was tried to apply the Cauchy model with two layers to describe simultaneously the SiO_x top layer and the modified bulk. The iterative routine always converges to the state, when the thickness of SiO_x layer is zero and the thickness of bulk is nearly equal to those in single layer Cauchy model. It was also tried to fix the thickness of SiO_x layer at some virtual value, for example. In this case the total film thickness was equal to the thickness for the single layer model. Going from these results and considerations the application of a multilayer model is not very reasonable. The same model for non-modified as well as for modified PDMS films were applied elsewhere.[205-207] In particular in [206,207] the application of single layer model was explained as follows:

"The apparent thickness reported is the result of analysis of the data with a single layer model. Because the SiO_x layer was very thin, attempts to model the film thickness by a two-layer model (i.e. PDMS plus SiO_x) did not provide superior representations of the data than did a simple single layer model." [206,207]

"In general SE is rather sensitive to small changes in the refractive index and/or layer thickness. However, in the case of stratified layers the correlation between refractive index n and layer thickness d is significant and small changes of n may be compensated by changes of d. The refractive indices of PDMS (1.405) and SiO_2 (1.457) are very similar; therefore, applying a multilayer model is not very reasonable, and the analysis was limited to a single layer model." [205]

4.4.3. IR absorption spectrum of non-modified and plasma modified PDMS films

Absorption spectra of non-modified films

The characteristic absorption spectrum of a thin PDMS film with the thickness of about 210 nm is shown in Figure 4.32. The spectrum of the PDMS thin film is characterized by methyl groups which exhibit two stretching vibration modes: asymmetric one at 2965 cm^{-1} and symmetric one at 2906 cm^{-1}. [113,116,208] Further, the strong and very sharp band at 1266 cm^{-1} belongs to symmetric deformation vibration of $Si\text{-}CH_3$ group, and the asymmetric deformation band for $Si\text{-}CH_3$ at 1413 cm^{-1} has peak, respectively. The bands at 866 cm^{-1} and at 824 cm^{-1} correspond to $Si\text{-}(CH_3)_2$ asymmetric and symmetric rocking vibrations. The last one is overlapped with the band at approximately 800 cm^{-1} for the Si-C asymmetric stretching vibration in $Si\text{-}(CH_3)_2$. The bands at 1043 cm^{-1} and 1112 cm^{-1} represent the Si-O-Si asymmetric stretching vibrations.

Absorption spectra of plasma modified PDMS films

The hydrogen plasma treatment of the PDMS film results in strong changes of the IR spectrum (Figure 4.32). The overall decrease of characteristic PDMS absorption bands, that means all methyl group bands and the Si-O-Si asymmetric stretching band at 1112 cm^{-1}, as well as the formation of a new band at 1230 cm^{-1} were observed. The band degradation for vibration modes of CH_3 and $Si\text{-}CH_3$ groups is an indication of partial demethylation in the film, which appears due to the photodegradation of PDMS. In Lee and Graves the influence of VUV radiation on low-k SiOCH films was studied.[135] It was shown that, the VUV photons cause the demethylation of material and the formation of SiO_x overlayer. The release of CH_3 radicals was detected by mass spectrometry as the evidence of Si-C bond scission. In another work the mechanism of VUV photolysis of tetramethylsilane ($Si(CH_3)_4$) was studied.[182] It was found out that the photodecomposition has two main channels: the photoexcitation into the lowest Rydberg state is followed by Si-C bond breaking or by methane elimination, respectively. For the symmetric deformation vibration mode of $Si\text{-}(CH_3)$ not only degradation, but also the appearance of a shoulder, situated between 1270 cm^{-1} and 1285 cm^{-1}, was observed (Figure 4.32 C). This shoulder arises due to

substitution of methyl groups by oxygen atoms, and is the evidence of CH_3 group removal from the film.[209,210]

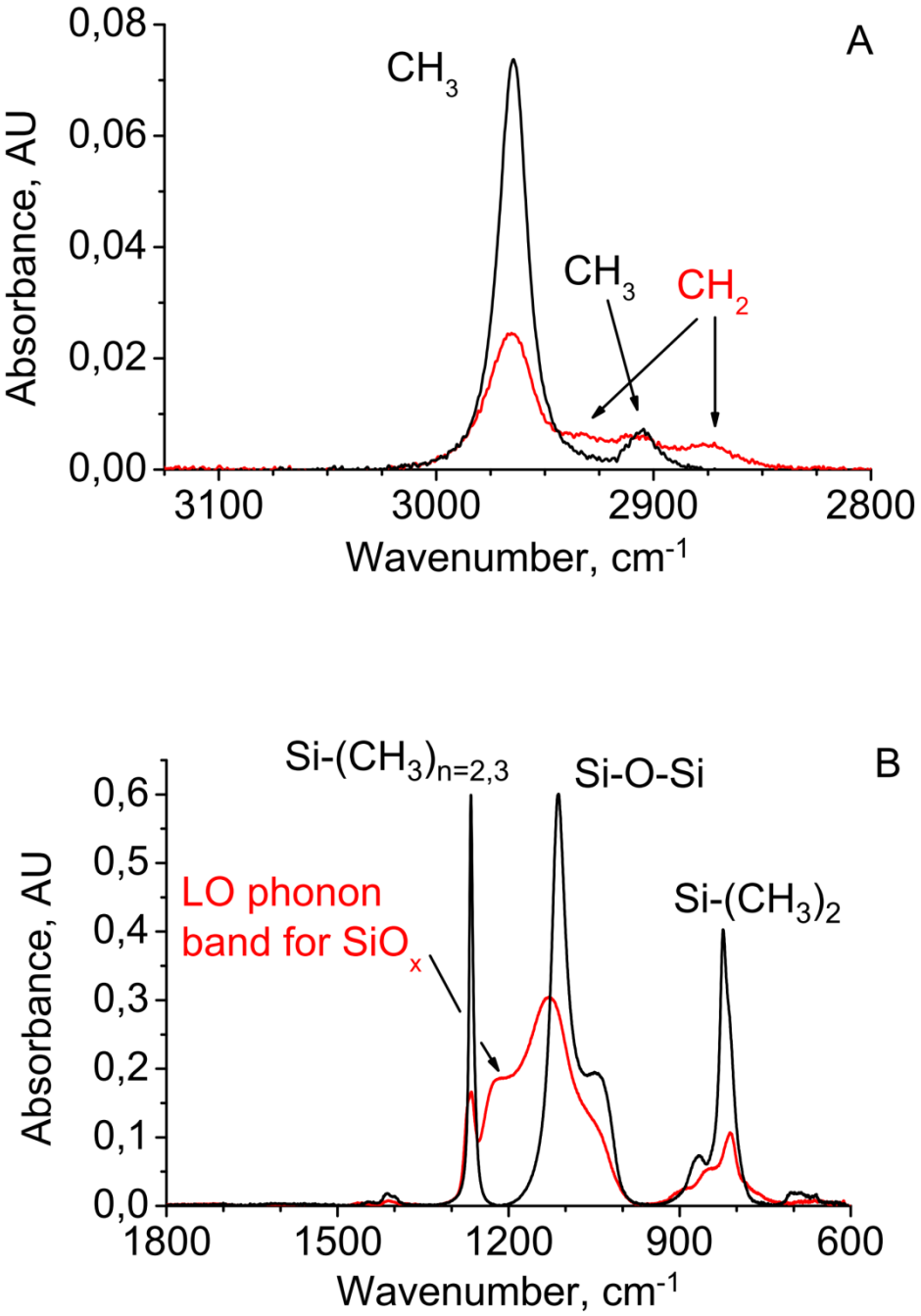

Figure 4.32. The IR spectra of non-modified (black) film with the thickness of 210 nm and film treated during 10 min (red) for different wavenumber intervals. Part C is on the next page.

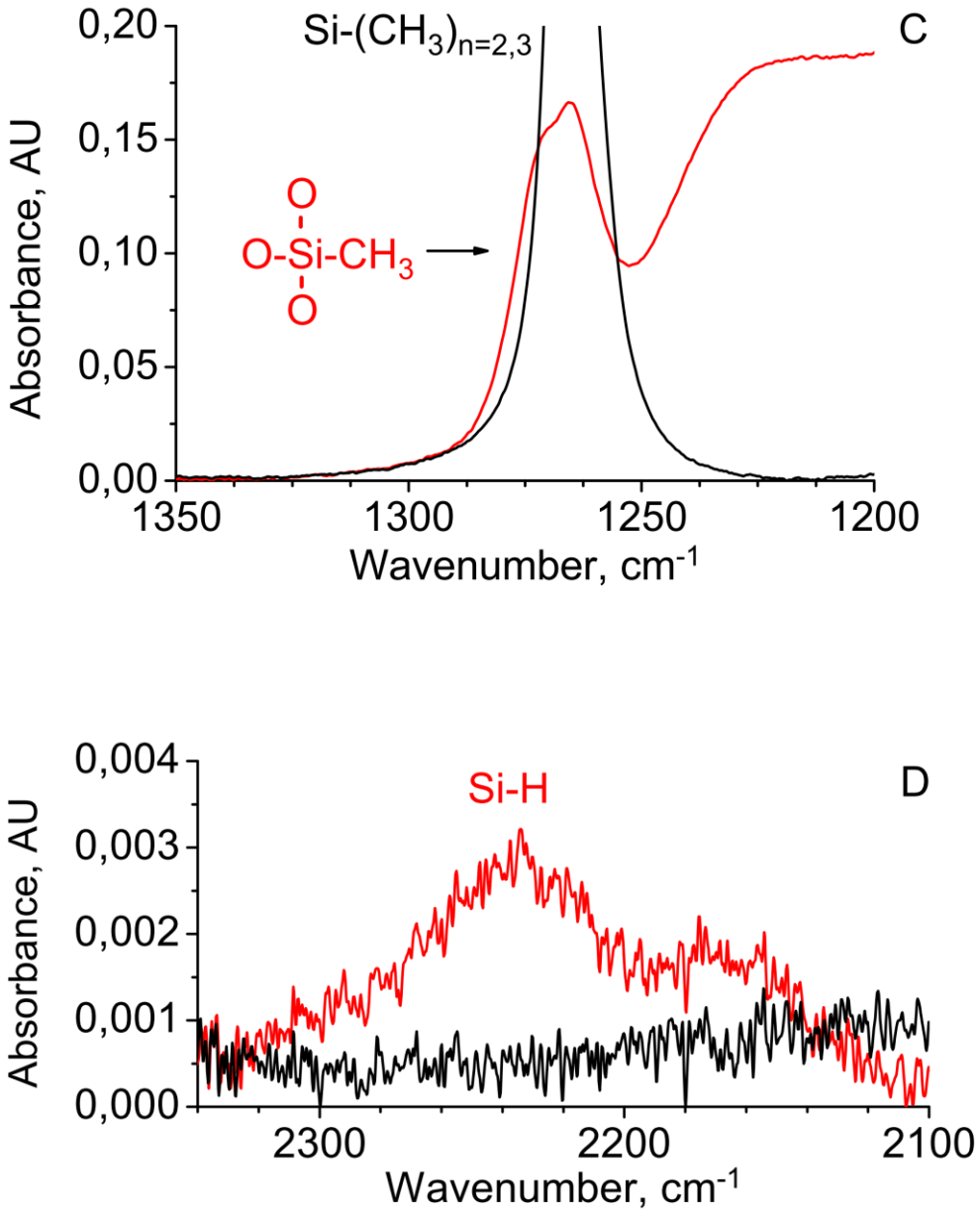

Figure 4.32. The IR spectra of non-modified (black) film with the thickness of 210 nm and film treated during 10 min (red) for different wavenumber intervals.

The strongest modification of the PDMS film is observed for the top layer, leading to the rapid removal of all CH_3 groups and formation of SiO_x layer. In the IR spectrum the presence of this layer is indicated by the new absorption feature at 1230 cm^{-1} called the Berreman mode. [211,212] It is the longitudinal optical (LO) phonon structure generated by surface charges due to the normal component of electric field strength of incident

IR radiation. Additionally, all modified films have small content of CH_2, which is indicated by the presence of two weak bands at 2875 cm^{-1} and 2933 cm^{-1} for symmetric and asymmetric stretching vibrations. The appearance of Si-H bonds is confirmed by the band at 2235 cm^{-1}.The detailed list of main absorption bands is presented below in the Table 4.1.

Table 4.1. List of the main absorption bands of non-modified and plasma modified PDMS (SILFAR® 1000) films

Non-modified PDMS film

Wavenumber, cm^{-1}	Mode of vibration	Ref.
2965	CH – asymmetric stretching, CH_3	[84]
2906	CH – symmetric stretching, CH_3	[84]
1443	CH – asymmetric deformation (in-phase), CH_3	[208,213]
1413	CH – asymmetric deformation (out-of-phase), CH_3	[84,214]
1266	CH – symmetric deformation, CH_3 (Umbrella)	[84,214]
1112	Si-O-Si asymmetric stretching	[84,214]
1043	Si-O-Si asymmetric stretching	[84,214]
866	CH_3 – asymmetric rocking, Si-$(CH_3)_2$	[113,117,214]
~845	CH_3 – asymmetric rocking, Si-$(CH_3)_3$	[113,117]
824	CH_3 – symmetric rocking, Si-$(CH_3)_2$	[113,117,214]
~800	Si-C – asymmetric stretching, Si-$(CH_3)_2$	[113,117]

New bands in modified PDMS film

Wavenumber, cm^{-1}	Mode of vibration	Ref.
3100 − 3700	OH, stretching vibration, H_2O and SiOH	[84,214]
2930	CH – asymmetric stretching, CH_2	[84]
2873	CH – symmetric stretching, CH_2	[84]
2235	Si-H, stretching vibration	[84,214]
1660	OH, scissoring vibration, H_2O	[84,214]
1230	LO phonon band (Berreman mode), SiO_x	[211,212]
945	Si-O, stretching vibration, Si-OH	[84,214]

4.4.4. Chemical reactions in PDMS films during the plasma modification

From the comparison of the spectra of modified and non-modified films it is possible to propose several reactions which take place in films during the plasma modification. The CH_2 groups appear because of the formation of Si-CH_2-CH_3 or cross-linking with the production of Si-CH_2-Si and/or Si-CH_2-CH_2-Si (see Reactions 1-3). The presence of Si-CH_2-CH_2-Si structure in PDMS films modified by VUV photolysis was also suggested by Skurat and Dorofeev. [129]

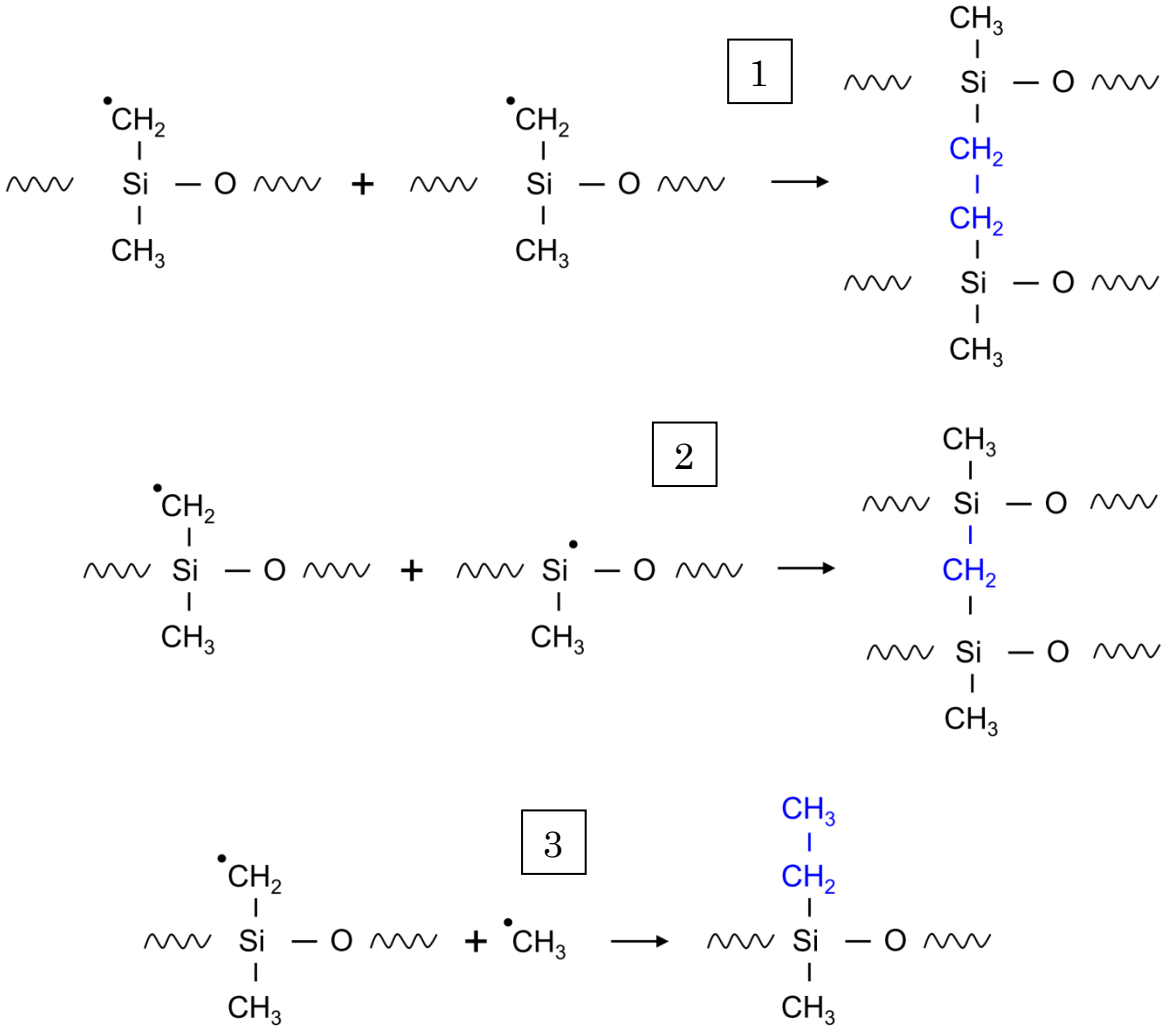

The reaction 4 demonstrates the way of Si-H group production trough the reaction of atomic hydrogen with the dangling bond. It was observed that the absorbance of the corresponding band (Figure 4.32) is very weak and

does not depend on film thickness. Therefore, the formation of Si-H takes place only on the surface of films. The formation of this bond was observed only in H_2 plasma, but not in Ar, Xe or O_2. Thus, we can conclude that atomic hydrogen comes to the surface from the H_2 plasma. Also the intensity of the Si-H stretching vibration band does not depend on the film thickness if it exceeds 5 – 10 nm. It means that the penetration depth of hydrogen atoms is very limited and Si-H bonds are concentrated only in the near-surface layer.

4

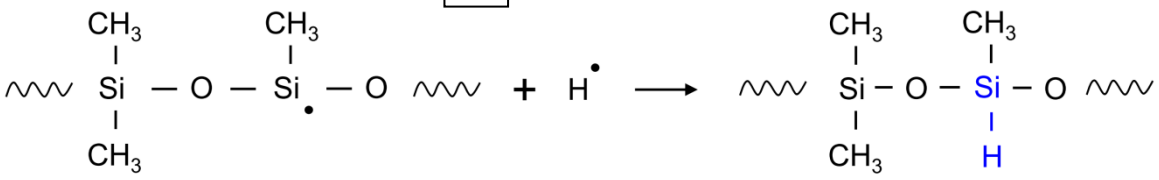

The appearance of a shoulder of the Si-CH_3 symmetric deformation band at 1266 cm^{-1} can be explained by the reaction 5. According P. J. Launer the position of this band shifted to higher wavenumbers indicates the substitution of the CH_3 group by an oxygen atom.[209]

5

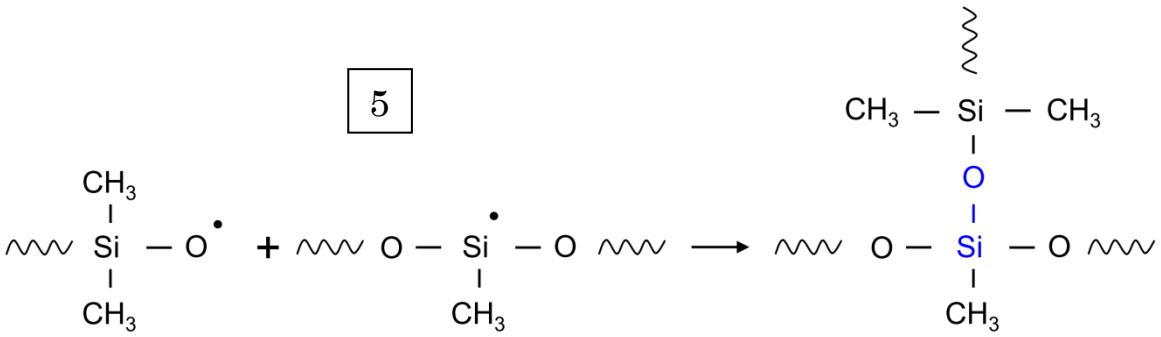

Reactions taking place in the film are not limited to these five. An additional analysis can help to reveal other reaction channels of PDMS plasma modification.

4.4.5. Interference effect in thin film IRRAS spectra.

The absorbance of non-modified and, therefore, homogeneous films can be measured and compared with the thickness determined by SE. Then the plot "absorbance vs. thickness" gives the opportunity to derive film thickness from the absorbance spectrum.

It might be erroneously assumed, that like in the standard transmission technique the Beer-Lambert law takes place and the dependence is linear. However, for thin films it can be not the case. Figure 4.33 demonstrates us peak absorbances of various bands vs. film thickness (see Table 4.1).

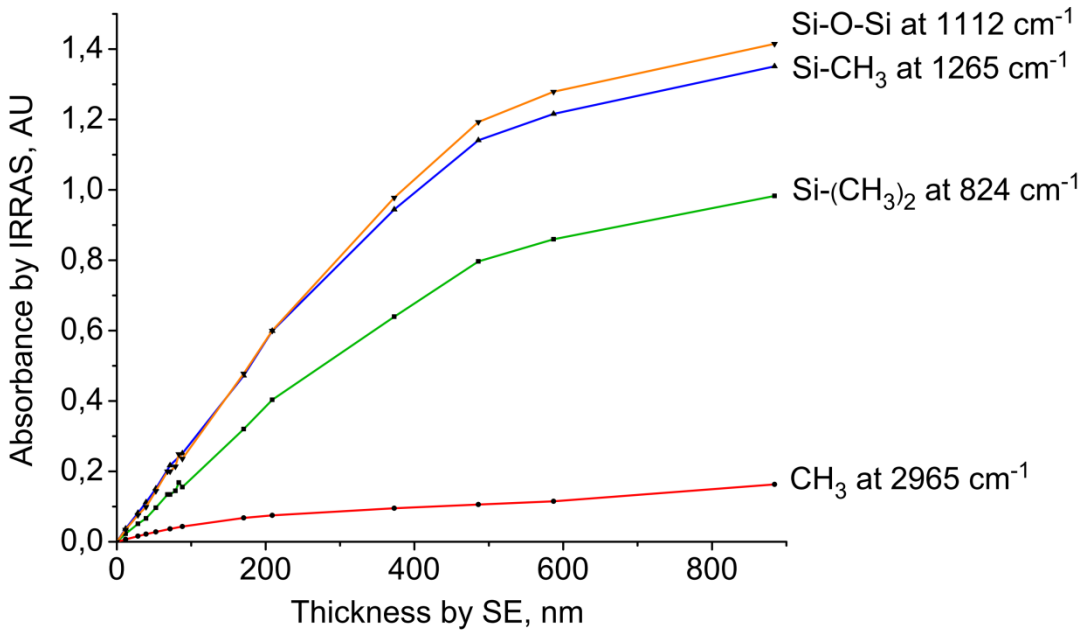

Figure 4.33. IR peak absorbance of various bands as functions of PDMS film thickness.

Initially the linear function becomes non-linear for all bands. The thickness, where the function is still linear, is smaller for bands with higher wavenumbers (i. e. with lower wavelengths). The effect arises due to the interference taking place for thin films. A part of IR beam undergoes multiple reflections from interfaces vacuum – PDMS film and PDMS film – substrate, a part of it comes back in a vacuum and interferes with another part of beam reflected from the interface

vacuum – PDMS as it is demonstrated in Figure 4.34. It should be noted, that this effect is not because the optical path difference between the incident and reflected radiation. For example, the wavenumber of 824 cm^{-1} corresponds to the wavelength of 12.136 μm, which strongly exceeds the thickness of films studied in our work. Therefore, the effect due to the optical path difference is negligible, and for the spectral region without absorption such interference does not exist. Actually, a phase difference between the incident and reflected beam accumulates due to the absorption and leads to the observed interference effect.[211,215-218]

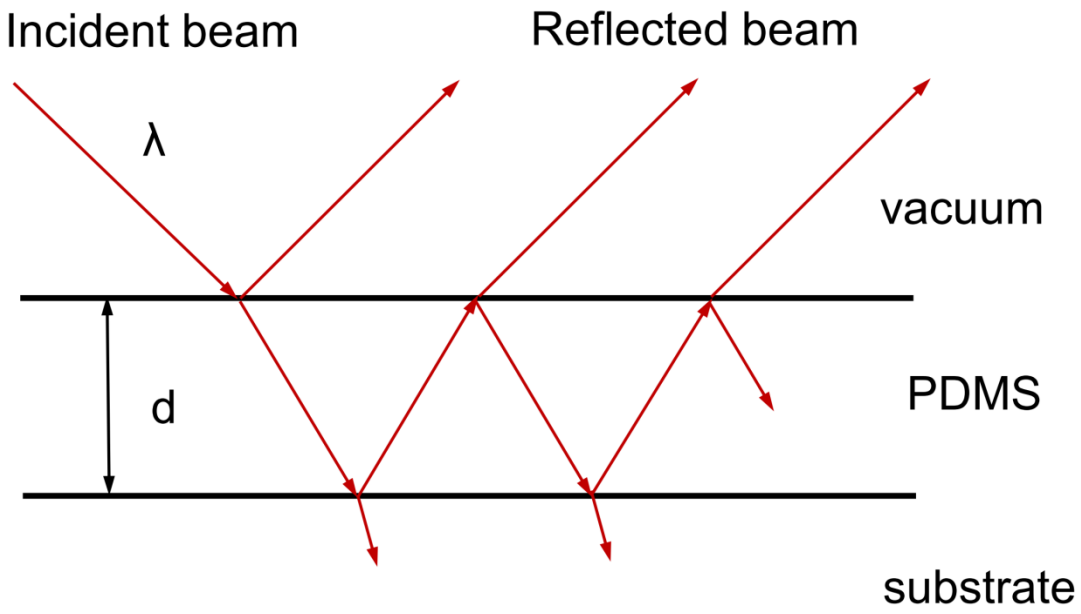

Figure 4.34. Explanatory drawing for the interference effect.

This effect can be calculated. The final expression for the reflection coefficient R, which is the ratio of the total intensity of all beams reflected by the system to the intensity of the incident beam, can be found in following works.[211,215,217] The formula from [211,215] is convenient for programming:

$$R = \left| \frac{(Q_1 - Q_2)(Q_2 + Q_3)\exp(4\pi Z_2 d/\lambda) + (Q_1 + Q_2)(Q_2 - Q_3)}{(Q_1 + Q_2)(Q_2 + Q_3)\exp(4\pi Z_2 d/\lambda) + (Q_1 - Q_2)(Q_2 - Q_3)} \right|^2 \qquad (4.9)$$

where $Q_i = Z_i$ for s-polarized radiation,
$Q_i = \varepsilon_i / Z_i$ for p-polarized radiation,
$Z_i = \sqrt{\varepsilon_1 \sin^2 \varphi - \varepsilon_i}$, $\varepsilon_i = n_i^2 - k_i^2 + 2in_ik_i$, $i = 1,2,3.$
φ - incidence angle, n_i and k_i - refractive index and extinction coefficient, respectively.
In our case 1 is for vacuum, 2 for PDMS, 3 for substrate.

4.4.6. Treatment of ultrathin films (~ 10 nm) by the VUV radiation from H_2 plasma vs. direct plasma treatment.

As it was described in the Chapter 6 the depth of penetration of ions accelerated in the powered electrode sheath can be up to 5 - 10 nm. In this connection it was interesting to study to compare influence of only plasma VUV radiation and direct plasma (VUV, ions, atoms molecules,…) on films with the thickness of ca. 10 nm. For that, the separate experiment was realized, which scheme is presented in Figure 4.35. (see also [192]) Plasma treatment conditions were comparable with those for the main line of experiments (see Chapter 5, Table 3.1). The main parameters of the discharge are listed in Table 4.2.

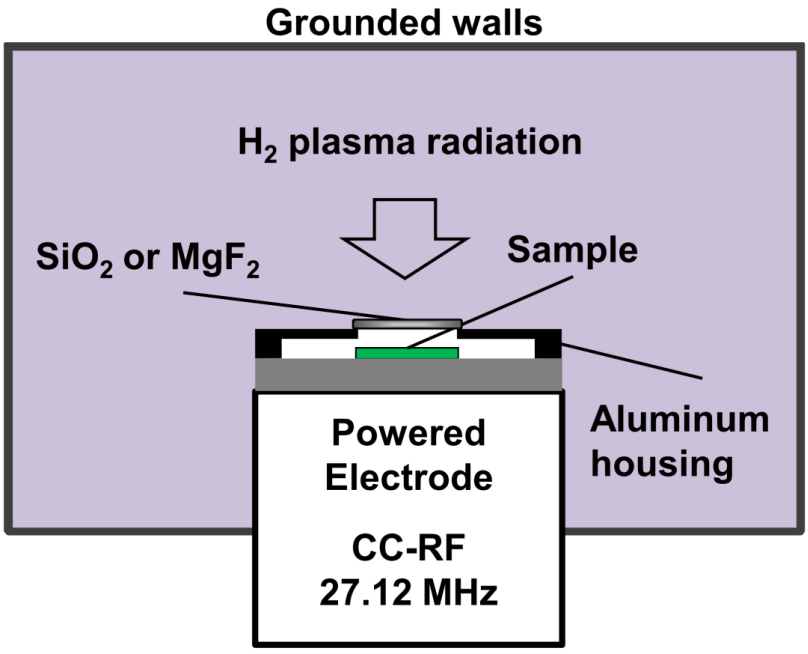

Figure 4.35. Scheme of the experiment for the comparison of influence of only plasma VUV radiation and direct plasma (VUV, ions, atoms molecules,…) on films with the thickness of about 10 nm. A gas exchange between reactor and internal volume of the housing is free. In the series of experiments with direct plasma treatment the aluminum housing with window was absent.

Table 4.2. Parameters of the discharge for the separate experiment described in this section.

Processing gas	H_2
Discharge type	CCRF, 27.12 MHz
Base pressure	≈ 2 Pa
Process pressure p	26.7 Pa
Gas flow f	28 sccm
Forward power	200-300 W
Full reactor volume V	ca. 30 L
Residence time t_r	17 s
Powered electrode surface area	64 cm^2
Treatment time	30 - 1800 s

The samples were placed on the surface of the powered electrode. In one series of experiments they experienced the influence of all plasma components. In another series they were covered by aluminum housing with a window. The housing covered all area of powered electrode, and it had free gas exchange with the main volume of chamber. On its top a window covered the circular 25 mm aperture to avoid the interaction of the PDMS film with the plasma particles, but to allow the radiation to act on the film. The housing prevented also excitation of plasma in its internal volume. The distance between the PDMS film and the top side of the window was 5 mm.

Three different window materials were used in different experiments: soda-lime glass with the cutoff of 330 nm and with the thickness of 1 mm, quartz glass (SQ 1) with the cutoff of 160 nm and with the thickness of 1 mm, and the MgF_2 window with the thickness of 2 mm and transmittance exceeding 90 % for normal incidence of light with wavelength in the range between 120 nm and 200 nm. (See Figure 4.21, another thickness in this case should be taken into account for recalculation of transmittance)).

The treatment with soda-lime glass has no effect on liquid PDMS films as expected. During the treatment with the quartz glass window the samples were irradiated by a part of VUV radiation, mostly by radiation from dissociation continuum (see Figure 8 in [192]) . The strongest VUV emission of hydrogen plasma is located below 165 nm, but the

transmission cut-off of the quartz glass is about at 160 nm. In this case the transmitted radiation is not intensive, which results in the small effect in the PDMS film modification. The H_2 plasma irradiation of PDMS film with thickness of 10 nm during 180 s showed reduction of only 13 % for peaks indicating the presence of methyl groups and 8 % of Si-O-Si asymmetric stretching peak. In the third series of experiments the PDMS sample was screened with the MgF_2 window. In this case the treatment effect is much stronger (Figure 4.36). This result is concordant with results already reported in Jung et al., where the influence of H_2 plasma VUV radiation filtrered by LiF window was compared for alkyl- and silanol-containing SiO_2 aerogel films.[219]

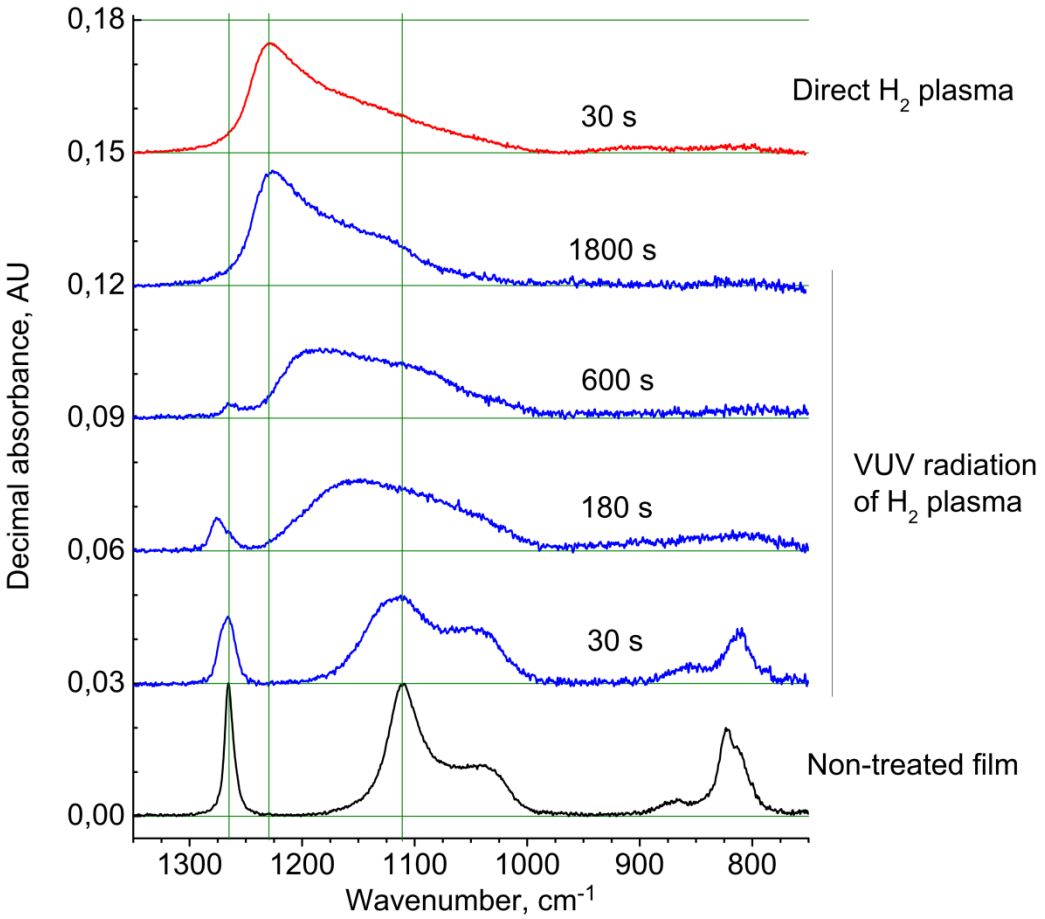

Figure 4.36. IR absorbances of thin films with initial thickness of 10 nm, modified by H_2 plasma (red) or by H_2 plasma VUV radiation (blue).

The latter case of irradiation through MgF_2 window is compared with the direct H_2 plasma action in Figure 4.36. The IR spectrum of the 10 nm film treated during 30 s in H_2 plasma exhibits only LO phonon band, all methyl groups are removed and destroyed. On the other hand, the

IR spectrum of the 10 nm film treated during 30 s by plasma VUV radiation demonstrates the degradation of all main characteristic PDMS bands, but no appearance of LO phonon band at 1230 cm^{-1}. Further increase of treatment time to 180 s, 600 s and up to 1800 s leads to a continuous change of the IR spectrum. We see the appearance of LO phonon band, indicating the presence of SiO_x . This band shifts gradually to higher wavenumbers up to 1230 cm^{-1}. Mirley and Koberstein modified Langmuir-Blodgett layers of diacid-terminated PDMS into ultrathin SiO_x films by treatment with the low pressure mercury-quartz lamp, which generates VUV/UV light in the 185 and 254 nm range.[220] Dölle et al. transformed 220 nm PDMS films in nitrogen atmosphere (the vessel was evacuated to the pressure of 50 mbar and then filled with nitrogen) to carbon containing SiO_x material by strong VUV radiation of Xe_2^* excimer lamp.[221] In both works, like in our, the gradual shift of LO phonon peak to higher wavenumber was observed. Even when the irradiation intensity is strong, like that in Dölle et al. (about 70 mW/cm^2), the LO peak shifts slowly (tens of minutes) to the final position at 1230 cm^{-1}.[221]

The shift to higher wavenumbers can take place due to the increase of the stoichiometric index of SiO_x material, as it was calculated in Lehmann et al.[222] In our case additional oxygen in the film can appear in plasma as residual impurities like O_2 and H_2O molecules. The emission of O_2 molecules was not observed by OES, the emission from OH radicals originating from H_2O is always present. Another interpretation of the band shift is connected with the change of SiO_x film porosity. In Brunet-Bruneau et al. the peak shift from 1120 cm^{-1} to 1245 cm^{-1} was related to the porosity decrease from 50 to 0 percents in the SiO_2 film.[223,224] But the shift is most likely the result of consecutive changes in the chemical structure of the film as it looks from comparison of absorbance spectra for different treatment time. The immediate appearance (within few seconds) of this peak at 1230 cm^{-1} is typical only for direct plasma treatment. This situation demonstrates us the rapid transformation of PDMS to SiO_x, but not gradual, like in the case of the treatment by plasma VUV radiation.

Increase of the treatment time results also in the degradation of all bands, indicating the presence of methyl groups. This degradation of CH_3 bands is accompanied by the shift of Si-CH_3 symmetrical deformation band due to the substitution of methyl group by oxygen atoms (like it was described in Section 4.4.3). Following substitution or destruction of the last CH_3 group bonded to Si removes the shifted shoulder, and after 600 s of irradiation only a weak residual peak of symmetrical deformation band is seen at the initial position. Meanwhile, the Si-O-Si asymmetric

stretching band undergoes prominent changes. Initially, the band absorption intensity decreases, withal the band shape broadens out.

Finally, after 1800 s of treatment by plasma VUV radiation the absorbance spectrum is similar with that for direct H_2 plasma treatment over 30 s, – the final state of films is the same – methyl-free SiO_x layer.

It should be noted that in the experiments with housing different factors reduce the intensity of irradiation by VUV light, and decelerate the thin film modification. One of them is the intensity reduction due to the decrease of the angular aperture to about 136°. Another one is the absorption of radiation by the window material, which is stronger for non-normal incidence. Also, H_2 plasma exhibits emission below the cut-off wavelength (115 nm) of the MgF_2 window.[225] This radiation is missing in experiments with the treatment by only VUV light. However, its intensity is expected to be much weaker than that of the Lyman band system, and its influence should not be strong. All this factors, however, don't explain the drastically slower modification effect of thin film by plasma VUV.

As it was mentioned previously (see Section 4.1) the ion bombardment at the powered electrode is energetic enough to dissociate chemical bonds and modify the film. Additionally, fast or thermal hydrogen atoms can modify the top layer of the film. Therefore, this rapid transformation should be referred to the action of particles (H^+, H_2^+, H_3^+, H, H_2) striking the film surface, which is likely the main factor in modification of very thin (~ 10 nm) films or the top layer of thicker films by the direct H_2 plasma treatment.

4.4.7. Shrinkage of films during plasma modification and distribution of CH_3 groups across the film thickness.

In this Section the influence of radiation on films with initial thickness in the range 10 - 600 nm will be discussed. As we know the plasma particles can only modify very top surface layer of PDMS. On the other hand VUV radiation penetrates deeper and modifies the film bulk. Its intensity decreases continuously on the way of propagation. Therefore, upper layers experience strong irradiation, while the deeper regions can remain unmodified, if the film is originally thick. An intensive VUV radiation dissociates chemical bonds, crosslinks the film, destroys and removes CH_3 groups. This leads to a film shrinkage during the treatment and to the formation of gradient distribution of CH_3 along the film thickness. The shrinkage was studied by SE and the distribution of CH_3 groups by IRRAS.

Shrinkage of modified PDMS films

The thickness reduction of plasma modified PDMS films is presented in Figure 4.37 for different initial thickness and plasma treatment time. All plots show initially the linear dependence. For this part of plot the IR spectrum reveals that PDMS is completely converted into a SiO_x layer. Under the assumption that the Si content does not change during the PDMS film conversion into SiO_x layer, the shrinking ratio (final thickness/initial thickness) should be 0.55.[226] In our experiments such films had the shrinking ratio of approximately 0.55 - 0.60. This coincidence, additionally to SEM results (see Figure 4.27), shows the absence of big pores or voids in the SiO_x layer. No further thickness decrease and alteration of the IR spectrum of the SiO_x film was observed in subsequent plasma treatment. It should be noted here, that the thickness reduction of SiO_x layer due to etching or sputtering in plasma is absent for samples positioned at floating potential or at the surface of the powered electrode. This was proved in experiments. For example, 10 nm PDMS films were transformed to methyl-free SiO_x during 30 s. Afterwards, their thickness and IR absorption spectrum were measured, and the treatment was continued until 1800 s. Interim and final

measurements showed no thickness decrease and no IR absorption spectrum change.

Film regions below 100 nm are characterized by residual CH_3 content even after 30 minutes and lower shrinkage. For this case, the curves show the deviation from the initial linearity and, afterwards, a smooth transition into another linear part, which continues to the film-Al interface. For different treatment time the second linear part appears at different depth: for 3 minute – at 50 nm, for 10 minutes – at 150 nm and for 30 minutes – at 200 nm. In this region the radiation intensity is reduced because of the absorption in the overlaying material. It leads to weaker degree of CH_3 removal and weaker cross-linking in this region, and hence, to the lower thickness reduction. This linear part of the film is shrinked uniformly and shows approximately the same shrinking ratio of ca. 0.90 - 0.95 for different treatment times. Films with such weakly crosslinked region are characterized by low adhesion on the substrate. They can be easily wiped. In Graubner et al. PDMS films with the initial thickness between 50 and 730 nm were irradiated by Xe_2^* excimer lamp at 172 nm, and the reported results are similar to that demonstrated for the film shrinkage in this paragraph.[205]

The distribution of CH_3 across the film thickness in plasma modified PDMS

The distribution of the methyl group over the whole depth of the film is shown in Figure 4.37 A. It is seen that the top layer contains no CH_3 groups. This layer has only the IR absorption band indicating the SiO_x structure. Its thickness grows from 15 to 60 nm as the treatment time increases from 3 to 30 min. The removal of CH_3 groups due to the plasma treatment decreases their concentration in the film. On the other hand, the shrinking due to the crosslinking can increase the concentration of CH_3 groups. The slope of absorbance curves is proportional to the concentration of CH_3 in the film. Below the methyl-free layer the slope of curves and the concentration of CH_3 for modified films rise gradually. In the weakly cross-linked bulk the shrinking effect and the amount of removed CH_3 are low. Therefore, the slopes of curves tend to rise to those in the non-modified films. For 3 min treatment the slope in the bulk is already close to the slope for non-modified films. Longer treatment time leads to stronger removal of CH_3 in deeper film regions, which is indicated by the further reduced slopes (for example, 3 min vs. 30 min in Figure 4.37 B).

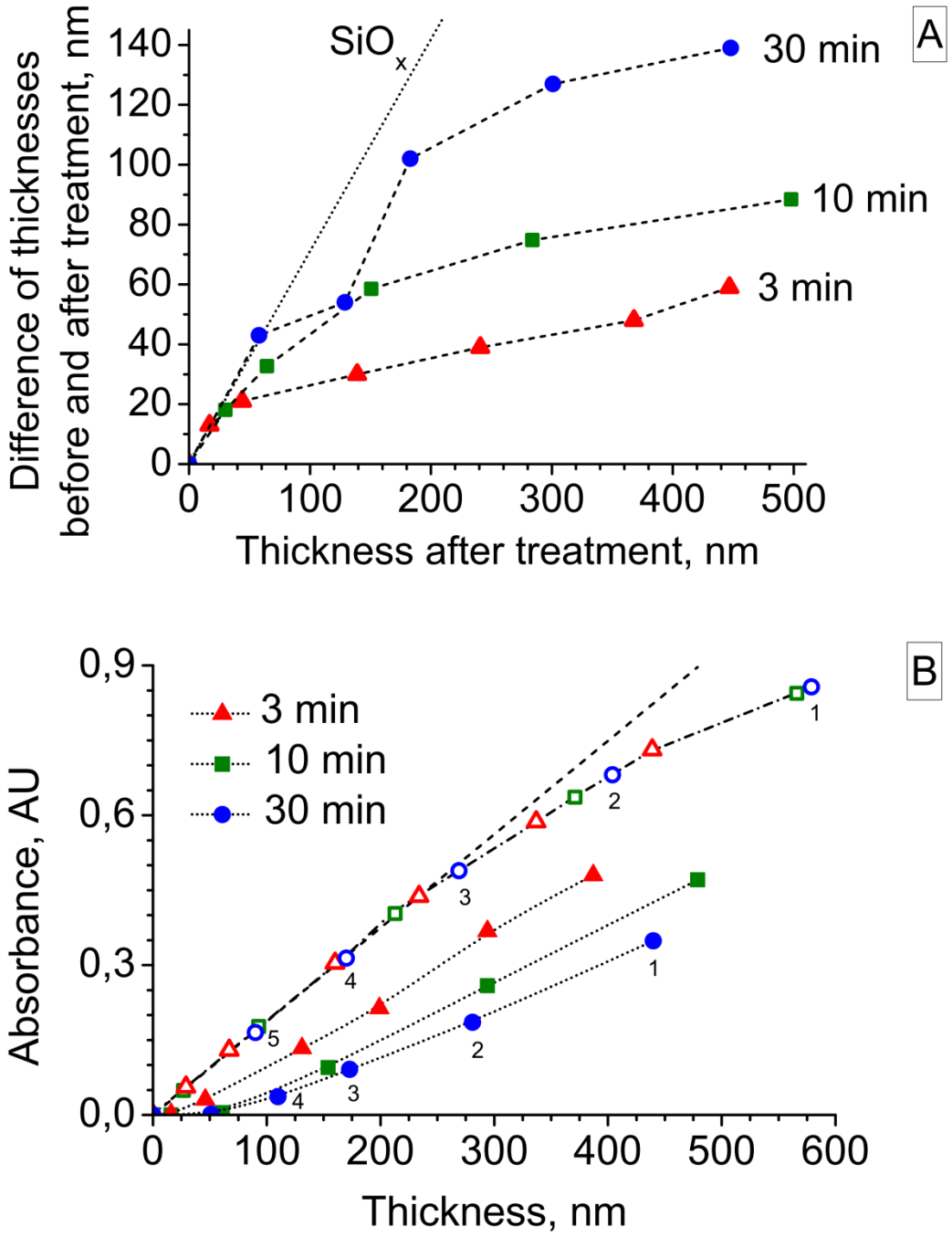

In figure (B) and (C) open symbols denote the absorbance of non-modified PDMS films and are plotted vs. initial film thickness, while closed ones for modified films are plotted vs. final film thickness. Additionally, for 30 min equal numbers show corresponding points to compare the IR absorbance and the thickness before and after treatment.

See the next page for continuation

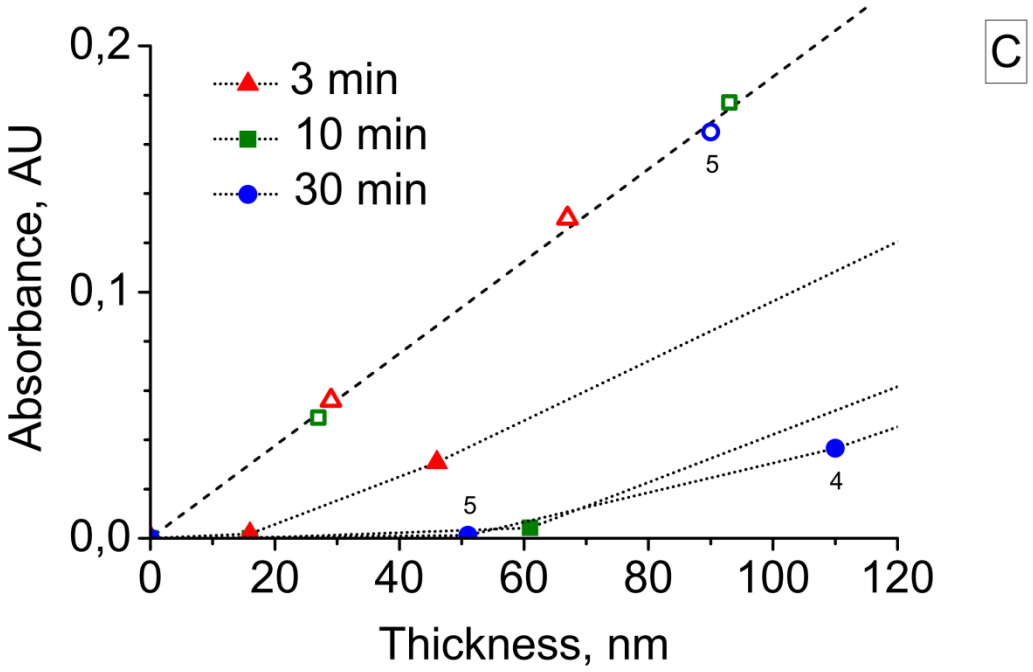

Figure 4.37. Thickness difference before and after treatment vs. thickness after treatment (A), and IR decimal absorbance of symmetrical rocking vibration peak of Si-$(CH_3)_2$ at 824 cm^{-1} for films treated during 3, 10 and 30 min (closed symbols) compared with that for films before treatment (open symbols) (B) and (C).

4.4.8. Influence of the treatment time on CH_3 reduction.

In Figure 4.38 the absorbance of CH_3 vs. treatment time is plotted for various initial thicknesses. Thin films with the thickness below 50 nm have lost almost all the methyl groups after 3 minutes treatment time and were converted into SiO_x material. With increasing treatment time the thickness of the top SiO_x layer gradually grows. However, films with the thickness greater than 100 nm are not modified completely into SiO_x after 30 minutes. A part of VUV radiation is absorbed by upper layers and the intensity decreases gradually for deeper film regions. Therefore, the rate of CH_3 group removal decreases with the time and the curves have a tendency to go into the constant value. Thus, an increased treatment time is very inefficient for the treatment of thick films. The strongest removal rate of CH_3 groups is observed at the beginning of the treatment. This dynamics correlates with the above described quick appearance and the growth of bubbles containing gaseous products including CH_3 groups. After about 5 - 10 min the rate of CH_3 removal

decelerates strongly and the damage effect stops. These and similar results were presented in articles. [192,227]

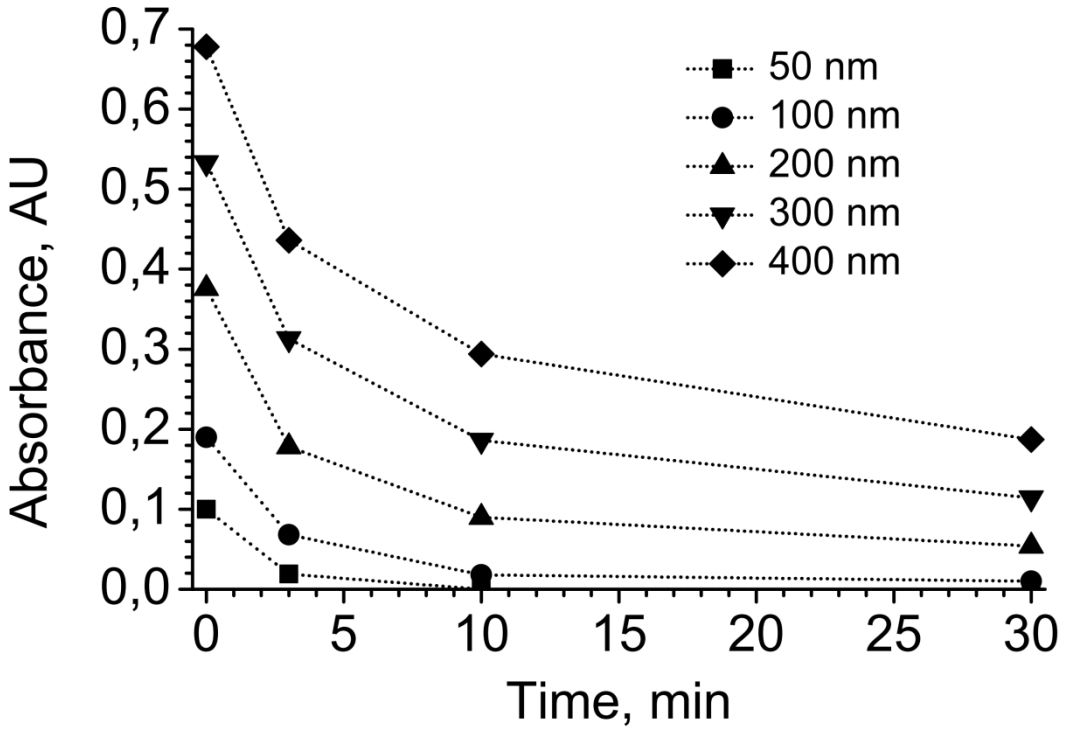

Figure 4.38. Absorbance for symmetrical rocking vibrations of Si-$(CH_3)_2$ at 824 cm^{-1} vs. treatment time for different initial thickness. The data are taken from the plots in Figure 4.37.

4.5. Photocatalytic performance of composite layers with TiO_2 nanoparticles

One of the basic ideas was to produce composite films consisting of TiO_2 nanoparticles embedded in a H_2 plasma-modified PDMS matrix. These composite films were provided by the Fraunhofer Institute for Manufacturing Technology and Advanced Materials in Bremen.[15]

To create a stable dispersion from hydrophilic anatase TiO_2 nanoparticles and hydrophobic PDMS it is necessary to perform a special routine for compatibilization.[228] It was realized by the bead milling of TiO_2 dispersed in a block copolymer. In this process polyether (in blue rectangle in Figure 4.39) is adhered to the surface of nanopraticles and silicone chains are oriented towards PDMS. It makes nanoparticles wettable by PDMS.

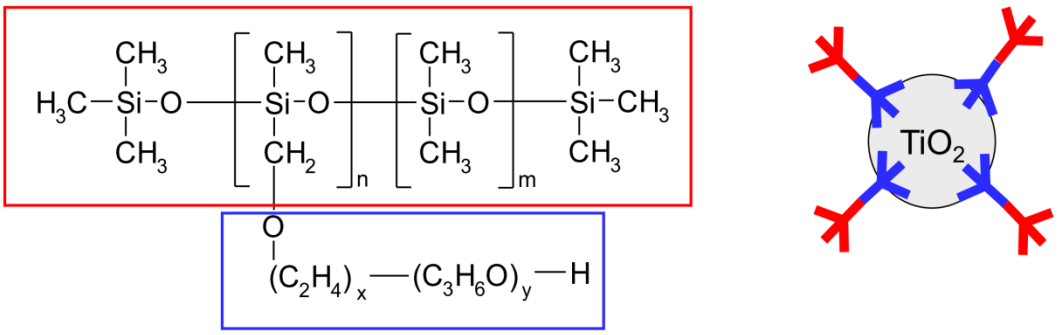

Figure 4.39 Compatibilization of TiO_2 nanoparticles with PDMS. Figure is adapted from [228].

Afterwards, the dispersion of PDMS and compatibilized TiO_2 nanoparticles was deposited to substrates by spin-coating and treated by plasma to create a solid photocatalytically active coating. As an example, the SEM micrographs of a plasma modified PDMS film with TiO_2 on a Si wafer are presented in Figure 4.40. Some particles merged into big agglomerates during the preparation, a part of particles remained separately. One of the TiO_2 crystalline configurations is anatase, which is advantageous for photocatalysis. It has a bandgap of ca. 3.25 eV.[229] The irradiation of TiO_2 nanoparticles by light of higher photon energy generates electron-hole pairs. A part of these pairs recombines in the bulk of TiO_2 nanoparticles, while the rest reaches the surface. The holes act like oxidants and the electrons like reductants initiating chemical redox reactions with adsorbed compounds. If holes react with H_2O molecules, OH radicals are produced, which have strong oxidizing potential of 2.8 eV. Redox reactions degrade different organics, viruses, bacteria, fungi, algae, and cancer cells to CO_2, H_2O, and harmless inorganic anions.[229-231]

The test of the photocatalytic performance was realized in the Fraunhofer Institute for Manufacturing Technology and Advanced Materials in Bremen. Two cuvettes, one with a composite film consisting of embedded TiO_2 nanoparticles in the plasma cross-linked PDMS film and another as a reference, were filled by aqueous solution of methylene blue (MB) to test MB degradation (Figure 4.41). Afterwards both cuvettes were irradiated by UV-A light during 24 hours. MB decomposition was detected by measurement of the absorbance in the visible range (Figure 4.41) and compared with the reference.

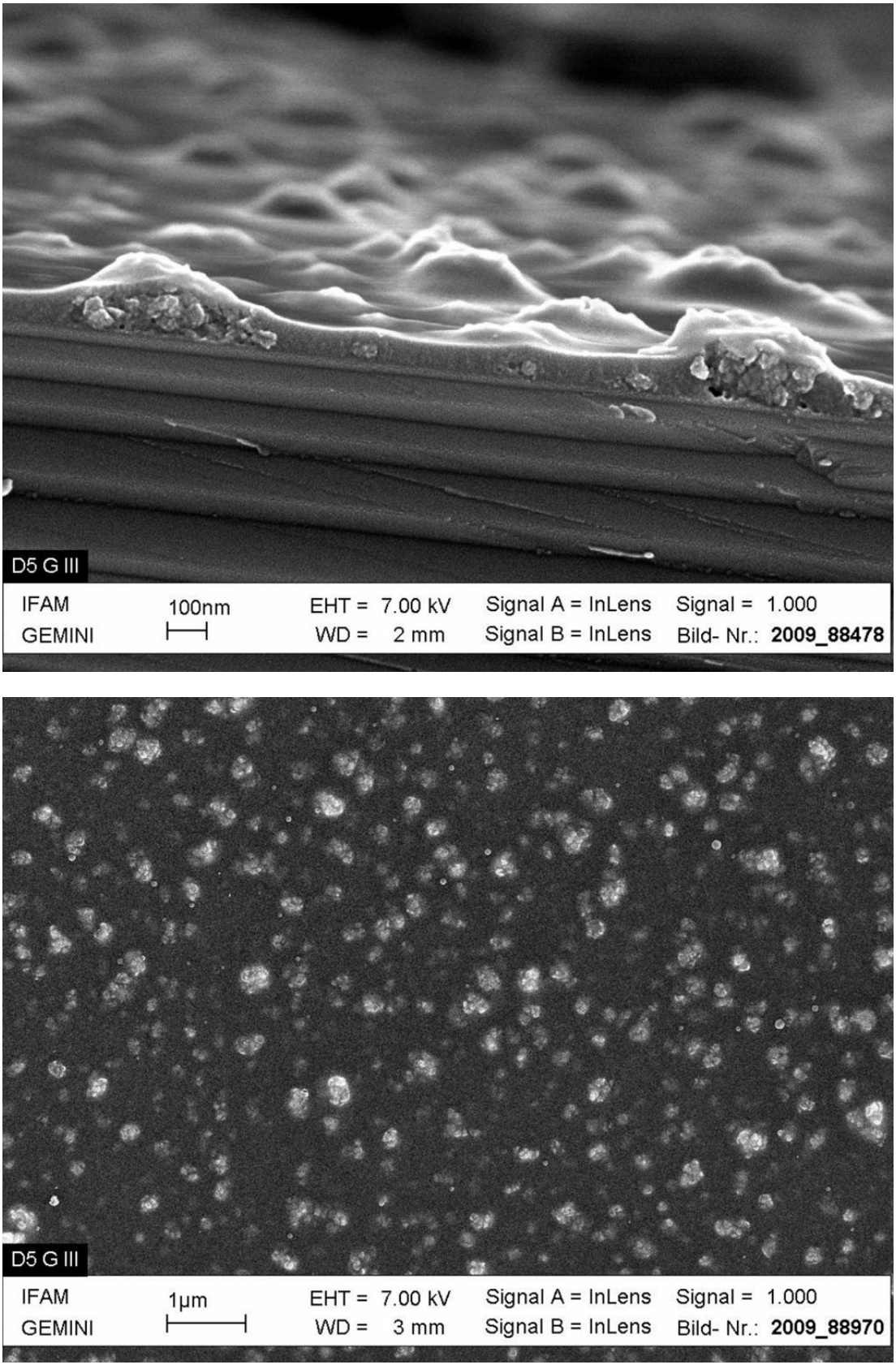

Figure 4.40. SEM micrographs of H_2 plasma modified PDMS film with TiO_2 nanoparticles. Side and top view. Adapted from [15,232,233]

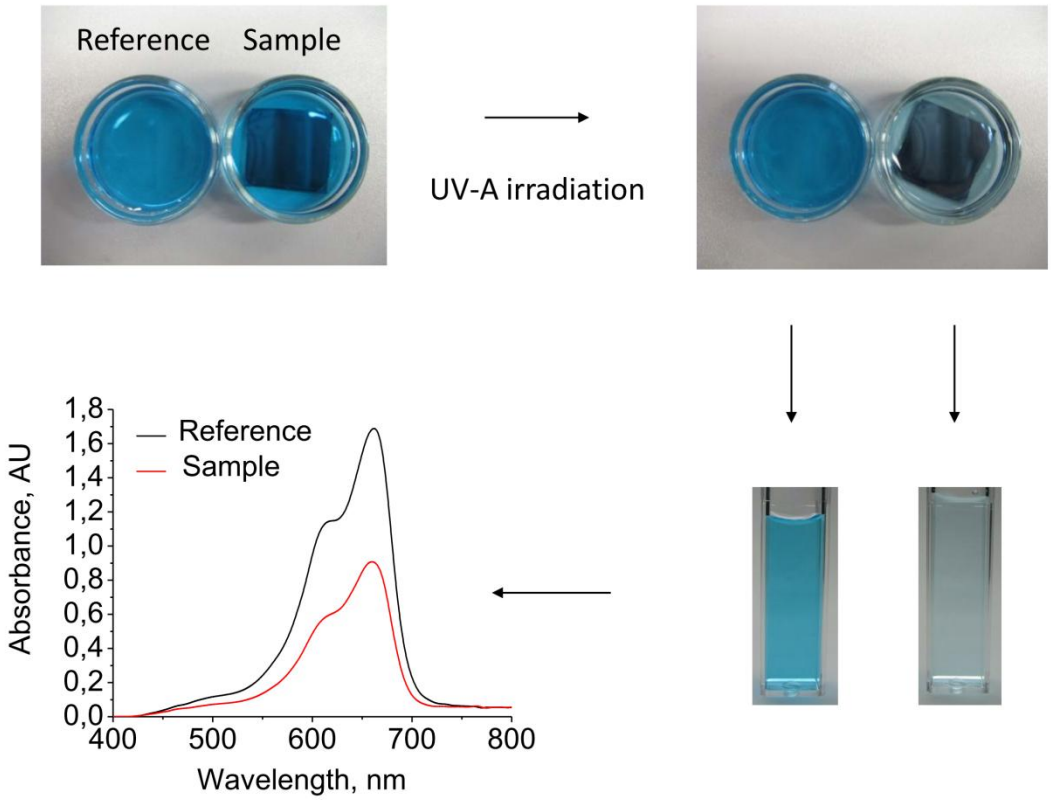

Figure 4.41. Illustration of performance tests of composite coatings with TiO_2 particles, and absorbance of aqueous solution of methylene blue.[232,233]

In Figure 4.40 it is seen that the top surface of particles is covered by thin layer of plasma-modified PDMS. This layer prevents the diffusion of electron-hole pairs to the surface, and may also absorb and reflect UV light needed for the activation of photocatalyc effect. As the result, it decreases the performance of photocatalytic activity of coatings. To open the surface of TiO_2 nanoparticles and improve the efficiency of coatings, the modified PDMS overlayer was etched in a low-pressure asymmetric CCRF discharge (13.56 MHz) in CF_4 gas. The design of reactor is described in details in the PhD thesis of S. Stepanov ([234], pp. 37-39). Main processing parameters of the CF_4 plasma etching are presented in Table 4.3.

The samples were placed on the surface of the powered electrode or 2 cm above at floating potential and faced towards the powered electrode. In the latter case no etching effect was observed. For samples on the powered electrode energetic particles (ions and neutrals) struck the surface of samples, which resulted in the etching with the constant rate of about 0.8 nm/s.

Table 4.3. Main processing parameters of the etching process.

Processing gas	CF_4
Discharge type	Asymmetric CCRF, 13.56 MHz
Process pressure	20 Pa
Gas flow	15 sccm
Forward power	100 W
Full reactor volume	ca. 20 L
Powered electrode surface area	50 cm^2
Treatment time	10 – 90 s

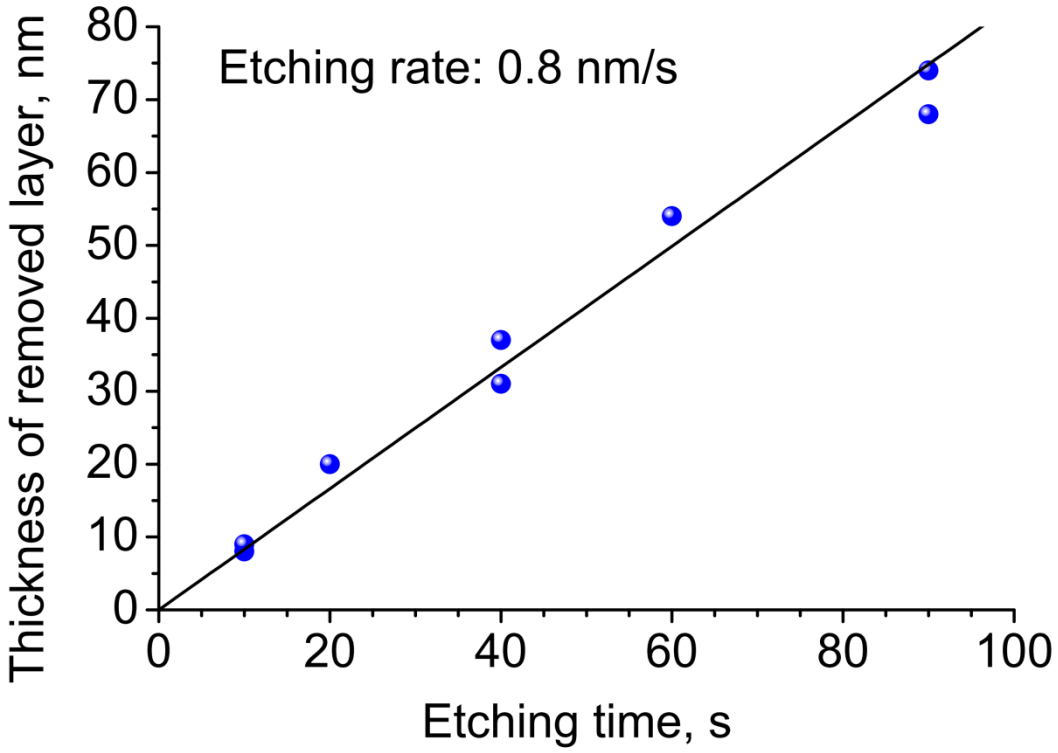

Figure 4.42. Thickness reduction as the function of etching time. Initial thickness of films was 145 - 160 nm. The data are taken from [15,232,233].

Figure 4.43 compares micrograph of a non-etched film and films etched during various time. The thickness reduction due to plasma etching is clearly seen. When the reduction exceeds ca. 50 - 70 nm, the top surface of TiO_2 particles is strongly opened, and the improvement of the photocatalytic performance is optimal. Figure 4.44 demonstrates this

improvement tested on the decomposition of methylene blue.[15] The photocatalytic activity of composite films with TiO_2 was also compared with that of Pilkinkton Active™, which is a benchmark photocatalyst film for comparison with other photocatalyst.[235] It is seen in Figure 4.44 that after etching the composite films are not inferior to the Pilkinkton Active™ coating.

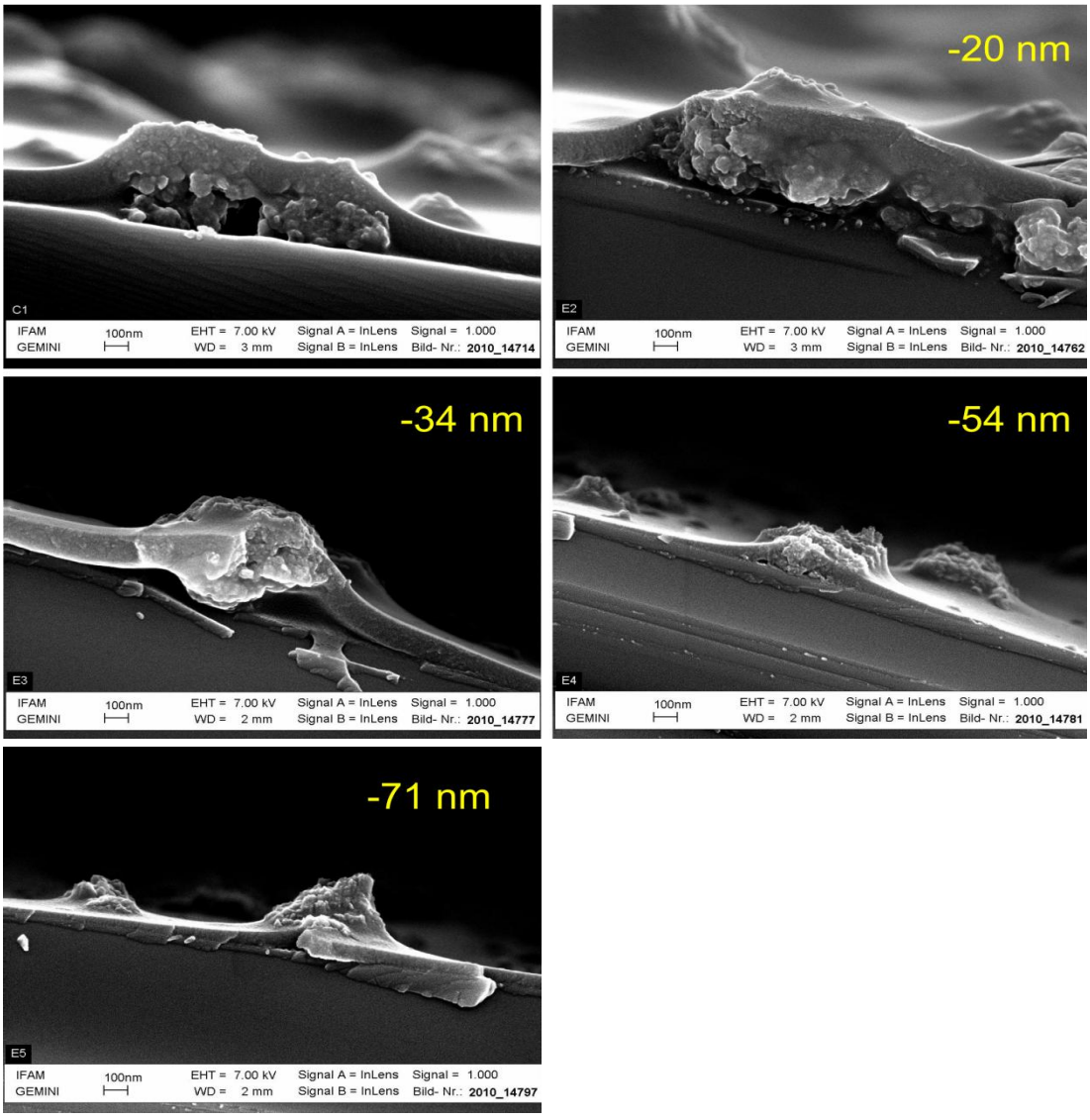

Figure 4.43. SEM micrographs of a non-etched film and films etched during various time. Yellow numbers show the thickness reduction.

Figures 4.43 and 4.44 are published with permission of the authors. Data is adapted from [15,232,233]

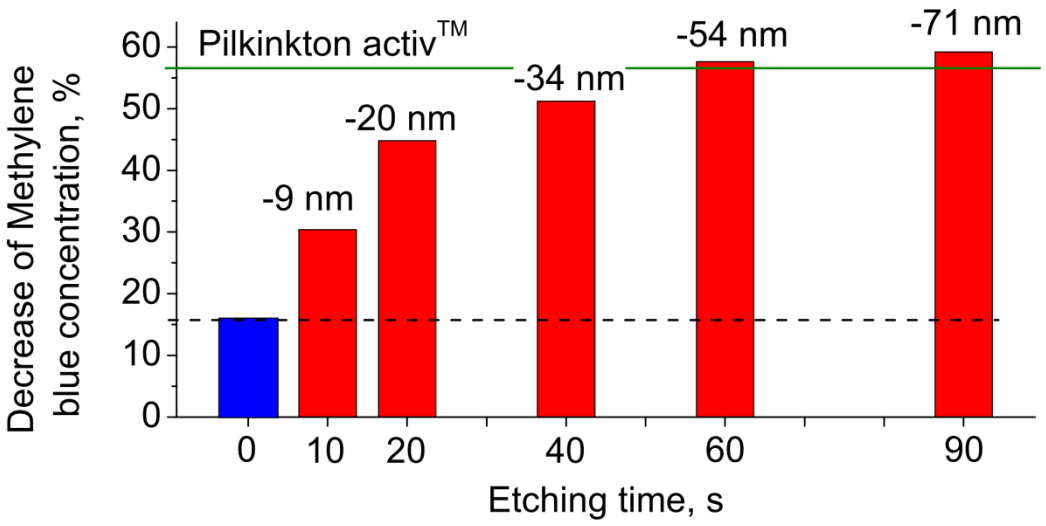

Figure 4.44. Enhancement of the photocatalytic activity after 24 h UV-A irradiation vs. etching time. Negative numbers over bars indicate the thickness reduction. The green line demonstrates the photocatalytic efficiency of Pilkinkton Active™ glass.

5. Summary and Outlook

The development of innovative coatings with multifunctional properties is an ambitious task in modification of material surfaces. Besides conventional technologies, e.g., the Chemical Vapor Deposition (CVD) as a thermal process, the non-thermal plasma is widely applied to deposit thin functional films from the plasma chemical conversion of precursors or from sputtered target material in magnetron discharges. Furthermore, thin functional composite films consisting of a bulk matrix layer with embedded nanoparticles are synthesized, e.g., by co-deposition of a plasma polymer film and nanoparticles from magnetron sputtering.

A novel approach is a hybrid method combining the non-thermal plasma processing with nanotechnology for the development of multifunctional surface coatings.

The conception of the hybrid coating process is based on three steps:

- the preparation of a suspension consisting of an organic liquid and functional nanoparticles,
- the deposition of the suspension as a thin liquid film on the material surface, and
- the plasma modification of the liquid organic film to achieve a thin solid composite film with embedded nanoparticles demonstrating multifunctional properties and good adherence on the substrate material.

In this work the liquid polydimethylsiloxane (PDMS) was applied as a model system, and the experimental investigations were focused on the PDMS plasma modification. In particular, the specific role of the different plasma components and the influence of the plasma and processing parameters on the PDMS modification were studied. The applied capacitively coupled radio frequency (CCRF) plasma was analyzed by electric probe measurements and optical emission spectroscopy, whereas the molecular changes in PDMS due to plasma-induced chemical

reactions were studied by the Fourier transform infrared reflection absorption spectroscopy. Additionally, the photocatalytic activity of thin composite films consisting of plasma cross-linked PDMS with embedded TiO_2 nanoparticles was demonstrated.

During the investigation it was found that the CCRF discharge modifies efficiently thin liquid PDMS films to solid coatings. The penetration depth of particles like neutrals, ions, electrons and radicals in the film is strongly limited. The samples were positioned in the plasma bulk at floating potential, and by means of probe measurements it was measured that the difference between plasma and floating potential is typically 10 − 20 V. This potential difference corresponds to the boundary sheath voltage at the sample and determines the maximum kinetic energy of positive ions impinging on the PDMS surface. But by such low energy ions can penetrate only in a surface layer with the thickness of few nanometers (< 5 nm). The penetration depth of plasma electrons, neutrals and radicals does not even exceed that of ions. Though, plasma particles impinging on a PDMS film do not penetrate in the film bulk, they contribute in the modification of the top layer with the approximate thickness of 5 nm. The heating of samples in the CCRF discharge is weak to modify PDMS by itself and only the plasma radiation is able to transform the liquid bulk to solid one. It is known that the absorption onset of PDMS lies in the VUV region (below 200 nm). The energetic VUV radiation penetrates into the PDMS film on a thickness from several hundred nanometers to few micrometers and initiates photochemical reactions there. Thus, different gases like Ar, Xe, O_2, H_2O, air and H_2 were tested to provide the strongest VUV emission intensity of the CCRF discharge. Discharge pressure and power were varied for all these gases and it was found that at all conditions the H_2 plasma demonstrates drastically stronger emission. Thus, this gas was selected for the plasma treatment of liquid PDMS films.

The IRRAS analysis revealed the transformation process of PDMS with the degradation of CH_3 groups, the formation of new groups like SiOH, CH_2 and SiH, the formation of the SiO_x material and crosslinking. Here, it is known that abstracted H atoms and CH_3 radicals leave the film and form stable gaseous products like H_2, CH_4 and C_2H_6 and participate in further chemical reactions. It was found that the modification effect is not uniform across the film thickness. The top region with an initial thickness up to 100 nm loses all CH_3 groups, in the underlying region the CH_3 concentration increases gradually from zero to the value for PDMS, if the film was thick enough. The methyl-free SiO_x top layer contains also

SiOH and SiH groups. Furthermore, the SiH groups are concentrated only in a very thin layer with a thickness below 10 nm. The presence of the unscreened polar SiOSi and SiOH groups on the surface causes the adsorption of H_2O from the atmosphere, which was also observed by IRRAS.

By means of the spectroscopic ellipsometry it was found out that all above described regions experience a shrinking. The reason is the crosslinking and loss of material. The most shrunken layer is the top SiO_x layer with the shrinking ratio (final thickness/initial thickness) of 0.55 - 0.60. Further, this ratio gradually rise up to the value of 0.95 in the deeper region, which has the concentration of CH_3 groups of about that for PDMS. After the analysis of all results the depth of effective modification was estimated at 300 - 400 nm for the most optimal conditions.

The optimization of the plasma VUV intensity was realized by variation of discharge pressure and power. The strongest plasma emission at studied conditions provided the irradiance of the sample of ca. 13 mW/cm^2. However, such strong radiation causes very strong production rate of the abovementioned gaseous products. These products leave the modifying film slower as they are produced, what causes their accumulation in there. Their pressure grows up leading to formation of bubbles, which can later explode. Finally, the film becomes heavily damaged. To avoid this effect the pressure and the RF power were changed to reduce the irradiance to 6 - 7 mW/cm^2. This resulted in the absence of any damages.

Dust particles and any original impurities in PDMS oil stimulate formation of fragile bumps in the treated film. Besides impurities, processing conditions can affect also on the film quality. The heating of samples due to the dissipation of energy forwarded to the discharge leads to their expansion. At the same time, the film undergoes a non-uniform change in the chemical structure across their thickness. The bulk of film has much higher expansion coefficient than the top SiO_x layer. Thus, during cooling the film shrinks non-uniformly and the films gets a wavelike structure. Here, dust particles and impurities cause a redistribution of tension forces around themselves in heated films and stimulate additionally the formation of complex wave-like patterns.

The carried out investigation is not comprehensive. For instance, the VUV radiation intensity decreases strongly with the thickness. Therefore, the increase of treatment time to increase the irradiation dose is inefficient. The film should be crosslinked over the whole depth in

another way, e.g. by more intensive excimer or exciplex lamps/lasers (Xe_2^*, ArF^*), which have a narrow emission spectrum in the region of relatively small absorption coefficient (see Figure 4.17). In this case, the effective depth of modification can reach micrometer scale.

Another interesting possibility is to realize the model of propagation of VUV radiation through thin PDMS film, including the effect of modification of its chemical composition within time, like it was done in [135]. Such model includes balance equations for species in modifying material (Si-O, Si-C, C-H and others) and Beer-Lambert law in differential form. All functions depend on spatial coordinate and time. The solution will provide information about concentration profiles of all species in the model across the film thickness for different treatment time. These results can be compared with IR absorbance profiles presented in Figure 4.37 B and C.

X-ray photo electron spectroscopy (XPS) or Auger electron spectroscopy (AES) can be combined with layer-by-layer sputtering of film, for instance by energetic Ar^+, to obtain the elemental composition across the whole film thickness.[200,236,237]

References

[1] M. Birkholz, U. Albers and T. Jung, Nanocomposite layers of ceramic oxides and metals prepared by reactive gas-flow sputtering, *Surface and Coatings Technology* **2004**, *179*, 279.

[2] T. Jung, T. Kälber and V. v. d. Heide, Gas flow sputtering of oxide coatings: practical aspects of the process, *Surface and Coatings Technology* **1996**, *86–87, Part 1*, 218.

[3] T. Jung and A. Westphal, High rate deposition of alumina films by reactive gas flow sputtering, *Surface and Coatings Technology* **1993**, *59*, 171.

[4] G. Battaglin, V. Bello, E. Cattaruzza, F. Gonella, G. Mattei, P. Mazzoldi, R. Polloni, C. Sada and B. F. Scremin, RF magnetron co-sputtering deposition of Cu-based nanocomposite silica films for optical applications, *Journal of Non-Crystalline Solids* **2004**, *345 – 346*, 689.

[5] D. Boscarino, A. Vomiero, G. Mattei, A. Quaranta, P. Mazzoldi and G. Della Mea, Deposition of silica-silver nanocomposites by magnetron cosputtering, *Journal of Vacuum Science & Technology B: Microelectronics and Nanometer Structures* **2005**, *23*, 11.

[6] A. Biswas, Z. Marton, J. Kanzow, J. Kruse, V. Zaporojtchenko, F. Faupel and T. Strunskus, Controlled Generation of Ni Nanoparticles in the Capping Layers of Teflon AF by Vapor-Phase Tandem Evaporation, *Nano Letters* **2002**, *3*, 69.

[7] P. Grytsenko K, A. Capobianchi, A. Convertino, J. Friedrich, D. Schulze R, V. Ksensov, S. Schrader, S. Iwanori and S. G. Pandalai, Polymer-metal nanocomposite thin film prepared by co-evaporation in a vacuum, **2005**, 85.

[8] R. A. Roy, R. Messier and S. V. Krishnaswamy, Preparation and properties of r.f.-sputtered polymer-metal thin films, *Thin Solid Films* **1983**, *109*, 27.

[9] H. Biederman and D. Slavínská, Plasma polymer films and their future prospects, *Surface and Coatings Technology* **2000**, *125*, 371.

[10] M. Raffi, F. Hussain, T. M. Bhatti, J. I. Akhter, A. Hameed and M. M. Hasan, Antibacterial characterization of silver nanoparticles against E. coli ATCC-15224, *Journal of Materials Science & Technology* **2008**, *24*, 192.

[11] M. K. Rai, S. D. Deshmukh, A. P. Ingle and A. K. Gade, Silver nanoparticles: the powerful nanoweapon against multidrug-resistant bacteria, *Journal of Applied Microbiology* **2012**, *112*, 841.

[12] M. C. Xu, Y. K. Gao, E. M. Moreno, M. Kunst, M. Muhler, Y. M. Wang, H. Idriss and C. Woll, Photocatalytic Activity of Bulk TiO_2 Anatase and Rutile Single Crystals Using Infrared Absorption Spectroscopy, *Physical Review Letters* **2011**, *106*, 138302.

[13] D. Reyes-Coronado, G. Rodríguez-Gattorno, M. E. Espinosa-Pesqueira, C. Cab, R. d. Coss and G. Oskam, Phase-pure TiO_2 nanoparticles: anatase, brookite and rutile, *Nanotechnology* **2008**, *19*, 145605.

[14] T. Sumita, T. Yamaki, S. Yamamoto and A. Miyashita, Photo-induced surface charge separation of highly oriented TiO_2 anatase and rutile thin films, *Applied Surface Science* **2002**, *200*, 21.

[15] M. Ott, C. Dolle, V. Danilov, A. Hartwig, J. Meichsner, D. Salz, C. Schmuser, O. Schorsch, M. Sebald, H. E. Wagner and K. D. Vissing, Photocatalytic thin Films Prepared by Plasma Curing of Non-Reactive Siloxane Dispersions Containing TiO_2 Particles, *Contributions to Plasma Physics* **2012**, *52*, 593.

[16] V. P. Tolstoy, I. Chernyshova and V. A. Skryshevsky, Handbook of Infrared Spectroscopy of Ultrathin Films, Wiley, **2003**.

[17] D. Bodas, J. Y. Rauch and C. Khan-Malek, Surface modification and aging studies of addition-curing silicone rubbers by oxygen plasma, *European Polymer Journal* **2008**, *44*, 2130.

[18] F. D. Egitto and L. J. Matienzo, Transformation of Poly(dimethyl-siloxane) into thin surface films of SiO_x by UV/Ozone treatment. Part I: Factors affecting modification, *Journal of Materials Science* **2006**, *41*, 6362.

[19] H. Hillborg, J. F. Ankner, U. W. Gedde, G. D. Smith, H. K. Yasuda and K. Wikstrom, Crosslinked polydimethylsiloxane exposed to oxygen plasma studied by neutron reflectometry and other surface specific techniques, *Polymer* **2000**, *41*, 6851.

[20] L. J. Matienzo and F. D. Egitto, Transformation of poly(dimethylsiloxane) into thin surface films of SiO_x by UV/ozone treatment. Part II: segregation and modification of doped polymer blends, *Journal of Materials Science* **2006**, *41*, 6374.

[21] M. J. Owen and P. J. Smith, Plasma treatment of polydimethyl-siloxane, *Journal of Adhesion Science and Technology* **1994**, *8*, 1063.

[22] K. Fateh-Alavi and U. W. Gedde, Effect of stabilizers on surface oxidation of silicone rubber by corona discharge, *Polymer Degradation and Stability* **2004**, *84*, 469.

[23] S. Bhattacharya, A. Datta, J. M. Berg and S. Gangopadhyay, Studies on surface wettability of poly(dimethyl) siloxane (PDMS) and glass under oxygen-plasma treatment and correlation with bond strength, *Journal of Microelectromechanical Systems* **2005**, *14*, 590.

[24] J. L. Fritz and M. J. Owen, Hydrophobic recovery of plasma-treated polydimethylsiloxane, *Journal of Adhesion* **1995**, *54*, 33.

[25] K. Efimenko, W. E. Wallace and J. Genzer, Surface modification of Sylgard-184 poly(dimethylsiloxane) networks by ultraviolet and ultraviolet/ozone treatment, *Journal of Colloid and Interface Science* **2002**, *254*, 306.

[26] O. Y. Meng, P. P. Klemchuk and J. T. Koberstein, Exploring the effectiveness of SiOx coatings in protecting polymers against photo-oxidation, *Polymer Degradation and Stability* **2000**, *70*, 217.

[27] S. Ichikawa, Photooxidation of plasma polymerized polydimethyl-siloxane film by 172 nm vacuum ultraviolet light irradiation in dilute oxygen, *Journal of Applied Physics* **2006**, *100*, 033510.

[28] B. Schnyder, T. Lippert, R. Kotz, A. Wokaun, V. M. Graubner and O. Nuyken, UV-irradiation induced modification of PDMS films investigated by XPS and spectroscopic ellipsometry, *Surface Science* **2003**, *532*, 1067.

[29] C. L. Mirley and J. T. Koberstein, Preparation of Ultrathin Metal-Oxide Films from Langmuir-Blodgett Layers, *Langmuir* **1995**, *11*, 2837.

[30] E. A. Waddell, S. Shreeves, H. Carrell, C. Perry, B. A. Reid and J. McKee, Surface modification of Sylgard 184 polydimethylsiloxane by 254 nm excimer radiation and characterization by contact angle goniometry, infrared spectroscopy, atomic force and scanning electron microscopy, *Applied Surface Science* **2008**, *254*, 5314.

[31] Y. Berdichevsky, J. Khandurina, A. Guttman and Y. H. Lo, UV/ozone modification of poly(dimethylsiloxane) microfluidic channels, *Sensors and Actuators B: Chemical* **2004**, *97*, 402.

[32] J. C. McDonald, D. C. Duffy, J. R. Anderson, D. T. Chiu, H. K. Wu, O. J. A. Schueller and G. M. Whitesides, Fabrication of microfluidic systems in poly(dimethylsiloxane), *Electrophoresis* **2000**, *21*, 27.

[33] I. Wong and C.-M. Ho, Surface molecular property modifications for poly(dimethylsiloxane) (PDMS) based microfluidic devices, *Microfluidics and Nanofluidics* **2009**, *7*, 291.

[34] I. J. Chen and E. Lindner, The stability of radio-frequency plasma-treated polydimethylsiloxane surfaces, *Langmuir* **2007**, *23*, 3118.

[35] D. T. Eddington, J. P. Puccinelli and D. J. Beebe, Thermal aging and reduced hydrophobic recovery of polydimethylsiloxane, *Sensors and Actuators B: Chemical* **2006**, *114*, 170.

[36] J. A. Vickers, M. M. Caulum and C. S. Henry, Generation of hydrophilic poly(dimethylsiloxane) for high-performance microchip electrophoresis, *Analytical Chemistry* **2006**, *78*, 7446.

[37] P. K. Chu, J. Y. Chen, L. P. Wang and N. Huang, Plasma-surface modification of biomaterials, *Materials Science and Engineering: R: Reports* **2002**, *36*, 143.

[38] V. N. Vasilets, A. V. Kuznetsov and V. I. Sevast'yanov, Regulation of the biological properties of medical polymer materials with the use of a gas-discharge plasma and vacuum ultraviolet radiation, *High Energy Chemistry* **2006**, *40*, 79.

[39] K. Maex, M. R. Baklanov, D. Shamiryan, F. Iacopi, S. H. Brongersma and Z. S. Yanovitskaya, Low dielectric constant materials for microelectronics, *Journal of Applied Physics* **2003**, *93*, 8793.

[40] S. K. Singh, A. A. Kumbhar and R. O. Dusane, Resisting oxygen plasma damage in low-k hydrogen silsesquioxane films by hydrogen plasma treatment, *Materials Letters* **2006**, *60*, 1579.

[41] K. Takeda, Y. Miyawaki, S. Takashima, M. Fukasawa, K. Oshima, K. Nagahata, T. Tatsumi and M. Hori, Mechanism of plasma-induced damage to low-k SiOCH films during plasma ashing of organic resists, *Journal of Applied Physics* **2011**, *109*, 033303.

[42] H. Cui, R. J. Carter, D. L. Moore, H. G. Peng, D. W. Gidley and P. A. Burke, Impact of reductive N_2/H_2 plasma on porous low-dielectric constant SiCOH thin films, *Journal of Applied Physics* **2005**, *97*, 113302.

[43] K. Yonekura, S. Sakamori, K. Goto, M. Matsuura, N. Fujiwara and M. Yoneda, Investigation of ash damage to ultralow-k inorganic materials, *Journal of Vacuum Science & Technology B* **2004**, *22*, 548.

[44] W. Crookes, The Bakerian Lecture: On the Illumination of Lines of Molecular Pressure, and the Trajectory of Molecules, *Philosophical Transactions of the Royal Society of London* **1879**, *170*, 135.

[45] I. Langmuir, Oscillations in Ionized Gases, *Proceedings of the National Academy of Sciences of the United States of America* **1928**, *14*, 627.

[46] M. I. Boulos, P. Fauchais and E. Pfender, Thermal Plasmas: Fundamentals and applications, Plenum Press, **1994**.

[47] M. A. Lieberman and A. J. Lichtenberg, Principles Of Plasma Discharges and Materials Processing, Wiley-Interscience, **2005**.

[48] A. Otto, Basic Elements of the Physics of Charged Particles, www.what.gi.alaska.edu/ao/plasma.

[49] L. C. Tsai, W. H. Tsai, W. S. Schreiner, F. T. Berkey and J. Y. Liu, Comparisons of GPS/MET retrieved ionospheric electron density and ground based ionosonde data, *Earth Planets and Space* **2001**, *53*, 193.

[50] M. C. Kelley, The Earth's Ionosphere: Plasma Physics and Electrodynamics, Academic Press, **2009**.

[51] M. Rybansky and V. Rusin, Integral Brightness of Corona during Solar Eclipse of June 30, 1973, *Bulletin of the Astronomical Institutes of Czechoslovakia* **1975**, *26*, 206.

[52] Current solar images, http://umbra.nascom.nasa.gov/images/latest.html.

[53] G. Noci, The Temperature of the Solar Corona, *Memorie della Società Astronomica Italiana* **2003**, *74*, 704.

[54] A. D. Fokker, Electron Temperature of Solar Corona as Derived from Radio Observations, *Bulletin of the Astronomical Institutes of the Netherlands* **1966**, *18*, 359.

[55] A. P. Hayes, A. Vourlidas and R. A. Howard, Deriving the electron density of the solar corona from the inversion of total brightness measurements, *Astrophysical Journal* **2001**, *548*, 1081.

[56] G. P. Serbu, Explorer 35 Observations of Solar-Wind Electron Density, Temperature, and Anisotropy, *Journal of Geophysical Research* **1972**, *77*, 1703.

[57] V. K. Zhivotov, V. D. Rusanov and A. A. Fridman, Diagnostics of a nonequilibrium chemically active plasma, Energoatomizdat, Moscow **1985**. In Russian.

[58] Y. P. Raizer, Gas discharge physics, Springer, **1991**.

[59] H. Tawara, Y. Itikawa, H. Nishimura and M. Yoshino, Cross-Sections and Related Data for Electron Collisions with Hydrogen Molecules and Molecular-Ions, *Journal of Physical and Chemical Reference Data* **1990**, *19*, 617.

[60] J. S. Yoon, M. Y. Song, J. M. Han, S. H. Hwang, W. S. Chang, B. Lee and Y. Itikawa, Cross sections for electron collisions with hydrogen molecules, *Journal of Physical and Chemical Reference Data* **2008**, *37*, 913.

[61] K. Kohler, J. W. Coburn, D. E. Horne, E. Kay and J. H. Keller, Plasma potentials of 13.56-MHz rf argon glow discharges in a planar system, *Journal of Applied Physics* **1985**, *57*, 59.

[62] A. Metze, D. W. Ernie and H. J. Oskam, Application of the physics of plasma sheaths to the modeling of rf plasma reactors, *Journal of Applied Physics* **1986**, *60*, 3081.

[63] P. Horowitz and W. Hill, The Art of Electronics, Cambridge University Press, **1989**.

[64] L. M. Tolbert, B. Ozpineci, S. K. Islam and M. S. Chinthavali, Wide bandgap semiconductors for utility applications, *Power and Energy Systems, Proceedings* **2003**, 317.

[65] A. Benmoussa, J. F. Hochedez, W. K. Schmutz, U. Schuhle, M. Nesladek, Y. Stockman, U. Kroth, M. Richter, A. Theissen, Z. Remes, K. Haenen, V. Mortet, S. Koller, J. P. Halain, R. Petersen, M. Dominique and M. D'Olieslaeger, Solar-blind diamond detectors for LYRA, the solar VUV radiometer on board PROBA II, *Experimental Astronomy* **2003**, *16*, 141.

[66] A. BenMoussa, A. Soltani, U. Schuhle, K. Haenen, Y. M. Chong, W. J. Zhang, R. Dahal, J. Y. Lin, H. X. Jiang, H. A. Barkad, B. BenMoussa, D. Bolsee, C. Hermans, U. Kroth, C. Laubis, V. Mortet, J. C. De Jaeger, B. Giordanengo, M. Richter, F. Scholze and J. F. Hochedez, Recent developments of wide-bandgap semiconductor based UV sensors, *Diamond and Related Materials* **2009**, *18*, 860.

[67] F. Omnes, E. Monroy, E. Munoz and J. L. Reverchon, Wide bandgap UV photodetectors: A short review of devices and applications, *Gallium Nitride Materials and Devices II* **2007**, *6473*, 64730E.

[68] R. Goldstein and F. N. Mastrup, Absorption Coefficients of the O_2 Schumann-Runge Continuum from 1270 Å - 1745 Å using a New Continuum Source, *J. Opt. Soc. Am.* **1966**, *56*, 765.

[69] H. C. Lu, H. K. Chen, H. F. Chen, B. M. Cheng and J. F. Ogilvie, Absorption cross section of molecular oxygen in the transition $E^3\Sigma_u^- v = 0 - X^3\Sigma_g^- v = 0$ at 38 K, *Astronomy & Astrophysics* **2010**, *520*, A19.

[70] S. Ogawa and M. Ogawa, Absorption Cross-Sections of $O_2(a^1\Delta_g)$ and $O_2(X^3\Sigma_g^-)$ in Region from 1087 to 1700 A, *Canadian Journal of Physics* **1975**, *53*, 1845.

[71] K. Yoshino, W. H. Parkinson, K. Ito and T. Matsui, Absolute absorption cross-section measurements of Schumann-Runge continuum of O_2 at 90 and 295 K, *Journal of Molecular Spectroscopy* **2005**, *229*, 238.

[72] I. D. Sudit and F. F. Chen, RF compensated probes for high-density discharges, *Plasma Sources Science & Technology* **1994**, *3*, 162.

[73] J. N. Hilfiker, R. Synowicki and H. G. Tompkins, Spectroscopic Ellipsometry Methods for thin Absorbing Coatings, *SVC - 51st Annual Technical Conference Proceedings* **2008**, 511.

[74] R. M. A. Azzam and N. M. Bashara, Ellipsometry and polarized light, North-Holland Pub. Co., **1977**.

[75] H. Fujiwara, Spectroscopic Ellipsometry: Principles and Applications, Wiley, **2007**.

[76] H. G. Tompkins and E. A. Irene, Handbook Of Ellipsometry, William Andrew Pub., **2005**.

[77] H. G. Tompkins, WVASE32® Software Training Manual, **2006**.

[78] D. Stroud, The effective medium approximations: Some recent developments, *Superlattices and Microstructures* **1998**, *23*, 567.

[79] D. Goncalves and E. A. Irene, Fundamentals and applications of spectroscopic ellipsometry, *Quimica Nova* **2002**, *25*, 794.

[80] J. B. Theeten and D. E. Aspnes, Ellipsometry in Thin-Film Analysis, *Annual Review of Materials Science* **1981**, *11*, 97.

[81] A. E. Naciri, L. Broch, L. Johann and R. Kleim, Fixed polarizer, rotating-polarizer and fixed analyzer spectroscopic ellipsometer: accurate calibration method, effect of errors and testing, *Thin Solid Films* **2002**, *406*, 103.

[82] S. Bertucci, A. Pawlowski, N. Nicolas, L. Johann, A. El Ghemmaz, N. Stein and R. Kleim, Systematic errors in fixed polarizer, rotating polarizer, sample, fixed analyzer spectroscopic ellipsometry, *Thin Solid Films* **1998**, *313*, 73.

[83] B. C. Smith, Fundamentals of Fourier Transform Infrared Spectroscopy, Second Edition, Taylor & Francis Group, **2011**.

[84] B. C. Smith, Infrared Spectral Interpretation: A Systematic Approach, Crc Press, **1999**.

[85] B. H. Stuart, Infrared Spectroscopy: Fundamentals and Applications, John Wiley & Sons, **2004**.

[86] P. Griffiths and J. A. De Haseth, Fourier Transform Infrared Spectrometry, Wiley, **2007**.

[87] J. Kauppinen and J. Partanen, Fourier Transforms in Spectroscopy, Wiley, **2011**.

[88] A. Rogalski, HgCdTe infrared detector material: history, status and outlook, *Reports on Progress in Physics* **2005**, *68*, 2267.

[89] P. Capper and C. T. Elliott, Infrared Detectors and Emitters: Materials and Devices, Springer-Verlag GmbH, **2001**.

[90] S. A. Francis and A. H. Ellison, Infrared Spectra of Monolayers on Metal Mirrors, *Journal of the Optical Society of America* **1959**, *49*, 131.

[91] R. G. Greenler, Infrared Study of Adsorbed Molecules on Metal Surfaces by Reflection Techniques, *Journal of Chemical Physics* **1966**, *44*, 310.

[92] R. G. Greenler, Reflection Method for Obtaining Infrared Spectrum of a Thin Layer on a Metal Surface, *Journal of Chemical Physics* **1969**, *50*, 1963.

[93] G. N. Kuznetsova, V. P. Tolstoi, S. I. Kol'tsov and V. B. Aleskovskii, Optimum conditions for the detection of ir reflection-absorption spectra of oxide layers on metals, *Journal of Applied Spectroscopy* **1980**, *32*, 167.

[94] K. Molt, Die Infrarot-Spektroskopie als Methode zur chemischen Charakterisierung von dünnen Schichten auf Metallen, *Fresenius' Journal of Analytical Chemistry* **1984**, *319*, 743.

[95] R. Abbas, E. C. Ihmels, S. Enders and J. Gmehling, Measurement of Transport Properties for Selected Siloxanes and Their Mixtures Used as Working Fluids for Organic Rankine Cycles, *Industrial & Engineering Chemistry Research* **2011**, *50*, 8756.

[96] O. K. Bates, Thermal Conductivity of Liquid Silicones, *Industrial & Engineering Chemistry* **1949**, *41*, 1966.

[97] Dow Corning®, http://www.dowcorning.com.

[98] I. Gelest, B. C. Arkles and G. L. Larson, Silicon compounds: silanes and silicones : a survey of properties and chemistry, Gelest, Inc., **2008**.

[99] N. Grassie and I. G. Macfarlane, The thermal degradation of polysiloxanes - I.Poly(dimethylsiloxane), *European Polymer Journal* **1978**, *14*, 875.

[100] H. Zhixiong, X. Wenfeng and C. Dongcai, The thermal decomposition kinetics of polysiloxane/polymethylacrylate IPNs materials, *Journal of Wuhan University of Technology--Materials Science Edition* **2006**, *21*, 47.

[101] S. J. Blanksby and G. B. Ellison, Bond Dissociation Energies of Organic Molecules, *Accounts of Chemical Research* **2003**, *36*, 255.

[102] J. E. Mark, Polymer data handbook, Oxford University Press, **1999**.

[103] I. Pinnau and Z. J. He, Pure- and mixed-gas permeation properties of polydimethylsiloxane for hydrocarbon/methane and hydrocarbon/hydrogen separation, *Journal of Membrane Science* **2004**, *244*, 227.

[104] A. Singh, B. D. Freeman and I. Pinnau, Pure and mixed gas acetone/nitrogen permeation properties of polydimethylsiloxane [PDMS], *Journal of Polymer Science Part B-Polymer Physics* **1998**, *36*, 289.

[105] T. C. Merkel, V. I. Bondar, K. Nagai, B. D. Freeman and I. Pinnau, Gas sorption, diffusion, and permeation in poly(dimethylsiloxane), *Journal of Polymer Science Part B: Polymer Physics* **2000**, *38*, 415.

[106] M. Sadrzadeh, K. Shahidi and T. Mohammadi, Synthesis and Gas Permeation Properties of a Single Layer PDMS Membrane, *Journal of Applied Polymer Science* **2010**, *117*, 33.

[107] P. C. Nicolson and J. Vogt, Soft contact lens polymers: an evolution, *Biomaterials* **2001**, *22*, 3273.

[108] R. W. Baker, N. Yoshioka, J. M. Mohr and A. J. Khan, Separation of Organic Vapors from Air, *Journal of Membrane Science* **1987**, *31*, 259.

[109] H. H. Nijhuis, M. H. V. Mulder and C. A. Smolders, Selection of Elastomeric Membranes for the Removal of Volatile Organics from Water, *Journal of Applied Polymer Science* **1993**, *47*, 2227.

[110] A. J. Barry, Viscometric Investigation of Dimethylsiloxane Polymers, *Journal of Applied Physics* **1946**, *17*, 1020.

[111] M. J. Hunter, E. L. Warrick, J. F. Hyde and C. C. Currie, Organosilicon Polymers. II.The Open Chain Dimethylsiloxanes with Trimethylsiloxy End Groups, *Journal of the American Chemical Society* **1946**, *68*, 2284.

[112] J. E. Mark, H. R. Allcock and R. West, Inorganic polymers, Oxford University Press, **2005**.

[113] T. Mundry, Einbrennsilikonisierung bei pharmazeutischen Glaspackmitteln analytische Studien eines Produktionsprozesses, Ph.D. dissertation, Humboldt University of Berlin, **1999**.

[114] Wikipedia, http://en.wikipedia.org/wiki/Simethicone.

[115] D. K. Cai, A. Neyer, R. Kuckuk and H. M. Heise, Optical absorption in transparent PDMS materials applied for multimode waveguides fabrication, *Optical Materials* **2008**, *30*, 1157.

[116] D. K. Cai, A. Neyer, R. Kuckuk and H. M. Heise, Raman, mid-infrared, near-infrared and ultraviolet-visible spectroscopy of PDMS silicone rubber for characterization of polymer optical waveguide materials, *Journal of Molecular Structure* **2010**, *976*, 274.

[117] D. K. Cai, Optical and Mechanical Aspects on Polysiloxane Based Electrical-Optical-Circuits-Board, PhD dissertation, Technical University of Dortmund, **2008**.

[118] V. M. Graubner, R. Jordan, O. Nuyken, T. Lippert, M. Hauer, B. Schnyder and A. Wokaun, Incubation and ablation behavior of poly(dimethylsiloxane) for 266 nm irradiation, *Applied Surface Science* **2002**, *197*, 786.

[119] S. Kopetz, D. Cai, E. Rabe and A. Neyer, PDMS-based optical waveguide layer for integration in electrical-optical circuit boards, *AEU - International Journal of Electronics and Communications* **2007**, *61*, 163.

[120] D. Oldfield and T. Symes, Long term natural ageing of silicone elastomers, *Polymer Testing* **1996**, *15*, 115.

[121] M. Amin, M. Akbar and S. Amin, Hydrophobicity of silicone rubber used for outdoor insulation (An overview), *Reviews on Advanced Materials Science* **2007**, *16*, 10.

[122] D. Meyerhofer, Characteristics of Resist Films Produced by Spinning, *Journal of Applied Physics* **1978**, *49*, 3993.

[123] D. W. Schubert and T. Dunkel, Spin coating from a molecular point of view: its concentration regimes, influence of molar mass and distribution, *Materials Research Innovations* **2003**, *7*, 314.

[124] A. von Keudell, M. Meier and T. Schwarz-Selinger, Simultaneous interaction of methyl radicals and atomic hydrogen with amorphous hydrogenated carbon films, as investigated with optical in situ diagnostics, *Applied Physics a-Materials Science & Processing* **2001**, *72*, 551.

[125] J. F. Ziegler, M. D. Ziegler and J. P. Biersack, TRIM (the Transport of Ions in Matter) software, http://www.srim.org/

[126] H. Yamamoto, K. Asano, K. Ishikawa, M. Sekine, H. Hayashi, I. Sakai, T. Ohiwa, K. Takeda, H. Kondo and M. Hori, Chemical bond modification in porous SiOCH films by H_2 and H_2/N_2 plasmas investigated by in situ infrared reflection absorption spectroscopy, *Journal of Applied Physics* **2011**, *110*, 123301.

[127] S. Uchida, S. Takashima, M. Hori, M. Fukasawa, K. Ohshima, K. Nagahata and T. Tatsumi, Plasma damage mechanisms for low-k porous SiOCH films due to radiation, radicals, and ions in the plasma etching process, *Journal of Applied Physics* **2008**, *103*, 073303.

[128] A. C. Cefalas, E. Sarantopoulou, E. Gogolides and P. Argitis, Absorbance and outgasing of photoresist polymeric materials for UV lithography below 193 nm including 157 nm lithography, *Microelectronic Engineering* **2000**, *53*, 123.

[129] V. E. Skurat and Y. I. Dorofeev, The Transformations of Organic Polymers during the Illumination by 147.0 and 123.6 nm Light, *Angewandte Makromolekulare Chemie* **1994**, *216*, 205.

[130] T. L. Cottrell, The Strengths of Chemical Bonds, Butterworths, London **1958**.

[131] R. Walch, "Bond dissociation energies in organosilicon compounds" in: *Silicone Compound: Silanes and Silicones,* 2nd ed., B. Arkles and G. Larson, Eds., Gelest, Inc., Morrisville, PA **2008**.

[132] M. R. Wertheimer, A. C. Fozza and A. Hollander, Industrial processing of polymers by low-pressure plasmas: the role of VUV radiation, *Nuclear Instruments & Methods in Physics Research Section B-Beam Interactions with Materials and Atoms* **1999**, *151*, 65.

[133] M. Nitschke, Infrarotspektroskopische Charakterisierung plasmamodifizierter Polymeroberflächen, PhD dissertation, Technical University of Chemnitz and Zwickau, Chemnitz **1996**.

[134] D. Barton, J. W. Bradley, K. J. Gibson, D. A. Steele and R. D. Short, An in situ comparison between VUV photon and ion energy fluxes to polymer surfaces immersed in an RF plasma, *Journal of Physical Chemistry B* **2000**, *104*, 7150.

[135] J. Lee and D. B. Graves, The effect of VUV radiation from Ar/O_2 plasmas on low-k SiOCH films, *Journal of Physics D-Applied Physics* **2011**, *44*, 325203.

[136] M. J. Titus, D. Nest and D. B. Graves, Absolute vacuum ultraviolet flux in inductively coupled plasmas and chemical modifications of 193 nm photoresist, *Applied Physics Letters* **2009**, *94*, 171501.

[137] A. A. Lissovski and A. B. Treshchalov, Emission of the third continuum of argon excited by a pulsed volume discharge, *Physics of Plasmas* **2009**, *16*, 123501.

[138] M. Moselhy, R. H. Stark, K. H. Schoenbach and U. Kogelschatz, Resonant energy transfer from argon dimers to atomic oxygen in microhollow cathode discharges, *Applied Physics Letters* **2001**, *78*, 880.

[139] H. Nagai, M. Hiramatsu, M. Hori and T. Goto, Measurement of oxygen atom density employing vacuum ultraviolet absorption spectroscopy with microdischarge hollow cathode lamp, *Review of Scientific Instruments* **2003**, *74*, 3453.

[140] M. J. Druyvesteyn, Der Niedervoltbogen, *Zeitschrift Fur Physik* **1930**, *64*, 781.

[141] C. A. Anderson and W. G. Graham, Temporally and Spatially-Resolved Plasma Parameters and EEDF Measurements in a Low-Frequency Discharge, *Plasma Sources Science & Technology* **1995**, *4*, 561.

[142] D. D. Blackwell and F. F. Chen, Time-resolved measurements of the electron energy distribution function in a helicon plasma, *Plasma Sources Science & Technology* **2001**, *10*, 226.

[143] F. F. Chen, Lecture notes on Langmuir probe diagnostics, *Mini-Course on Plasma Diagnostics, IEEE-ICOPS meeting, Jeju, Korea* **2003**.

[144] F. F. Chen, Langmuir probes in RF plasma: surprising validity of OML theory, *Plasma Sources Science & Technology* **2009**, *18*, 035012.

[145] C. W. Chung, Experimental investigation on the floating potential of cylindrical Langmuir probes in non-Maxwellian electron distributions, *Physics of Plasmas* **2005**, *12*, 123505.

[146] V. I. Demidov, S. V. Ratynskaia and K. Rypdal, Electric probes for plasmas: The link between theory and instrument, *Review of Scientific Instruments* **2002**, *73*, 3409.

[147] M. Dimitrova, T. K. Popov, J. Todorov and T. G. Naydenova, Second derivative Langmuir probe measurements in Faraday dark space in Argon d.c. gas discharge at intermediate pressures, *First International Workshop and Summer School on Plasma Physics* **2006**, *44*, 169.

[148] A. Ganguli, B. B. Sahu and R. D. Tarey, A new structure for RF-compensated Langmuir probes with external filters tunable in the absence of plasma, *Plasma Sources Science & Technology* **2008**, *17*, 015003.

[149] V. A. Godyak and V. I. Demidov, Probe measurements of electron-energy distributions in plasmas: what can we measure and how can we achieve reliable results?, *Journal of Physics D-Applied Physics* **2011**, *44*, 233001.

[150] M. Hannemann and F. Sigeneger, Langmuir probe measurements at incomplete rf-compensation, *Czechoslovak Journal of Physics* **2006**, *56*, B740.

[151] S. Klagge, Space-Resolved and Direction-Resolved Langmuir Probe Diagnostic in RF Planar Discharges, *Plasma Chemistry and Plasma Processing* **1992**, *12*, 103.

[152] G. Neumann, U. Banziger, M. Kammeyer and M. Lange, Plasma-Density Measurements by Microwave Interferometry and Langmuir Probes in an Rf Discharge, *Review of Scientific Instruments* **1993**, *64*, 19.

[153] A. Schwabedissen, E. C. Benck and J. R. Roberts, Langmuir probe measurements in an inductively coupled plasma source, *Physical Review E* **1997**, *55*, 3450.

[154] A. E. Wendt, Passive external radio frequency filter for Langmuir probes, *Review of Scientific Instruments* **2001**, *72*, 2926.

[155] N. Hershkowitz, "How Langmuir Probes Work" in: *Plasma Diagnostics,* O. Auciello and D. L. Flamm, Eds., Academic Press, Boston **1989**.

[156] N. A. Gorbunov, A. Grochola, P. Kruk, A. Pietruczuk and T. Stacewicz, Studies of electron energy distribution in plasma produced by a resonant laser pulse, *Plasma Sources Science & Technology* **2002**, *11*, 492.

[157] N. A. Gorbunov, A. N. Kopytov and F. E. Latyshev, Determination of the electron energy distribution in a plasma from the first and second derivatives of the probe current, *Technical Physics* **2002**, *47*, 940.

[158] H. Li, Measurements of electron energy distribution function and neutral gas temperature in an inductively coupled plasma, Thesis for the Degree of Master of Science, University of Saskatchewan, Saskatoon **2006**.

[159] C. M. O. Mahony, J. McFarland, P. G. Steen and W. G. Graham, Structure observed in measured electron energy distribution functions in capacitively coupled radio frequency hydrogen plasmas, *Applied Physics Letters* **1999**, *75*, 331.

[160] F. F. Chen, dc probe detection of phased EEDFs in RF discharges, *Plasma Physics and Controlled Fusion* **1997**, *39*, 1533.

[161] T. E. Sharp, Potential-energy curves for molecular hydrogen and its ions, *Atomic Data and Nuclear Data Tables* **1971**, *2*, 119.

[162] L. Conde, An introduction to Langmuir probe diagnostics of plasmas, http://plasmalab.aero.upm.es/~lcl/PlasmaProbes/Probes-2010-2.pdf.

[163] J. M. Ajello, S. K. Srivastava and Y. L. Yung, Laboratory studies of uv emissions of H_2 by electron impact. The Werner- and Lyman-band systems, *Physical Review A* **1982**, *25*, 2485.

[164] H. Schmoranzer and R. Zietz, Observation of Selectively Excited Continuous Vacuum Ultraviolet Emission in Molecular-Hydrogen, *Physical Review A* **1978**, *18*, 1472.

[165] J. Watson and R. J. Anderson, Excitation of E,$F^1\Sigma_g^+$ States of H_2 by Electron-Impact, *Journal of Chemical Physics* **1977**, *66*, 4025.

[166] S. M. A. Espinho, Experimental investigation of UV radiation from microwave Ar, Ar-H_2 and H_2 plasmas, Master's dissertation, Instituto Superior Técnico, Lisbon **2012**.

[167] L. Xianming, E. S. Donald, H. Abgrall, E. Roueff, D. Dziczek, D. L. Hansen and J. M. Ajello, Time-resolved Electron Impact Study of Excitation of H_2 Singlet-Gerade States from Cascade Emission in the Vacuum Ultraviolet Region, *The Astrophysical Journal Supplement Series* **2002**, *138*, 229.

[168] W. Ubachs and E. Reinhold, Highly Accurate H_2 Lyman and Werner Band Laboratory Measurements and an Improved Constraint on a Cosmological Variation of the Proton-to-Electron Mass Ratio, *Physical Review Letters* **2004**, *92*, 101302.

[169] B. P. Lavrov, A. S. Melnikov, M. Kaning and J. Ropcke, uv continuum emission and diagnostics of hydrogen-containing nonequilibrium plasmas, *Physical Review E* **1999**, *59*, 3526.

[170] K. Dittmann, Detailed Investigations of the Sheath Dynamics and Elementary Processes in Capacitively Coupled RF Plasmas, PhD dissertation, Ernst-Moritz-Arndt-University, Greifswald **2009**.

[171] G. K. James, J. M. Ajello and W. R. Pryor, The middle ultraviolet-visible spectrum of H_2 excited by electron impact, *Journal of Geophysical Research-Planets* **1998**, *103*, 20113.

[172] A. Aguilar, J. M. Ajello, R. S. Mangina, G. K. James, H. Abgrall and E. Roueff, The electron-excited mid-ultraviolet to near-infrared spectrum of H_2: Cross sections and transition probabilities, *Astrophysical Journal Supplement Series* **2008**, *177*, 388.

[173] A. Aguilar, G. K. James, J. M. Ajello, H. Abgrall and E. Roueff, Visible to Near Infrared Emission Spectra of Electron-Excited H_2, *Proceedings of the NASA LAW 2006, held February 14-16, 2006, UNLV, Las Vegas. Published by NASA Ames, Moffett Field, CA* **2006**, 140.

[174] T. M. Bloomstein, M. Rothschild, R. R. Kunz, D. E. Hardy, R. B. Goodman and S. T. Palmacci, Critical issues in 157 nm lithography, *Journal of Vacuum Science & Technology B* **1998**, *16*, 3154.

[175] B. L. Sowers, M. W. Williams, R. N. Hamm and E. T. Arakawa, Optical Properties of Some Silicone Diffusion-Pump Oils in Vacuum Ultraviolet-Using a Closed-Cell Technique, *Journal of Applied Physics* **1971**, *42*, 4252.

[176] J. P. Guelfucci, M. Brou and M. L. Huertas, VUV photoionization process in non polar dielectric liquids, *Journal De Chimie Physique Et De Physico-Chimie Biologique* **1999**, *96*, 1.

[177] J. P. Guelfucci, M. Brou, M. L. Huertas and J. Casanovas, Photoionization of polydimethylsiloxane oils and determination of the associated parameters, *Journal of Electrostatics* **1999**, *47*, 39.

[178] H. Koizumi, K. Lacmann and W. F. Schmidt, Light-Induced Electron-Emission from Silicone Oils, *Journal of Physics D-Applied Physics* **1992**, *25*, 857.

[179] V. O. Saik and S. Lipsky, Absorption spectra of some liquids in the VUV, *Journal of Physical Chemistry A* **2001**, *105*, 10107.

[180] R. Roberge, C. Sandorfy, J. I. Matthews and O. P. Strausz, Far Ultraviolet and Hel Photoelectron-Spectra of Alkyl and Fluorine Substituted Silane Derivatives, *Journal of Chemical Physics* **1978**, *69*, 5105.

[181] V. Huber, K. R. Asmis, A. C. Sergenton, M. Allan and S. Grimme, Electron energy loss and DFT/SCI study of the singlet and triplet excited states and electron attachment energies of tetramethylsilane, hexamethyldisilane, tris(trimethylsilyl)silane, and tetramethoxysilane, *Journal of Physical Chemistry A* **1998**, *102*, 3524.

[182] M. Ahmed, P. Potzinger and H. G. Wagner, Photolysis of Tetramethylsilane near the Absorption Onset - Mechanism and Photophysics, *Journal of Photochemistry and Photobiology a-Chemistry* **1995**, *86*, 33.

[183] L. Gammie, C. Sandorfy and O. P. Strausz, Photochemistry of Silicon - Compounds. 6. 147 nm Photolysis of Tetramethylsilane, *Journal of Physical Chemistry* **1979**, *83*, 3075.

[184] S. K. Tokach and R. D. Koob, Photolysis of Tetramethylsilane at 147 nm - Reactivity of $(CH_3)_3Si$ and $(CH_3)_2SiCH_2$, *Journal of Physical Chemistry* **1979**, *83*, 774.

[185] S. Siegel and T. Stewart, Vacuum-Ultraviolet Photolysis of Polydimethylsiloxane . Gas Yields and Energy Transfer, *Journal of Physical Chemistry* **1969**, *73*, 823.

[186] H. R. Philipp, Optical Properties of Non-Crystalline Si, SiO, SiO_x and SiO_2, *Journal of Physics and Chemistry of Solids* **1971**, *32*, 1935.

[187] G. Zuther, Dielectric and Optical-Properties of Siox, *Physica Status Solidi a-Applied Research* **1980**, *59*, K109.

[188] O. Leroy, P. Stratil, J. Perrin, J. Jolly and P. Belenguer, Spatiotemporal Analysis of the Double-Layer Formation in Hydrogen Radio-Frequency Discharges, *Journal of Physics D-Applied Physics* **1995**, *28*, 500.

[189] M. Ackerman, "UV-solar radiation related to mesospheric processes" in: *Mesospheric Models and Related Experiments,* G.-Fiocco, Ed., D. Reidel Publishing Company, Dordrecht **1971**.

[190] M. M. Gurevich, Photometry (Theory, Methods and Devices), Energoatomizdat, Leningrad **1983**. in Russian.

[191] Solar Constant and Air Mass Zero Solar Spectral Irradiance Tables, E 490 − 00a, *American Society for Testing and Materials (Reapproved 2006).*

[192] V. Danilov, H.-E. Wagner and J. Meichsner, Modification of Polydimethylsiloxane Thin Films in H_2 Radio-frequency Plasma Investigated by Infrared Reflection Absorption Spectroscopy, *Plasma Processes and Polymers* **2011**, *8*, 1059.

[193] H. Chatham, Oxygen diffusion barrier properties of transparent oxide coatings on polymeric substrates, *Surface & Coatings Technology* **1996**, *78*, 1.

[194] J. Goldstein, Scanning Electron Microscopy and X-Ray Micro-analysis, Springer London, Limited, **2003**.

[195] N. Bowden, S. Brittain, A. G. Evans, J. W. Hutchinson and G. M. Whitesides, Spontaneous formation of ordered structures in thin films of metals supported on an elastomeric polymer, *Nature* **1998**, *393*, 146.

[196] N. Bowden, W. T. S. Huck, K. E. Paul and G. M. Whitesides, The controlled formation of ordered, sinusoidal structures by plasma oxidation of an elastomeric polymer, *Applied Physics Letters* **1999**, *75*, 2557.

[197] E. Grossman and I. Gouzman, Space environment effects on polymers in low earth orbit, *Nuclear Instruments & Methods in Physics Research Section B-Beam Interactions with Materials and Atoms* **2003**, *208*, 48.

[198] N. Levy, E. Grossman, I. Gouzman and Y. Noter, VUV radiation interaction with outgassing products of black paints: In-situ NUV-VIS spectroscopy and complementary studies, *Proceedings of the 9th International Symposium on Materials in a Space Environment* **2003**, *540*, 217.

[199] D. B. H. Chua, H. T. Ng and S. F. Y. Li, Spontaneous formation of complex and ordered structures on oxygen-plasma-treated elastomeric polydimethylsiloxane, *Applied Physics Letters* **2000**, *76*, 721.

[200] J. Y. Park, H. Y. Chae, C. H. Chung, S. J. Sim, J. Park, H. H. Lee and P. J. Yoo, Controlled wavelength reduction in surface wrinkling of poly(dimethylsiloxane), *Soft Matter* **2010**, *6*, 677.

[201] Z. Q. Cao and X. Zhang, Density change and viscous flow during structural relaxation of plasma-enhanced chemical-vapor-deposited silicon oxide films, *Journal of Applied Physics* **2004**, *96*, 4273.

[202] J. Thurn and R. F. Cook, Stress hysteresis during thermal cycling of plasma-enhanced chemical vapor deposited silicon oxide films, *Journal of Applied Physics* **2002**, *91*, 1988.

[203] J. Thurn, R. F. Cook, M. Kamarajugadda, S. P. Bozeman and L. C. Stearns, Stress hysteresis and mechanical properties of plasma-enhanced chemical vapor deposited dielectric films, *Journal of Applied Physics* **2004**, *95*, 967.

[204] H. Shih and P. J. Flory, Equation-of-State Parameters for Poly(Dimethylsiloxane), *Macromolecules* **1972**, *5*, 758.

[205] V. M. Graubner, D. Clemens, T. Gutberlet, R. Kotz, T. Lippert, O. Nuyken, B. Schnyder and A. Wokaun, Neutron reflectometry and spectroscopic ellipsometry studies of cross-linked poly(dimethyl-siloxane) after irradiation at 172 nm, *Langmuir* **2005**, *21*, 8940.

[206] M. Ouyang, P. P. Klemchuk and J. T. Koberstein, Exploring the effectiveness of SiOx coatings in protecting polymers against photo-oxidation, *Polymer Degradation and Stability* **2000**, *70*, 217.

[207] M. Ouyang, C. Yuan, R. J. Muisener, A. Boulares and J. T. Koberstein, Conversion of some siloxane polymers to silicon oxide by UV/ozone photochemical processes, *Chemistry of Materials* **2000**, *12*, 1591.

[208] C. Carteret and A. Labrosse, Vibrational properties of polysiloxanes: from dimer to oligomers and polymers. 1. Structural and vibrational properties of hexamethyldisiloxane $(CH_3)_3SiOSi(CH_3)_3$, *Journal of Raman Spectroscopy* **2010**, *41*, 996.

[209] P. J. Launer, "Infrared analysis of organosilicon compounds: spectra-structure correlations" in: *Silicone Compound: Silanes and Silicones,* 2nd edition, B. Arkles and G. Larson, Eds., Gelest, Inc., Morrisville, PA **2008**.

[210] V. M. Graubner, R. Jordan, O. Nuyken, B. Schnyder, T. Lippert, R. Kotz and A. Wokaun, Photochemical modification of cross-linked poly(dimethylsiloxane) by irradiation at 172 nm, *Macromolecules* **2004**, *37*, 5936.

[211] V. P. Tolstoy, I. V. Chernyshova and V. A. Skryshevsky, Handbook of Infrared Spectroscopy of Ultrathin Films, John Wiley & Sons, Inc., Hoboken, NJ, USA **2003**.

[212] B. Harbecke, B. Heinz and P. Grosse, Optical-Properties of Thin-Films and the Berreman Effect, *Applied Physics a-Materials Science & Processing* **1985**, *38*, 263.

[213] H. Kriegsmann, Spektroskopische Untersuchungen an Siliciumverbindungen. 7.Die Schwingungsspektren Der Hoheren Dimethyl-Polysiloxan-Ringe Und Die Struktur Des Oktamethyl-Cyclo-Tetrasiloxans, *Zeitschrift fur Anorganische und Allgemeine Chemie* **1959**, *298*, 232.

[214] G. Socrates, Infrared Characteristic Group Frequencies: Tables and Charts, John Wiley, Chichester **1994**.

[215] S. N. Gruzinov and V. P. Tolstoi, Reflection-absorption of ultrathin films on the surface of semiconductors and dielectrics by the method of IR spectroscopy, *Journal of Applied Spectroscopy* **1987**, *46*, 480.

[216] W. Jacob, A. von Keudell and T. Schwarz-Selinger, Infrared analysis of thin films: Amorphous, hydrogenated carbon on silicon, *Brazilian Journal of Physics* **2000**, *30*, 508.

[217] J. D. Mcintyre and D. E. Aspnes, Differential Reflection Spectroscopy of Very Thin Surface Films, *Surface Science* **1971**, *24*, 417.

[218] K. Yamamoto and H. Ishida, Optical Theory Applied to Infrared-Spectroscopy, *Vibrational Spectroscopy* **1994**, *8*, 1.

[219] S. B. Jung, H. H. Park and H. Kim, The role of vacuum ultraviolet in H-2 plasma treatment on SiO_2 aerogel film, *Applied Surface Science* **2003**, *216*, 156.

[220] C. L. Mirley and J. T. Koberstein, A Room-Temperature Method for the Preparation of Ultrathin SiO_x Films from Langmuir-Blodgett Layers, *Langmuir* **1995**, *11*, 1049.

[221] C. Dolle, M. Papmeyer, M. Ott and K. Vissing, Gradual Photochemical-Induced Conversion of Liquid Polydimethylsiloxane Layers to Carbon Containing Silica Coatings by VUV Irradiation at 172 nm, *Langmuir* **2009**, *25*, 7129.

[222] A. Lehmann, L. Schumann and K. Hübner, Optical Phonons in Amorphous Silicon Oxides. II. Calculation of Phonon Spectra and Interpretation of the IR Transmission of SiO_x, *physica status solidi (b)* **1984**, *121*, 505.

[223] A. Brunet-Bruneau, S. Fisson, B. Gallas, G. Vuye and J. Rivory, Infrared ellipsometric study of SiO2 films: relationship between LO mode frequency and porosity, *Thin Solid Films* **2000**, *377*, 57.

[224] A. Brunet-Bruneau, S. Fisson, G. Vuye and J. Rivory, Change of TO and LO mode frequency of evaporated SiO2 films during aging in air, *Journal of Applied Physics* **2000**, *87*, 7303.

[225] W. G. Graham, Vacuum Ultraviolet Emission and H^- Production in a Low-Pressure Hydrogen Plasma, *Journal of Physics D-Applied Physics* **1984**, *17*, 2225.

[226] R. J. Muisener, A room temperature method for the formation of ultrathin silicon oxide films, Ph.D. dissertation, University of Connecticut, **1999**.

[227] V. Danilov, H.-E. Wagner and J. Meichsner, The Distribution of CH_3 Over the Film Thickness and Shrinkage of H_2 Plasma-Modified PDMS Films, *Plasma Processes and Polymers* **2013**, *10*, 320.

[228] S. Worch, M. Sebald and O. Schorsch, Customization of nano-TiO_2 dispersions for high photocatalytic activity, half-yearly meetings of the project "Plasma Hybrid Coating: Functional Surfaces by Plasma Supported Nano Technology", Bremen, 2008 - 2012.

[229] O. Carp, C. L. Huisman and A. Reller, Photoinduced reactivity of titanium dioxide, *Progress in Solid State Chemistry* **2004**, *32*, 33.

[230] E. Bizani, K. Fytianos, I. Poulios and V. Tsiridis, Photocatalytic decolorization and degradation of dye solutions and wastewaters in the presence of titanium dioxide, *Journal of Hazardous materials* **2006**, *136*, 85.

[231] U. Diebold, The surface science of titanium dioxide, *Surface Science Reports* **2003**, *48*, 53.

[232] C. D. M. Ott, J. H. Bredehöft, V. Danilov, A. Hartwig, E. Jolondz, J. Meichsner, P. Swiderek, D. Salz, C. Schmüser, M. Sebald, O. Schorsch, H.-E. Wagner, K.-D. Vissing, Plasma Hybrid Coating: Functional Surfaces by Plasma Supported Nano Technology, 2nd International Symposium on Functional Surfaces, September, Aachen, Germany, September 14 – 15, 2011.

[233] C. D. M. Ott, V. Danilov, J. Meichsner, D. Salz, C. Schmüser, O. Schorsch, H.-E. Wagner, K.-D. Vissing, Funktionelle Oberflächen mittels Plasma-Nanotechnologie, 15. Plasma-technologietagung – PT 15, Stuttgart, 28.02. – 02.03.2011.

[234] S. Stepanov, Absolute number density and kinetic analysis of CF, CF_2 and C_2F_4 molecules in pulsed CF_4/H_2 rf plasmas, PhD dissertation, Unversity of Greifswald, Greifswald **2010**.

[235] A. Mills, A. Lepre, N. Elliott, S. Bhopal, I. P. Parkin and S. A. O'Neill, Characterisation of the photocatalyst Pilkington Activ™: a reference film photocatalyst?, *Journal of Photochemistry and Photobiology a-Chemistry* **2003**, *160*, 213.

[236] M. Brinkmann, V. Z. H. Chan, E. L. Thomas, V. Y. Lee, R. D. Miller, N. Hadjichristidis and A. Avgeropoulos, Room-temperature synthesis of alpha-SiO_2 thin films by UV-assisted ozonolysis of a polymer precursor, *Chemistry of Materials* **2001**, *13*, 967.

[237] O. Joubert, G. Hollinger, C. Fiori, R. A. B. Devine, P. Paniez and R. Pantel, Ultraviolet Induced Transformation of Polysiloxane Films, *Journal of Applied Physics* **1991**, *69*, 6647.

List of Abbreviations

AC	alternating current
CCP	capacitively coupled plasma
CCRF	capacitively coupled radio-frequency
DC	direct current
DTGS detector	deuterium tryglycine sulfate detector
EEDF	electron energy distribution function
EEPF	electron energy probability function
EMA	effective medium approximation
FTIR spectroscopy	Fourier transform infrared spectroscopy
HMDSO	hexamethyldisiloxane
ICP	inductively coupled plasma
IR	infrared
IRRAS	infrared reflection absorption spectroscopy
LO phonon	longitudinal optical phonon
MCT	mercury cadmium telluride
MSE	mean squared error
OES	optical emission spectroscopy
OPD	optical path difference
PDMS	polydimethylsiloxane
PMT	photomultiplier
PRPSE	polarizer, rotating polarizer spectroscopic ellipsometer
RF	radio-frequency
SE	spectroscopic ellipsometry
SEM	scanning electron microscopy
SWE	single wavelength ellipsometry
TMS	tetramethylsilane
VUV	vacuum ultraviolet

List of Symbols

A, B, C	parameters of Cauchy model
C_{pow} , C_{gr}	capacitance of the sheath at powered and grounded electrode
d	film thickness or characteristic probe dimension
e	electron charge
E	electric field strength
E_λ	spectral irradiance
f	processing gas flow
f_p	electron energy probability function
h	probe sheath thickness
$I(\delta)$	interferogram
I_e	electron current to a probe
k	extinction coefficient
k_B	Boltzman constant
L	luminance
m_e	electron mass
m_i	ion mass
n	refractive index
n_e	electron concentration
n_i	ion concentration
$\tilde{n} = n + ik$	complex refractive index
p	discharge pressure
r_p , r_s	reflection coefficients for p- and s-polarized light
T_e	electron temperature
T_i	ion temperature
$\mathrm{T_w}$	transmittance of a window
t_r	residence time
S	spectral response of detector or probe surface area
V	processing chamber volume or voltage
V_{RF}	amplitude of RF field
V_{bias}	self-bias voltage
V_{fl}	floating potential
V_{pl}	plasma potential
Z	ionization multiplicity
Δ	ellipsometric parameter
δ	path difference of beams in an interferometer
ε	electron energy
ε_0	vacuum permittivity
ε_i	dielectric function of a layer with index i
Λ	plasma parameter
λ	wavelength

λ_D	Debye length
λ_{De} , λ_{Di}	Debye length of electrons and ions
μ_e , μ_a , μ_{er}	electron mobility and its active and reactive component
ν_0	electron elastic collision frequency
σ	standard deviation and conductivity
σ_a , σ_r	active and reactive plasma conductivity
τ	average time between electron-neutral collisions
ϕ	angle of incidence
Φ	luminous flux
Ψ	ellipsometric parameter
ω	discharge excitation frequency
ω_p	plasma frequency
ω_{pe} , ω_{pi}	plasma frequency of electrons and ions

List of Figures

List of Tables

Hiermit erkläre ich, dass diese Arbeit bisher von mir weder an der Mathematisch-Naturwissenschaftlichen Fakultät der Ernst-Moritz-Arndt-Universität Greifswald noch einer anderen wissenschaftlichen Einrichtung zum Zwecke der Promotion eingereicht wurde.

Ferner erkläre ich, dass ich diese Arbeit selbständig verfasst und keine anderen als die darin angegebenen Hilfsmittel und Hilfen benutzt und keine Textabschnitte eines Dritten ohne Kennzeichnung übernommen habe.

Curriculum Vitae

Personal Information

Date and place of birth: Oktober 7, 1984, St.-Petersburg, Russia
E-Mail: Vl.danilov@gmail.com

Education

01.09.1991 20.06.1999	High school Nr. 645 , St.-Petersburg, Russia
01.09.1999 20.06.2001	Academic Gymnasium at Saint-Petersburg State University (with a focus on mathematics and physics)
01.09.2001 15.06.2005	Institute of Physics, Department of Optics and Spectroscopy, Saint-Petersburg State University, Russia Specialization (since 2003): Plasma Physics Bachelor thesis: "Hydrodynamic and kinetic modeling of the cathode layer in the DC glow discharge in xenon," Rating: 5.0 (maximum 5.0) Scientific supervisor: Prof. Dr. Y. B. Golubovskii (E-Mail: yuri.golubovski@pobox.spbu.ru)
01.09.2005 25.01.2008	Institute of Physics, Department of Optics and Spectroscopy, Saint-Petersburg State University, Russia (Master of Science) Specialization: Plasma physics and plasma chemistry Master thesis: "Investigation of the positive column of glow discharge in oxygen at low pressures", grade: 5.0 (maximum 5.0) Scientific supervisor: Prof. Dr. Y. B.Golubovskii (E-Mail: yuri.golubovski@pobox.spbu.ru)

01.06.2008 up to date	PhD student in the workgroup Low Temperature Plasma Physics, Experimental Physics I, Institute of Physics, University of Greifswald Scientific supervisor: Prof. Dr. Jürgen Meichsner (E-Mail: meichsner@physik.uni-greifswald.de) Title of thesis: "Plasma Modification of Polydimethylsiloxane in a hydrogen CCRF low-pressure discharge"

Professional experience

01.06.2008 up to date	Scientific researcher, Institute of Physics, University of Greifswald
01.06.2008 31.06.2012	Project: "Plasma hybrid coating: functional surfaces by plasma supported nanotechnology", supported by the Volkswagen Foundation Supervisor: Prof. Dr. Jürgen Meichsner (E-Mail: meichsner@physik.uni-greifswald.de) Supervisor: PD Dr.. Hans-Erich Wagner (E-Mail: wagner@physik.uni-greifswald.de)

Award

February 2013	The third poster prize of German Society of Plasma Technology at the conference "Plasma Technology 16"

Peer-reviewed publications:

(1) **V. Danilov**, H. E. Wagner and J. Meichsner, Modification of polydimethylsiloxane thin films in H_2 radio-frequency plasma investigated by Infrared Reflection Absorption Spectroscopy, *Plasma Processes and Polymers* 2011, *8*, 1059.

(2) P. Swiderek, E. Jolondz, J. H. Bredehöft, T. Borrmann, C. Dölle, M. Ott, C. Schmüser, A. Hartwig, **V. Danilov**, H.-E. Wagner, J. Meichsner , Modification of Polydimethylsiloxane Coatings by H_2 RF Plasma, Xe_2^* Excimer VUV Radiation, and Low-Energy Electron Beams, *Macromolecular Materials and Engineering* 2012, *297*, 10912012.

(3) M. Ott, C. Dölle, **V. Danilov**, A. Hartwig, J. Meichsner, D. Salz, C. Schmüser, O. Schorsch, M. Sebald, H.-E. Wagner and K.-D. Vissing, Photocatalytic thin Films Prepared by Plasma Curing of Non-Reactive Siloxane Dispersions Containing TiO_2 Particles, *Contributions to Plasma Physics* 2012, *52*, 593.

(4) D. Skácelová, **V. Danilov**, J. Schäfer, A. Quade, P. Sťahel, M. Černák and J. Meichsner, Room temperature plasma oxidation in DCSBD: A new method for preparation of silicon dioxide films at atmospheric pressure, *Materials Science and Engineering: B*, 2013, *178*, 651.

(5) **V. Danilov**, H. E. Wagner and J. Meichsner, The distribution of CH_3 over the film thickness and shrinkage of H_2 plasma-modified PDMS films, *Plasma Processes and Polymers* 2013, *10*, 320.

(6) H. C. Thejaswini, R. Bogdanowicz, **V. Danilov**, J. Meichsner and R. Hippler, Characterization of a-CN_x:H Thin Films Deposited in C_2H_m/N_2 (m = 2, 4, 6) Barrier Discharge, *The Journal of Physical Chemistry*. (submitted)

Conference proceedings:

(1) **V. Danilov**, C. Dölle, M. Ott, H.-E. Wagner, J. Meichsner, Plasma treatment of polydimethylsiloxane thin films studied by infrared reflection absorption spectroscopy, XXIXth International Conference on Phenomena in Ionized Gases, July 12 – 17, 2009, Cancún, México, Contributed Paper, p. 104

(2) **V. Danilov**, H.-E. Wagner and J. Meichsner, Modification of polydimethylsiloxane thin films in H_2 discharge, XXXth International Conference on Phenomena in Ionized Gases, August 28th – September 2nd, 2011, Belfast, Great Britain, Contributed Paper

(3) **V. Danilov**, C. Dölle, M. Ott, H.-E. Wagner, J. Meichsner, Modification of liquid PDMS films by a H_2 CCRF discharge at low pressures, XXXIth International Conference on Phenomena in Ionized Gases, July 14 – 19, 2013, Granada, Spain, Contributed Paper

Other conference contributions:

(1) H. T. Do, R. Bogdanowicz, **V. Danilov**, J. Meichsner, M. Gnyba, and R. Hippler, Particles and thin films deposited by Ar/C_2H_2 and Ar/CH_4 plasmas, DPG Spring Meeting, Greifswald, 30. März – 02. April 2009, Poster

(2) **V. Danilov**, H.-E. Wagner and J. Meichsner, Plasma treatment of polydimethylsiloxane thin films, XVII. Erfahrungsaustausch *"*Oberflächentechnologie mit Plasma- und Ionenstrahlprozessen*"*, March 2 – 4, Mühlleithen / Vogtland, 2010, Talk

(3) **V. Danilov**, H.-E. Wagner, and J. Meichsner, Plasma treatment of polydimethylsiloxane thin films, DPG Spring Meeting 2010, March 21 – 26, Regensburg, Poster

(4) M. Ott, Christopher Dölle, **V. Danilov**, A. Hartwig, J. Meichsner, D. Salz, O. Schorsch, M. Sebald, H.-E. Wagner, K.-D. Vissing, Novel approach for the creation of photocatalytic thin films by plasma curing of TiO_2 containing dispersions of non-reactive siloxanes, Twelfth International Conference on Plasma Surface Engineering (PSE 2010), September 13 – 17, 2010, Garmisch-Partenkirchen, Talk

(5) **V. Danilov**, H.-E. Wagner, and J. Meichsner, Modifizierung von dünnen Schichten aus Polydimethylsiloxan in RF-Wasserstoff-

plasmen, 15. Plasma-technologietagung – PT 15, Stuttgart, 28.02. – 02.03.2011, Poster

(6) M. Ott, C. Dölle, **V. Danilov**, J. Meichsner, D. Salz, C. Schmüser, O. Schorsch, H.-E. Wagner, K.-D. Vissing, Funktionelle Oberflächen mittels Plasma-Nanotechnologie, 15. Plasma-technologietagung – PT 15, Stuttgart, 28.02. – 02.03.2011, Talk

(7) **V. Danilov**, H.-E. Wagner, and J. Meichsner, Plasmavernetzung von Polydimethylsiloxan (PDMS) zur Herstellung von Nanokompositschichten mit photokatalytisch aktiven Oberflächen, XVIII. Erfahrungsaustausch, Oberflächentechnologie mit Plasma - und Ionenstrahlprozessen, Mühlleithen/Vogtland, 08. – 10.03.2011, Talk

(8) **V. Danilov**, H.-E. Wagner and J. Meichsner, H_2 plasma modification of polydimethylsiloxane thin films investigated by infrared reflection absorption spectroscopy, 75th Annual Meeting of the DPG and DPG Spring Meeting, Dresden, 13. – 18.03.2011, Poster

(9) **V. Danilov**, H.-E. Wagner, and J. Meichsner, Modification of polydimethylsiloxane thin films in H_2 CCRF plasma studied by IR reflection absorption spectroscopy, DPG Spring Meeting, Kiel, 28. – 31.03.2011, Talk

(10) **V. Danilov**, H.-E. Wagner, and J. Meichsner, Modification of polydimethylsiloxane thin films in H_2 RF discharge, International Conference on Phenomena in Ionized Gases (ICPIG), Belfast, Northern Ireland, 28.08 – 02.09.2011, Poster

(11) **V. Danilov**, H.-E. Wagner, and J. Meichsner, Treatment of thin polydimethylsiloxane films in RF plasmas investigated by infrared reflection absorption spectroscopy, 2nd International Symposium on Functional Surfaces, Aachen 14. – 15.9.2011, Poster

(12) D. Salz, **V. Danilov**, C. Dölle, A. Hartwig, J. Meichsner, C. Schmüser, M. Sebald, O. Schorsch, H.-E. Wagner, M. Ott, Photocatalytic TiO_2 layers by Plasma Hybrid Coating, 2nd International Symposium on Functional Surfaces, September 14 – 15, 2011, Aachen, Germany, Poster

(13) P. Swiderek, E. Jolondz, J. H. Bredehöft, M. Ott, C. Dölle, C. Schmüser, H.-E. Wagner, **V. Danilov**, J. Meichsner, Plasma Hybrid Coating: Contribution of free electrons to the chemical modification of polysiloxane coatings, 2nd International Symposium on Functional Surfaces, September 14 – 15, 2011, Aachen, Germany, Poster

(14) M. Ott, C. Dölle, J. H. Bredehöft, **V. Danilov**, A. Hartwig, E. Jolondz, J. Meichsner, P. Swiderek, D. Salz, C. Schmüser, M. Sebald, O. Schorsch, H.-E. Wagner, K.-D. Vissing: Plasma Hybrid Coating: Functional Surfaces by Plasma Supported Nano Technology, 2nd International Symposium on Functional Surfaces, September 14 – 15, 2011, Aachen, Germany, Talk

(15) D. Salz, C. Dölle, **V. Danilov**, J. Meichsner, C. Schmüser, O. Schorsch, K.-D. Vissing, H.-E. Wagner und M. Ott: Nano-kompositschichten mit photokatalytischen Eigenschaften 19. NDVak - Beschichtung, Modifizierung und Charakterisierung von Polymeroberflächen, October 19. – 20., 2011, Dresden, Germany, Talk

(16) P. Swiderek, E. Jolondz, J. H. Bredehöft, T. Borrmann, C. Dölle, M. Ott, C. Schmüser, A. Hartwig, **V. Danilov**, H.-E. Wagner, J. Meichsner, Modification of polydimethylsiloxane coatings by H_2 RF plasma, Xe_2^* excimer VUV radiation, and low-energy electron beams, 18th Symposium on Atomic, Cluster and Surface Physics, January 22. - 27., 2012, Alpe d'Huez, France, Poster

(17) **V. Danilov**, H.-E. Wagner and J. Meichsner, Cross-linking of polydimethylsiloxane thin films in hydrogen CCRF plasma, DPG Spring Meeting of the Section AMOP, Stuttgart, 12. – 16.03.2012, Poster

(18) **V. Danilov**, H.-E. Wagner and J. Meichsner, Cross-linking of PDMS thin films in hydrogen CC-RF plasma, 13th International Conference on Plasma Surface Engineering, Garmisch-Partenkirchen, 10. – 14.09, 2012, Poster

(19) **V. Danilov**, H.-E. Wagner and J. Meichsner, Characterization of thin films treated by a low-pressure CCRF discharge in H_2, Plasmatechnologie 16, Greifswald, 18. – 20.02, 2013, Poster

(20) **V. Danilov**, C. Dölle, M. Ott, H.-E. Wagner, J. Meichsner, Modification of liquid PDMS films by a H_2 CCRF discharge at low pressures, XXXIth International Conference on Phenomena in Ionized Gases, July 14 – 19, 2013, Granada, Spain, Poster

Acknowledgements

It is a great pleasure to thank everyone, who helped me to complete my dissertation successfully. I express my sincere acknowledgement to my scientific advisor Prof. Dr. Jürgen Meichsner for the support and guidance throughout my research work. I am thankful to him also for the possibility to work in the interesting scientific project, for valuable discussions and for the provided possibility to present my work at numerous conferences.

I am heartily grateful to Dr. Hans-Erich Wagner for comprehensive support in the project, for helpful discussions and advices throughout the whole work.

I appreciate technical magicians of our workgroup Peter Druckrey and Uwe Meißner for the great support and help in constructing and upgrading of experimental setups, and for Mister Twister.

I would like to express my deep gratitude to all my colleagues participated with me in the project "Plasma Hybrid Coating: Functional Surfaces by Plasma Supported Nano Technology" for valuable experience, new knowledge in various scientific branches and for the additional results provided for my dissertation. Namely, I thank Dr. Jan Hendrik Bredehöft, Dr. Christopher Dölle, Dr. habil. Andreas Hartwig, Evgeni Jolondz, Dr. Matthias Ott, Dr. Dirk Salz, Dr. Oliver Schorsch, Christoph Schmüser, Prof. Petra Swiderek and Dr. Klaus Vissing.

Many thanks to colleagues of my workgroup for pleasant and homelike atmosphere: Johannes Benduhn, Marc Bogaczyk, Dr. Kristian Dittmann, Jochen Zöllner, Thea Rassmann, Filip Fuchs, Frank Wienholtz, Dirk Pasedag, Mario Dünnbier, Sergey Stepanov, Hans Höft, Steffi Kaledat, Dr. Bert Krames, Dr. Christian Küllig, Stefan Miekley, Vera Müller, Dr. Holger Testrich, Robert Tschiersch, Iris-Diana Passow, Sebastian Nemschokmichal, Thomas Schumann, Martin Steinert, Jun.-Prof. Lars Stollenwerk, Thomas Wegner and Robert Wild.

My special thanks are to my friends Vladimir Sushkov, Gleb Fedoseev, Marina Ganeva and Oxana Ivanova.

I am grateful to Dana Skácelová for the joint work, which provided me new experience and knowledge. I also wish to thank Dr. Mykola Medvidov for SEM images of thin plasma-modified films.

I warmly thank my parents, my sister and Valeria for their overall support during all the years.